

DISSERTATION

Helical Optical Metamaterials

Zur Erlangung des akademischen Grades eines
DOKTORS DER NATURWISSENSCHAFTEN
von der Fakultät für Physik des
Karlsruher Instituts für Technologie (KIT)

genehmigte

DISSERTATION

von

Dipl.-Phys. Justyna Kinga Gansel
aus Backnang

Tag der mündlichen Prüfung: 04. Mai 2012

Referent: Prof. Dr. Martin Wegener _____

Korreferent: Prof. Dr. Kurt Busch _____

Publications

Parts of this thesis have already been published in scientific journals:

- J. K. Gansel, M. Thiel, M. S. Rill, M. Decker, K. Bade, V. Saile, G. von Freymann, S. Linden, and M. Wegener, “Gold Helix Photonic Metamaterial as Broadband Circular Polarizer,” *Science* **325**, 1513 (2009).
- J. K. Gansel, M. Wegener, S. Burger, and S. Linden, “Gold helix photonic metamaterials: A numerical parameter study,” *Opt. Express* **18**, 1059 (2010).
- M. Thiel, J. K. Gansel, M. Wegener, and G. von Freymann, “Wenn das Licht den Dreh raus hat. Künstliche chirale Materialien,” *Phys. Unserer Zeit* **42**, 70 (2011).
- J. K. Gansel, M. Latzel, A. Frölich, J. Kaschke, M. Thiel, and M. Wegener, “Tapered gold-helix metamaterials as improved circular polarizers,” *Appl. Phys. Lett.* **100**, 101109 (2012).

Parts of this thesis have already been published at conferences (only own presentations):

- J. K. Gansel, M. Thiel, K. Bade, V. Saile, G. von Freymann, S. Linden, and M. Wegener, “Three-dimensional metal photonic nanostructures using direct laser writing and electrodeposition,” talk SCH A216, Spring Meeting of the Deutsche Physikalische Gesellschaft (DPG) in Dresden (Germany), March 22 – 27 (2009).
- J. K. Gansel, M. Thiel, M. Wegener, K. Bade, V. Saile, G. von Freymann, and S. Linden, “Polarizing properties of three-dimensional helical metamaterials,” talk ITuD3, Conference on Lasers and Electro-Optics / International Quantum Electronics Conference (CLEO/IQEC) in Baltimore (USA), May 31 – June 5 (2009).
- J. K. Gansel, M. Thiel, M. S. Rill, M. Decker, K. Bade, V. Saile, G. von Freymann, S. Linden, and M. Wegener, “Three-dimensional gold-helix photonic metamaterials made via two-photon direct laser writing,” **invited** talk 7586-14, Conference on Synthesis and Photonics of Nanoscale Materials (SPIE Photonics West) in San Francisco (USA), January 23 – 28 (2010).
- J. K. Gansel, M. Thiel, M. S. Rill, M. Decker, K. Bade, V. Saile, S. Burger, G. von Freymann, S. Linden, and M. Wegener, “Three-dimensional photonic metamaterials made by direct laser writing,” **invited** talk, Fourth International Congress on

Advanced Electromagnetic Materials in Microwaves and Optics (Metamaterials) in Karlsruhe (Germany), September 12 – 16 (2011).

- J. K. Gansel, M. Latzel, A. Frölich, J. Kaschke, M. Thiel, and M. Wegener, “Tapered gold helices as high-extinction-ratio, broadband circular polarizer,” talk QM2E.4, Conference on Lasers and Electro-Optics (CLEO) in San José (USA), May 6 – 11 (2012).

Further work published in the course of this thesis:

- F. B. P. Niesler, J. K. Gansel, S. Fischbach, and M. Wegener, “Metamaterial metal-based bolometers,” *Appl. Phys. Lett.* **100**, 203508 (2012).

Contents

Publications	i
1. Introduction	1
2. Fundamentals of Helical Metamaterials	5
2.1. Light-Matter Interaction in Isotropic Media	5
2.1.1. Macroscopic Maxwell Equations	5
2.1.2. Isotropic Media	6
2.1.3. Wave Propagation in Isotropic Media	7
2.1.4. Effective Parameter Models for Metals and Dielectrics	10
2.1.5. Optical Metamaterials	13
2.2. Polarization of Electromagnetic Plane Waves	18
2.2.1. Polarization States	19
2.2.2. Jones Calculus	21
2.2.3. Description of Asymmetric Transmission using Jones Calculus	22
2.3. Chiral and Bianisotropic Metamaterials	23
2.3.1. Geometrical Definition of Chirality	23
2.3.2. Bianisotropy and Chirality	25
2.3.3. Uniaxial Bianisotropy	28
2.3.4. Wave Propagation in Chiral Media	30
2.3.5. Optical Phenomena in Chiral Media	32
2.3.6. Helices as Metamaterial Building Blocks	34
2.3.7. Realizations of Chiral Optical Metamaterials	36
3. Fundamentals of Electrochemical Deposition	39
3.1. Basic Terms in Electrochemistry	39
3.2. Electrochemical Equilibrium	43
3.2.1. Interface between Electrode and Electrolyte Solution	43
3.2.2. Electrochemical Double-Layer	45
3.2.3. The Standard Potential	46
3.3. Electrochemical Deposition of Metals	47
3.3.1. Terminal Voltage and Current Flow	47
3.3.2. Metal Growth	48
3.4. Inversion of Nanostructured Templates	49
4. Fabrication of Helical Metamaterials	53
4.1. Fabrication Methods for Three-Dimensional Metamaterials	53
4.2. Our Fabrication Method	55

4.3.	Electrochemical Deposition of Gold	62
4.3.1.	Composition of the Electrolyte Solution	62
4.3.2.	Gold Deposition Process	63
4.3.3.	Inversion of Nanostructured Templates with Gold	66
4.4.	Electrochemical Deposition of Nickel	71
4.5.	Electrochemical Deposition of Copper(I) Oxide and Copper	73
5.	Characterization and Modeling Techniques	81
5.1.	Optical Characterization Setup	81
5.2.	Numerical Modeling of Helical Metamaterials	84
6.	Helical Optical Metamaterials	87
6.1.	Uniaxial Helical Metamaterials for Axial Propagation	87
6.1.1.	Optical Properties of Uniaxial Helical Metamaterials	87
6.1.2.	Dependence of the Optical Properties on Geometrical Parameters	91
6.1.3.	Helical Metamaterials as Broadband Circular Polarizers	97
6.1.4.	Helical Superlattices	100
6.2.	Helical Metamaterials for Oblique and Transversal Propagation	103
6.2.1.	Triaxial Helical Metamaterials for Oblique Propagation	104
6.2.2.	Uniaxial Helical Metamaterials for Transversal Propagation	105
6.3.	Uniaxial Tapered-Helix Metamaterials	106
6.3.1.	Optical Properties of Uniaxial Tapered-Helix Metamaterials	107
6.3.2.	Improved Broadband Circular Polarizer	109
7.	First Steps towards Metal-Dielectric Heterostructures	113
7.1.	Uniaxial Discontinuous-Helix Metamaterials	113
7.2.	Experimental Approach to Metal-Dielectric Heterostructures	115
8.	Conclusions and Outlook	119
A.	Appendix	123
A.1.	Wave Propagation in Chiral Media — Additional Equations	123
A.2.	Process Parameters of the used Photoresists	124
A.3.	Supplementary Results on Uniaxial Tapered-Helix Metamaterials	125
	Bibliography	140
	Abbreviations	141
	Acknowledgements	145

1. Introduction

Helical geometries surround us in our everyday life. A very illustrative example is a screw, used for the fastening of work pieces. The helical symmetry implies that through rotation and simultaneous translation along its long axis a screw will return to its original appearance, except for the screw head of course. Usually, screws are tightened by a clockwise rotation as they have a right-handed thread, and a screw with a left-handed thread can not be used with a right-handed internal thread. This reflects a general property of helical objects: there is a left-handed and a right-handed form (which is the mirror image of the left-handed form), and both forms can not be brought to coincide by rotations or translations [1]. Objects with this kind of asymmetry are called chiral. Besides screws, screw conveyors, mechanical springs or wind generators are examples for a mechanical use of helical shapes.

A helical shape which accompanies us constantly and, more precisely, is an essential part of life itself, is deoxyribonucleic acid (DNA). It consists of chiral molecules, and the stacking of these asymmetric building blocks leads to the well-known helical shape which is again chiral. In fact, many helical macromolecules and even more chiral molecules are known in chemistry. The most prominent example may be the right-handed glucose. The chiral properties of glucose are often used to determine its concentration in a solution *via* an optical measurement.

This brings us to the question how chirality and optics are connected. If an electromagnetic wave is circularly polarized, the orientation of the electric field vector rotates constantly while the wave is propagating. Thus, the tip of the electric field vector describes a helical line in space. By this means, we intuitively understand that chiral and helical symmetries play an important role in optics and that light can interact differently with chiral materials depending on whether they are right- or left-handed. As early as 1848, Louis Pasteur discovered that the chirality of a material has an influence on its optical properties [2]. He investigated the rotation of linearly polarized light after transmission through a solution of tartaric acid and found that the sense of rotation changed depending on whether the solution contained the left- or the right-handed form of the acid molecules.

This phenomenon is called optical activity and was theoretically described by Paul Drude in reference [3], where the rotation effect results from a spiral-like movement of electrons in a material. In 1920, Karl Ferdinand Lindman verified this theory experimentally with the use of randomly distributed metal helices on the size scale of one centimeter [4]. He measured an optical activity that depended on the wavelength of the used microwave radiation, thus connecting the effect to the size of the helices.

From today's viewpoint, one might call Lindman's setup a helical metamaterial for microwave radiation. The basic idea of optical metamaterials is to compose an artificial material by using metallic building blocks that are smaller than a certain wavelength of light. Thus, light of this or a larger wavelength will "see" an effective material instead of separate structures. By designing the building blocks, we can design the electron oscillations which are induced by light within these building blocks. By this means, we can introduce pre-designed properties to the material. The metamaterial concept yields the possibility to realize optical properties that are not known from natural materials. Proposals and realizations of fascinating properties at optical frequencies like magnetic resonances [5–7], a negative phase velocity [8–11], perfect lensing [12], and, within the concept of transformation optics, optical cloaking [13–15], have stimulated metamaterial research.

Using chiral building blocks, the tailoring of optical properties has added a further fascinating side to the field of metamaterials. Chiral metamaterials enable optical properties and phenomena like circular birefringence, circular dichroism, optical activity, negative phase velocities on a chiral route [16], and a control of the polarization state of light in general. In the past years, realizations of chiral optical metamaterials have shown [17–22] that much stronger chiral effects can be achieved through metamaterials than are known from natural materials like quartz crystals or the above mentioned chiral molecules.

Chiral optical materials can be used for applications like polarization rotation or circular polarization filters. Through metamaterials, the functionality of these devices could be improved while simultaneously decreasing their thickness by orders of magnitude and enabling an incorporation into miniaturized optical systems. This could be of particular interest for the infrared spectral region where it is often hard to find suitable components made of natural materials.

And there is even more potential within chiral metamaterials. The above mentioned chiral metamaterials were made of one or two functional layers of planar chiral building blocks. As chirality is an inherently three-dimensional phenomenon, one can expect much stronger chiral effects if three-dimensional building blocks would be used. However, the realization of such structures is challenging.

Within this thesis, we have developed a method which allows to fabricate three-dimensional metallic structures with feature sizes of half a micrometer. It combines the design flexibility of three-dimensional polymer templates made by direct laser writing [23–25] with the possibilities of high-quality microfabrication by template inversion using electrochemical metal deposition [26]. With this method, we have realized helical optical metamaterials that possess very strong chiral optical properties. Both numerical calculations and measurements show a pronounced circular dichroism in a wavelength range spanning one octave. Such structures can be used as compact broadband circular polarizers, thus yielding an early real-world application of metamaterials.

Outline of this thesis

In chapter 2, all that is necessary to understand the optical properties of helical metamaterials is introduced. The chapter is divided in three parts: First, an introduction to light-matter interactions in isotropic materials and metamaterials is given. This is followed by an overview of polarization optics and its description using Jones calculus. In the last part of chapter 2, we explain what chirality and bianisotropy are and how they are linked. Furthermore, we give detailed information on optical properties of chiral materials, helices as metamaterial building blocks, and, as a comparison to our work, realizations of chiral optical metamaterials.

Chapter 3 gives an introduction to the electrochemical side of this thesis, starting with an explanation of the basic terms used in electrochemistry and processes present at an electrode before and during electrochemical deposition. We also explain how a metal layer grows on macroscopic electrodes and in microscopically small channels.

Chapter 4 first summarizes different methods for the fabrication of three-dimensional metamaterials, pointing out the possibilities of our approach. Then, a detailed overview of the whole process is given and the electrochemical deposition of different materials used by us as well as the inversion of templates with these materials is explained.

In chapter 5, we present the optical spectroscopic characterization method and the numerical calculation methods used within this work.

Chapter 6 shows resulting fabricated helical optical metamaterials, optical measurements, and numerical calculations along with discussions of the optical properties.

The first part of chapter 6 is concerned with arrays of parallel helices suited for measurements with light incident parallel to the helix axis. These structures show strong circular dichroism in a wavelength range spanning almost one octave and thus could be used as broadband polarization filters for circularly polarized light. This design is extended by superlattices to study interactions of the single building blocks in a metamaterial.

In the second part, we are concerned with the optical properties of helical metamaterials for different angles of incidence, in particular for incidence of light normal to the helix axis.

The last part presents a tapered-helix metamaterial where the helix radius changes gradually along the helix axis. These structures were predesigned for use as an improved circular polarizer and have an even stronger and more broadband circular dichroism than helical metamaterials with a constant helix radius.

In chapter 7, we propose an extension of our fabrication process that allows for the realization of metal-dielectric heterostructures. We numerically analyze metamaterial arrays composed of electrically discontinuous helices and present our first experimental approaches to the realization of such heterostructures.

Finally, we summarize the work presented in this thesis within the conclusions. We also give an outlook on future possibilities of helical metamaterials and our fabrication method.

2. Fundamentals of Helical Metamaterials

In this chapter, we want to provide the knowledge that is necessary to understand the optical properties of helical metamaterials and the methods used to characterize them. In the first section, we describe how light interacts with different isotropic media, what metamaterials are, and why we are interested in three-dimensional (3D) metamaterials. In the introduction, we mentioned the effects of chiral media on polarized light. Thus, the second section is concerned with polarization optics and its description by Jones calculus. Helical metamaterials are chiral and, as we will see, bianisotropic. In the third section, we want to make clear what chirality is and how different bianisotropic materials are classified. There, we also describe optical properties of chiral media and of helical structures. We also summarize realizations of optical chiral metamaterials in order to provide a comparison to our work.

For detailed discussions and derivations, we point out books about optics in general [27–30] and books which include the discussion of bianisotropy [31, 32].

2.1. Light-Matter Interaction in Isotropic Media

In this section, we want to give an overview of light-matter interaction in media which possess effective material parameters, like many natural media and metamaterials. Starting with the Maxwell equations, we give a description of how electromagnetic waves interact with and propagate through media.

In the remainder of this section, we explain the effective parameters of natural materials and metamaterials. Metamaterials consist of artificial building blocks. Resonant electron oscillations, so called plasmons, in the building blocks allow to deliberately tailor the optical properties of metamaterials. We will describe this by using a well-known metamaterial building block, the split-ring resonator. The split-ring resonator is also important as we can use it to explain resonances in helical metamaterials.

2.1.1. Macroscopic Maxwell Equations

The temporal and spatial behavior of electromagnetic waves in media is described by the macroscopic Maxwell equations. In their differential form and in SI units they read

$$\nabla \times \vec{E}(\vec{r}, t) = -\frac{\partial}{\partial t} \vec{B}(\vec{r}, t), \quad (2.1)$$

$$\nabla \cdot \vec{D}(\vec{r}, t) = \rho(\vec{r}, t), \quad (2.2)$$

$$\nabla \times \vec{H}(\vec{r}, t) = \frac{\partial}{\partial t} \vec{D}(\vec{r}, t) + \vec{j}(\vec{r}, t), \quad (2.3)$$

$$\nabla \cdot \vec{B}(\vec{r}, t) = 0. \quad (2.4)$$

$\vec{E}(\vec{r}, t)$ denotes the electric field, $\vec{B}(\vec{r}, t)$ the magnetic induction, $\vec{D}(\vec{r}, t)$ the electric displacement and $\vec{H}(\vec{r}, t)$ the magnetic field. $\rho(\vec{r}, t)$ is the density of free charges and $\vec{j}(\vec{r}, t)$ the density of free currents. As free charges and currents do not play a role within this work, $\rho(\vec{r}, t)$ and $\vec{j}(\vec{r}, t)$ will be set to zero from here on.

The relation between the fields in a medium is expressed using the polarization $\vec{P}(\vec{r}, t)$ and the magnetization $\vec{M}(\vec{r}, t)$:

$$\vec{D}(\vec{r}, t) = \epsilon_0 \vec{E}(\vec{r}, t) + \vec{P}(\vec{r}, t), \quad (2.5)$$

$$\vec{H}(\vec{r}, t) = \frac{1}{\mu_0} \vec{B}(\vec{r}, t) - \vec{M}(\vec{r}, t), \quad (2.6)$$

with $\epsilon_0 = 8.85 \cdot 10^{-12} \frac{\text{As}}{\text{Vm}}$ being the permittivity of the vacuum and $\mu_0 = 4\pi \cdot 10^{-7} \frac{\text{Vs}}{\text{Am}}$ being the permeability of the vacuum. The electromagnetic properties of a medium are mirrored in the distinct form of $\vec{P}(\vec{r}, t)$ and $\vec{M}(\vec{r}, t)$. However, a medium needs to fulfill certain conditions in order to be able to express its properties in macroscopic terms.

2.1.2. Isotropic Media

When electromagnetic waves propagate through a medium, the electric and magnetic fields can induce fluctuations in the density of charges and currents. Thus, in general, one has to consider microscopic electric and magnetic fields at the same length scale as these fluctuations (or smaller). The properties of the medium are then directly described by the charge and current densities.

The charge density, for example in a molecule, can be described in terms of charges and electric dipole, quadrupole, and higher order moments. The charges contribute to a macroscopic charge density. The sum of the electric dipole moments is called the macroscopic polarization \vec{P} . Higher dipole moments can be usually neglected. Similarly, microscopic currents lead to a macroscopic current density and a magnetization \vec{M} which is the sum of the microscopic magnetic dipole moments, again neglecting higher magnetic moments [29]. If the wavelength of an electromagnetic wave is reasonably larger than the length scale of the charge and current fluctuations, spatial averaging, *i.e.* homogenization, is allowed and the macroscopic quantities can be used.

In natural materials like metals or dielectrics, the charge and current densities are due to electrons and nuclei. The arrangement of atoms in crystals can be resolved by x-ray diffraction while it cannot be resolved using conventional optical techniques. Thus, one can argue that for lengths larger than 10^{-8} m, macroscopic quantities can be applied [29]. In the optical spectral region (including ultraviolet and infrared wavelengths), shortest wavelengths are on the order of 10^{-7} m and hence the usage of macroscopic Maxwell equations is justified. Conditions for the homogenization of metamaterials will be discussed in section 2.1.5.

In the following, homogeneous linear and isotropic media will be considered. In linear media, $\vec{P}(\vec{r}, t)$ and $\vec{M}(\vec{r}, t)$ do not depend on higher powers of the external fields $\vec{E}(\vec{r}, t)$ and $\vec{H}(\vec{r}, t)$. This is justified as we do not consider light sources with extremely high intensities. In an isotropic medium, the optical properties are equal in all directions.

Media which are not isotropic will be discussed in section 2.3.

The polarization $\vec{P}(\vec{r}, t)$ and the magnetization $\vec{M}(\vec{r}, t)$ can still have complex dependencies of the external fields. For example, the polarization and the magnetization at a certain time t can depend not only on an external field at this time t , but also at all times before t (temporal dispersion). The same reasoning applies to the position \vec{r} , describing spatial dispersion: the polarization and the magnetization at one specific position can depend on the external fields at all positions. Therefore, it is advantageous to change to the frequency domain where this can be described more easily. The transition between time domain and frequency domain is done by using Fourier transforms.

In the frequency domain, even for non-harmonic waves, every spectral component of an electromagnetic wave can be treated as a monochromatic wave [29]. Maxwell's equations for the frequency domain have the form

$$\nabla \times \vec{E}(\vec{r}, \omega) = i\omega \vec{B}(\vec{r}, \omega), \quad (2.7)$$

$$\nabla \cdot \vec{D}(\vec{r}, \omega) = 0, \quad (2.8)$$

$$\nabla \times \vec{H}(\vec{r}, \omega) = -i\omega \vec{D}(\vec{r}, \omega), \quad (2.9)$$

$$\nabla \cdot \vec{B}(\vec{r}, \omega) = 0. \quad (2.10)$$

In isotropic media, the excited polarization (magnetization) is proportional to the exciting electric (magnetic) field. Then, also the relation between electric displacement and the electric field is proportional as well as the relation between the magnetic induction and the magnetic field. The properties of an isotropic medium can be described by the constitutive relations

$$\vec{D}(\vec{r}, \omega) = \varepsilon_0 \varepsilon(\omega) \vec{E}(\vec{r}, \omega), \quad (2.11)$$

$$\vec{B}(\vec{r}, \omega) = \mu_0 \mu(\omega) \vec{H}(\vec{r}, \omega), \quad (2.12)$$

where the electric permittivity $\varepsilon(\omega)$ and the magnetic permeability $\mu(\omega)$ are complex scalars. The dependence of the material parameters on ω is called dispersion. For easier reading, material parameters will be written without explicitly noting the frequency dependence (ω) from now on. The influence of the material parameters on the propagation of electromagnetic waves will be discussed in the following part of this section.

2.1.3. Wave Propagation in Isotropic Media

Using the constitutive relations (2.11) and (2.12), we can substitute $D(\vec{r}, \omega)$ and $H(\vec{r}, \omega)$ in the Maxwell equations (2.7) – (2.10). When we take the curl of (2.7) and use (2.8) and (2.9), we obtain the wave equation for the electric field:

$$\nabla^2 \vec{E}(\vec{r}, \omega) = -\frac{\omega^2}{c_0^2} \varepsilon \mu \vec{E}(\vec{r}, \omega), \quad (2.13)$$

where $c_0 = \frac{1}{\sqrt{\epsilon_0\mu_0}} = 3 \cdot 10^8 \frac{\text{m}}{\text{s}}$ is the speed of light in vacuum. Using the same procedure for (2.9), we obtain the wave equation for the magnetic induction:

$$\nabla^2 \vec{B}(\vec{r}, \omega) = -\frac{\omega^2}{c_0^2} \epsilon \mu \vec{B}(\vec{r}, \omega). \quad (2.14)$$

These equations are solved by a monochromatic plane wave [28]. In the time domain, it has the form:

$$\vec{E}(\vec{r}, t) = \vec{E}_0 e^{i(\vec{k}\vec{r} - \omega t)}, \quad (2.15)$$

$$\vec{B}(\vec{r}, t) = \vec{B}_0 e^{i(\vec{k}\vec{r} - \omega t)}, \quad (2.16)$$

with \vec{E}_0 and \vec{B}_0 being constant vectors. \vec{k} is the wave vector which points in the propagation direction of the wave fronts. When inserting (2.15) and (2.16) into the Maxwell equations (2.7) and (2.9), we see that $\vec{E}(\vec{r}, t)$, $\vec{B}(\vec{r}, t)$ and \vec{k} are orthogonal to each other and form a right-handed set of vectors:

$$\vec{k} \times \vec{E}(\vec{r}, t) = \omega \vec{B}(\vec{r}, t). \quad (2.17)$$

Such a wave is called a transverse electromagnetic wave. It is important to keep the orthogonality in mind for the later reasoning on chiral metamaterials.

For an isotropic medium, the wave vector \vec{k} has the same value k in all directions. It can be written in the form

$$k = \frac{\omega}{c_0} \sqrt{\epsilon \mu} = k_0 n, \quad (2.18)$$

where $k_0 = \frac{\omega}{c_0}$ is the wave vector value in vacuum. The ratio $c = \frac{\omega}{k}$ is the phase velocity. It can also be expressed in terms of the wavelength $\lambda = \frac{2\pi}{k}$ and the frequency $f = \frac{\omega}{2\pi}$ as $c = f\lambda$. n is the refractive index:

$$n^2 = \epsilon \mu. \quad (2.19)$$

We remind that both ϵ and μ can be frequency-dependent and hence k depends on the frequency, too. Thus, equation (2.18) is called the dispersion relation as it expresses the dispersion of a medium. As ϵ and μ are complex numbers, we can express the refractive index in terms of a real and an imaginary part:

$$n = n' + in''. \quad (2.20)$$

Inserting this into equation (2.15), the plane wave can be split into a propagating part and an exponentially decaying part:

$$\vec{E}(\vec{r}, t) = \vec{E}_0 e^{-n'' \vec{k}_0 \vec{r}} e^{i(n' \vec{k}_0 \vec{r} - \omega t)}. \quad (2.21)$$

Here, we see clearly that n' determines the phase of the propagating part. n'' causes an

exponential decay of the wave and thus describes damping. Obviously, \vec{E}_0 determines the spatial orientation of the electric field. This is called the polarization of the electromagnetic wave and will be discussed in section 2.2.

While the wave vector determines the propagation direction of the wave fronts of an electromagnetic wave, the flow of electromagnetic energy is given by the pointing vector \vec{S} :

$$\vec{S}(\vec{r}, t) = \frac{1}{\mu_0} \text{Re}\{\vec{E}(\vec{r}, t)\} \times \text{Re}\{\vec{B}(\vec{r}, t)\}. \quad (2.22)$$

It gives the energy crossing a unit area perpendicular to \vec{S} per second. ‘‘Re’’ denotes that the physically meaningful, real parts of the fields should be used. \vec{S} does not necessarily point in the same direction as \vec{k} . In isotropic media with a negative refractive index, they point in opposite directions [8]. In anisotropic or bianisotropic media, they can include an angle often called the spatial walkoff angle.

Transmission and Reflection

When a wave encounters an interface between two media, usually part of it is transmitted and part is reflected. This depends on the impedance Z . It is defined as the ratio between the electric and the magnetic field amplitudes:

$$Z = \frac{E_0}{H_0} = \sqrt{\frac{\mu_0 \mu}{\epsilon_0 \epsilon}}. \quad (2.23)$$

For example, an electromagnetic wave with \vec{k} normal to an interface between two media (normal incidence) will not be reflected unless the two media have different impedances. The ratio between the electric field amplitude of the wave before the interface, $E_{0,i}$, and behind the interface, $E_{0,t}$, is called the transmission coefficient t . Similarly, a reflection coefficient r is defined as the ratio between incident and reflected field amplitudes. Quantitative information on the reflection and transmission coefficients and phase-shifts at interfaces can be extracted using the Fresnel equations (see, *e.g.* [27, 28]):

$$r_{\perp} = \left(\frac{E_{0,r}}{E_{0,i}} \right)_{\perp} = \frac{\frac{n_i}{\mu_i} \cos(\theta_i) - \frac{n_t}{\mu_t} \cos(\theta_t)}{\frac{n_i}{\mu_i} \cos(\theta_i) + \frac{n_t}{\mu_t} \cos(\theta_t)}, \quad (2.24)$$

$$t_{\perp} = \left(\frac{E_{0,t}}{E_{0,i}} \right)_{\perp} = \frac{2 \frac{n_i}{\mu_i} \cos(\theta_i)}{\frac{n_i}{\mu_i} \cos(\theta_i) + \frac{n_t}{\mu_t} \cos(\theta_t)}, \quad (2.25)$$

$$r_{\parallel} = \left(\frac{E_{0,r}}{E_{0,i}} \right)_{\parallel} = \frac{\frac{n_t}{\mu_t} \cos(\theta_i) - \frac{n_i}{\mu_i} \cos(\theta_t)}{\frac{n_i}{\mu_i} \cos(\theta_i) + \frac{n_t}{\mu_t} \cos(\theta_t)}, \quad (2.26)$$

$$t_{\parallel} = \left(\frac{E_{0,t}}{E_{0,i}} \right)_{\parallel} = \frac{2 \frac{n_i}{\mu_i} \cos(\theta_i)}{\frac{n_i}{\mu_i} \cos(\theta_t) + \frac{n_t}{\mu_t} \cos(\theta_i)}, \quad (2.27)$$

where θ is the angle between \vec{k} and the interface normal. The electric field vectors are polarized either parallel (\parallel) or perpendicular (\perp) to the plane of incidence (a plane nor-

mal to the interface and containing the wave vector). The indices indicate whether values before (i) or behind (t) the interface should be inserted.

Usually, one is interested in the intensity reflectance and transmittance (also called reflectivity and transmissivity [30]) as these are easily accessible experimentally. They are defined as the ratio of the light intensity at a unit area of the interface before and after it [30], where the light intensity is a temporal average of the absolute value of the pointing vector. The resulting expressions for the reflectance R and the transmittance T are

$$R = |r^2|, \quad T = \left| \frac{\sqrt{\frac{\varepsilon_t}{\mu_t}} \cos(\theta_t)}{\sqrt{\frac{\varepsilon_i}{\mu_i}} \cos(\theta_i)} \right| |t^2|. \quad (2.28)$$

In general, these values depend on the material parameters, on the angle of the wave vector of the incident wave with respect to the interface normal, and on the polarization of the incident wave.

2.1.4. Effective Parameter Models for Metals and Dielectrics

The effective permittivities of metals and dielectrics can be described using the Drude model and the Lorentz model, respectively. In both cases, electromagnetic waves can excite oscillations of electrons in the material that lead to a macroscopic polarization. A magnetization is not excited and thus the permeability μ can be set to one for natural materials at optical frequencies.

The Lorentz Model

The Lorentz model is used for the description of dielectrics. As we will consider metal-dielectric heterostructures later on, and as plasmon resonances are similar to a Lorentz oscillator, we explain it shortly here. In the Lorentz model, electrons are bound to atomic nuclei *via* a restoring force and form an oscillator with the eigenfrequency ω_0 . When applying an external electromagnetic field $\vec{E}(\vec{r}, t) = \vec{E}_0 e^{i(\vec{k}\vec{r} - \omega t)}$, a driven harmonic oscillator results.

Without loss of generality, we consider oscillations in the \hat{x} -direction. A shift $x(\omega, t)$ causes a polarization $P = N_e e x(\omega, t)$, where N_e is the electron density and $e = 1.6 \cdot 10^{-19}$ C is the elementary charge.

The motion of the electron gas is described by a differential equation which contains a phenomenological damping constant Γ :

$$m_e \frac{\partial^2 x(\omega, t)}{\partial t^2} + m_e \Gamma \frac{\partial x(\omega, t)}{\partial t} + m_e \omega_0^2 x(\omega, t) = e E_0 e^{i(\vec{k}\vec{r} - \omega t)}, \quad (2.29)$$

where m_e is the effective electron mass. Through inserting the solution of the differential equation into the expression for the polarization and using the material equation (2.11), we obtain the frequency dependent electric permittivity of a dielectric:

$$\varepsilon = 1 + \frac{e^2 N_e}{\varepsilon_0 m_e (\omega_0^2 - \omega^2 - i\Gamma\omega)}. \quad (2.30)$$

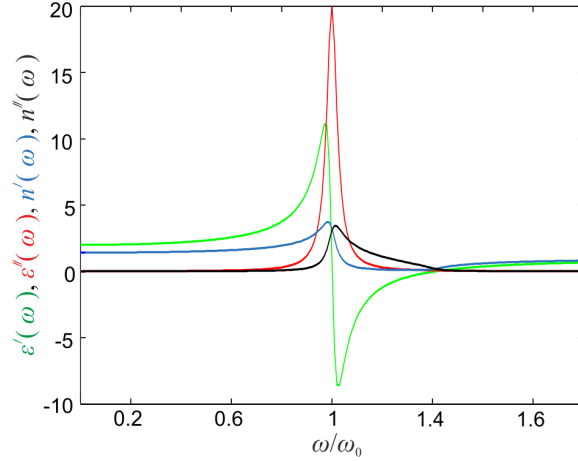


Figure 2.1 Real and imaginary part of the electric permittivity and the refractive index for the Lorentz model with a damping constant $\Gamma = 0.05 \omega_0$.

The resulting real and imaginary parts of the electric permittivity $\varepsilon = \varepsilon' + i\varepsilon''$ and the refractive index are shown in figure 2.1. For frequencies sufficiently far away from the eigenfrequency ω_0 , the real part of the permittivity is positive and the imaginary part is small. Then, the refractive index has a vanishing imaginary part and light can propagate through the medium with a small attenuation.

The Drude Model

The Drude model is a classical description of the dispersion in metals. It assumes that in metals, a free electron gas surrounds fixed nuclei. In the presence of an electromagnetic field, the electrons will oscillate relative to the nuclei depending on the frequency of the incident field. The motion of the electron gas is described by a differential equation which contains a phenomenological damping constant ω_{col} , the collision frequency. In contrast to the Lorentz model, it does not contain a term $m_e \omega_0^2 x(\omega, t)$. The differential equation reads

$$m_e \frac{\partial^2 x(\omega, t)}{\partial t^2} + m_e \omega_{\text{col}} \frac{\partial x(\omega, t)}{\partial t} = e E_0 e^{i(\vec{k}\vec{r} - \omega t)}. \quad (2.31)$$

Again, using its solution and the material equations, one obtains ε :

$$\varepsilon = 1 - \frac{\omega_{\text{pl}}^2}{\omega^2 + i\omega_{\text{col}}\omega}, \quad (2.32)$$

$$\omega_{\text{pl}} = \sqrt{\frac{e^2 N_e}{\varepsilon_0 m_e}}. \quad (2.33)$$

The plasma frequency ω_{pl} depends on the electron density and the effective electron mass of the material in question. Figure 2.2 shows the course of the real and the imaginary part of the permittivity and the refractive index. The parameters for gold (Au), copper

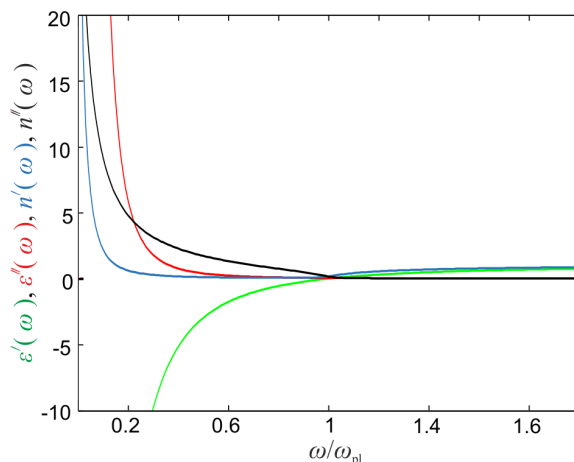


Figure 2.2 Real and imaginary part of the electric permittivity for a damping of $\omega_{\text{col}} = 0.05 \omega_{\text{pl}}$. The angular frequency ω is normalized to the plasma frequency.

(Cu) [33, 34], and nickel (Ni) [35, 36] are shown in table 2.1. As later measurements are done in the infrared, we show parameters for the infrared (denoted by “ir”) spectral region [33, 35]. For a comparison, we also show parameters for the visible (denoted by “vis”) spectral region [34, 36].

For all three metals in table 2.1, the plasma frequency is higher than frequencies corresponding to infrared wavelengths. In figure 2.2, we see that in this case the real part of ϵ is negative. Then, the refractive index has a large imaginary part. This means that propagation is strongly attenuated in metals and that only evanescent waves can penetrate. The metal thickness after which the field intensity has fallen to a factor of $1/e$ (e is Euler’s number) is called the skin depth. In metals it is at the scale of tens of nanometers for optical frequencies. Figure 2.3 shows the dispersion for the three metals used within this work. As we will see in the following section, the plasma frequency is crucial for the realization of plasmonic metamaterials. Au and Cu have plasma frequencies in the green part of the visible spectral region, which makes them interesting for the realization of plasmonic structures at longer wavelengths. In order to keep ohmic losses small, a low imaginary part of the permittivity is important [37]. This is why Au is preferred in comparison to Cu and Ni for the fabrication of metamaterial structures.

Table 2.1 Plasma- and collision frequency of gold (Au), copper (Cu) [33, 34], and nickel (Ni) [35, 36] for the visible (vis) and the infrared (ir) spectral region.

	Au	Cu	Ni
$\omega_{\text{pl,ir}} (10^{16} \frac{\text{rad}}{\text{s}})$	1.37	1.20	0.88
$\omega_{\text{pl,vis}} (10^{16} \frac{\text{rad}}{\text{s}})$	1.37	1.30	1.26
$\omega_{\text{col,ir}} (10^{14} \frac{\text{rad}}{\text{s}})$	0.37	0.75	1.62
$\omega_{\text{col,vis}} (10^{14} \frac{\text{rad}}{\text{s}})$	1.21	1.61	13.66

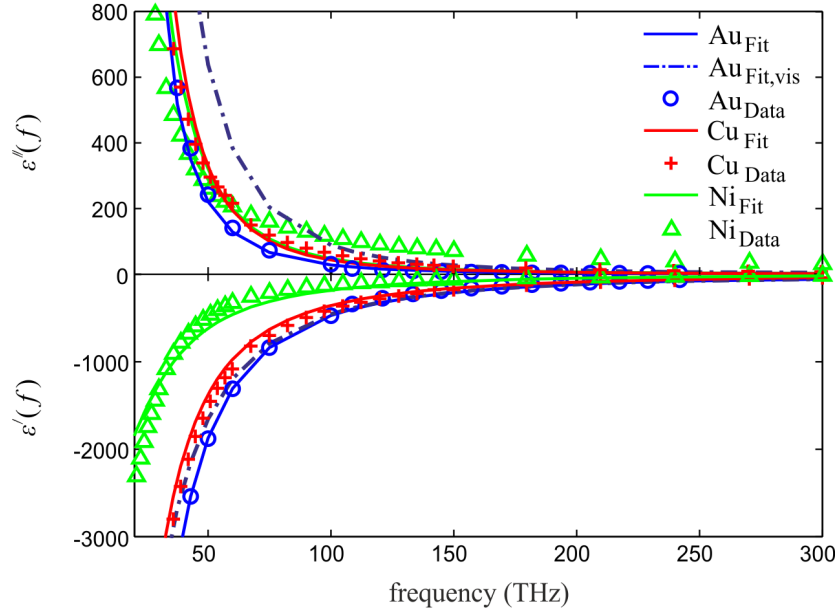


Figure 2.3 Imaginary and real parts of the electric permittivity for Au, Ni, and Cu in the infrared spectral region (data obtained from [33,35]). Please note the different scales for the imaginary and the real part. For Au, a fit for visible frequencies is shown as a comparison (fit data according to [34]).

The deviations between measured data and the drude fits are due to interband transitions and further resonances at higher frequencies. In order to take this into account, (2.32) can be extended by a frequency independent offset usually named ε_∞ and additional Lorentz terms.

2.1.5. Optical Metamaterials

For the build-up of optical metamaterials, usually metallic building blocks are used. If the building blocks and their mutual distance are sufficiently small with respect to a certain wavelength, the resulting material can be considered as homogeneous for this wavelength. We saw that in natural materials, oscillations of bound or free electrons determine the permittivity of these materials for optical frequencies. By carefully designing resonant electron oscillations in the metallic building blocks, the optical properties of a metamaterial can be deliberately controlled. This allows for the realization of materials with optical properties that are not present in natural materials. Examples are metamaterials with a permeability different from the value one [5–7] or a negative permittivity and permeability leading to a negative refractive index [8–11].

Until now, there is no common understanding on the exact conditions for homogenization in plasmonic metamaterials. Let us assume that a metamaterial consists of periodically arranged metal nanostructures with a lattice constant a on a substrate with refractive index n_{sub} . Then, the free-space wavelength λ has to be sufficiently bigger than a .

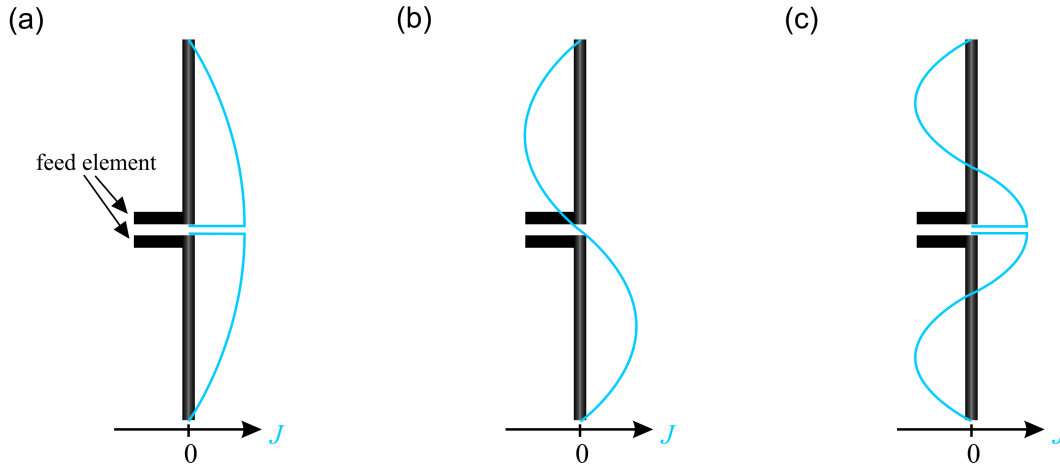


Figure 2.4 Current distribution along an antenna at resonant wavelengths for (a) $m = 1$, (b) $m = 2$, and (c) $m = 3$.

However, a broad spectrum for the ratio λ/a can be found in literature. While in [38], a ratio $\lambda/a \approx 1$ is said to be sufficient, at least $\lambda/a = 100$ is required according to [39]. In [40, 41], discussions and hints to recent publications on this topic can be found.

Within this thesis, we assume that metamaterials can be treated as homogeneous materials when the condition $\lambda/(n_{\text{sub}} \cdot a) > 1$ is fulfilled. This excludes diffraction orders higher than zero [27]. However, it does not exclude phase retardation effects for wavelengths near this limit [42], which should be kept in mind.

Radio Antennas as Macroscopic Analog for Metamaterial Building Blocks

How do resonances in metamaterial building blocks evolve? First, let us look at a macroscopic analog for particle plasmons, namely radio antennas. A straight radio antenna (figure 2.4) can be excited resonantly by applying an alternating current through the two feed elements. It will emit electromagnetic radiation with a wavelength λ that depends on the length of the antenna.

Reversely, electromagnetic radiation can couple to the antenna. The electric field component drives the electrons to one end of the antenna. When the exciting electric field is zero, the electrons relax towards the other end and a sinusoidal current with maximal value in the middle of the antenna is present. It can be fed into an electric circuit *via* the feed elements. The resonant wavelength is proportional to the length l of the antenna: $\lambda = m \frac{l}{2}$, ($m \in \mathbb{N}$). Obviously, resonances shift to longer wavelengths with increasing wire lengths. The so called *fundamental resonance* or *fundamental mode* is present for $m = 1$, followed by higher modes for higher values of m . In figure 2.4, this is depicted by the current J present in an antenna at a time when the driving electric field is zero. With increasing value of m , the number of positions with zero current (current nodes) increases like $m - 1$. When driven by a current, the antenna in the fundamental mode has an emission characteristic which is very similar to a dipole.

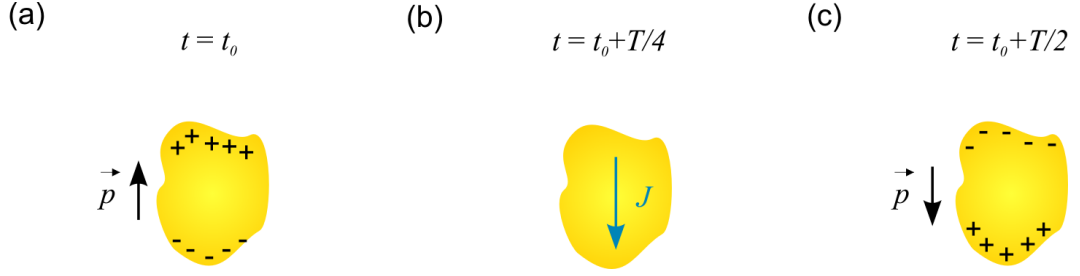


Figure 2.5 Metal nanoparticle under the influence of an electromagnetic field at different times. (a) $t = t_0$, (b) $t = t_0 + T/4$, and (c) $t = t_0 + T/2$.

Resonances in Optical Metamaterials

In contrast to a bulk metal, in metal nanostructures the electrons are confined to a limited volume. When an electromagnetic wave arrives at a nanostructure, it interacts with its electrons and is partially scattered and partially absorbed. This has been described by Mie [43] analytically for a metallic sphere. If a nanostructure is small compared to the wavelength of the incident electromagnetic wave, the quasistatic approximation can be used for calculations. Then, one can assume that at any given time, the incident electric field is constant throughout the nanostructure size. For complex structures or nanostructures with a size similar to the wavelength, usually numerical calculations are necessary.

In contrast to macroscopic antennas, plasmonic nanostructures are driven by electromagnetic waves at optical frequencies. While the electrons follow the exciting field almost directly for a small (radio) frequency, they start to drag behind when the frequency is increased towards the optical region. This is due to the effective electron mass m_e . The phase difference between exciting field and electron movement increases until it reaches a value of $\frac{\pi}{2}$ and a maximal amplitude of the oscillations [37]. At this point, the absorbed energy is maximal.

Figure 2.5 (a) depicts the resonance of a particle at a time t_0 , where the exciting electric field component of the electromagnetic wave has driven the electron gas towards one end of the particle. This results in an electric dipole moment \vec{p} of the particle oriented antiparallel with respect to the electric field and causes a restoring force on the electrons. A quarter period $T/4$ later, the electron gas relaxes into the particle leading to a current J as shown in figure 2.5 (b). Another quarter period later, the electric dipole moment is maximal in opposite direction (figure 2.5 (c)) and so on. The resonances of the system depend on the structure size, design, and material.

Split-Ring Resonators as Metamaterial Building Blocks

Split-ring resonators are very common metamaterial building blocks which exhibit a magnetic resonance, leading to a permeability different from one ($\mu \neq 1$) at optical frequencies. Moreover, they will be helpful to understand the resonances in helical metamaterials. The split-ring resonator design [5, 44] was proposed for the use as a metamaterial building

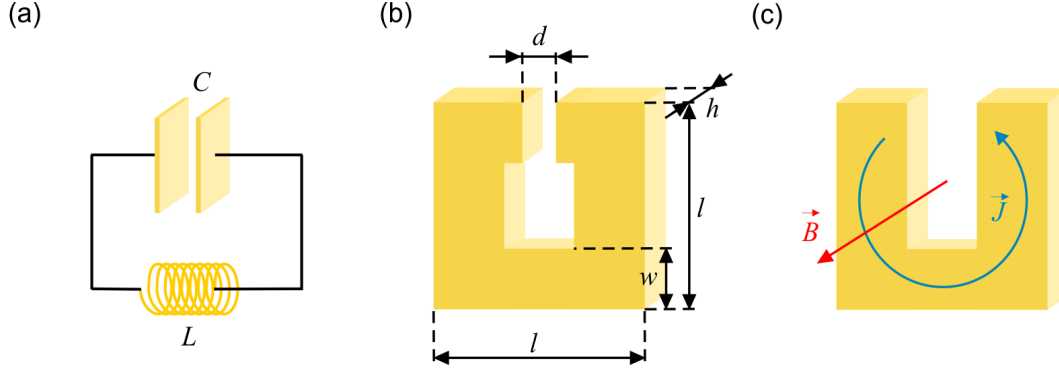


Figure 2.6 Split-ring resonator as a metamaterial building block. (a) Comparison to a LC circuit, (b) a split-ring resonator, and (c) depiction of the magnetic field B resulting from the current J .

block in 1999 by J. B. Pendry [5]. It imitates a LC circuit with an inductivity L and a capacitance C (figure 2.6 (a)). In such a circuit, the energy oscillates between the electric field building up between the capacitor plates, and the magnetic field present in the coil. In the split-ring resonator (figure 2.6 (b)), the slit resembles a plate capacitor and the ring represents one turn of a coil. Similar to a coil, a circulating current in the ring results in a magnetic field perpendicular to it (figure 2.6 (c)), and thus a magnetic dipole.

The LC circuit has a resonance frequency $\omega_{LC} = \frac{1}{\sqrt{LC}}$. Using the geometry parameters in figure 2.6 (b) and the formulas for a plate capacitor and a long coil, the resonance frequency can be estimated (see, *e.g.* [45]):

$$\omega_{LC} = \frac{c_0}{l\sqrt{\varepsilon_m}} \sqrt{\frac{d}{w}}, \quad (2.34)$$

where ε_m is the permittivity of the surrounding medium. As d and w usually are on the same order of magnitude, the spectral resonance position depends strongly on the length l of the split-ring resonator. The resulting permeability μ for an array of split-ring resonators with periodicity a_v , $v = [x, y, z]$, in the respective spatial directions can also be calculated [45]. Apart from a frequency in the nominator, the expression equals the permittivity of an undamped Lorentz oscillator.

Electromagnetic waves can couple in two ways to the magnetic resonance: Either directly by a magnetic field component H parallel to the magnetic dipole m of the split-ring resonator, or by an electric field component E parallel to the slit, thus inducing a circulating current. The second possibility is more convenient as split-ring resonator arrays are usually fabricated as planar layer on a substrate. Thus, coupling with the electric field allows for normal incidence of light onto the substrate. Figure 2.7 (a) shows a scanning electron microscope (SEM) picture of an array of fabricated split-ring resonators. Transmission and reflection spectra of this array under normal incidence and with the electric field polarized parallel to the slit of the resonators are shown in figure 2.7 (b) [7]. The dip in the transmission at 1500 nm corresponds to the magnetic

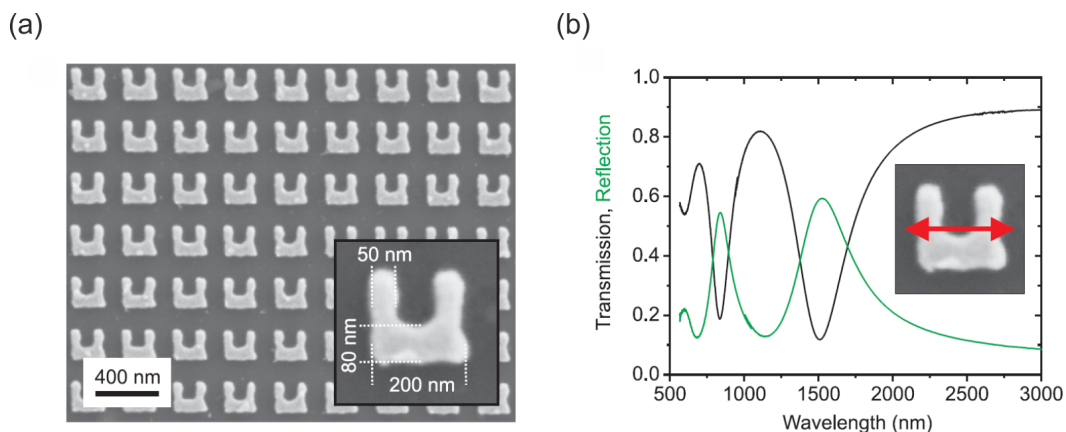


Figure 2.7 Split-ring resonator metamaterial. (a) SEM picture of an array with split-ring resonators. The inset shows a single structure with the geometrical sizes. The thickness of the Au structures is 30 nm. (b) Transmission (black) and reflection (green) spectra of the array shown in (a). In the inset, the red arrow indicates the polarization of the electric field component. Light is incident normal to the split-ring resonator plane [7]. (©2012 by the American Physical Society)

resonance discussed above. It is the fundamental resonance. Similar to a wire antenna, higher resonant modes with increasing number of current nodes are present in split-ring resonators. Please note that these modes are connected to electric resonances. The transmittance dip at 700 nm corresponds to a higher resonant mode with two current nodes at the edges of the split-ring resonator. The higher mode with one current node can be excited by an electric field that is polarized perpendicular to the slit of the resonators.

Three-Dimensional and Bulk Metamaterials

Planar building blocks, like the split-ring resonators discussed above, allow to tailor metamaterials with many interesting properties. However, some properties, in particular strong chirality, can only be achieved by using 3D building blocks. In addition, the interaction volume is increased in 3D structures in comparison to planar structures.

For planar metamaterials with several layers, experiments have shown that the metamaterial properties do depend on the number of layers [46–48], which encourages the fabrication of 3D metamaterials when aiming at bulk metamaterials.

Another example for the importance of 3D building blocks is isotropy. The split-ring resonator metamaterial discussed above is, strictly speaking, not an isotropic metamaterial. As we discussed, the material parameters depend on the orientation of the electric and magnetic field vectors with respect to the split-ring resonator orientation on the substrate. The material parameters also change depending on the angle of incidence of light as is discussed in [7]. Thus, the condition of the material parameters being independent of the direction in which light propagates through the medium, is not fulfilled. In order to create an isotropic split-ring resonator metamaterial, one could imagine a random distribution of arbitrarily oriented building blocks. However, such a completely random distribution is hard to achieve experimentally. The lack of isotropy was addressed already in 1999 by

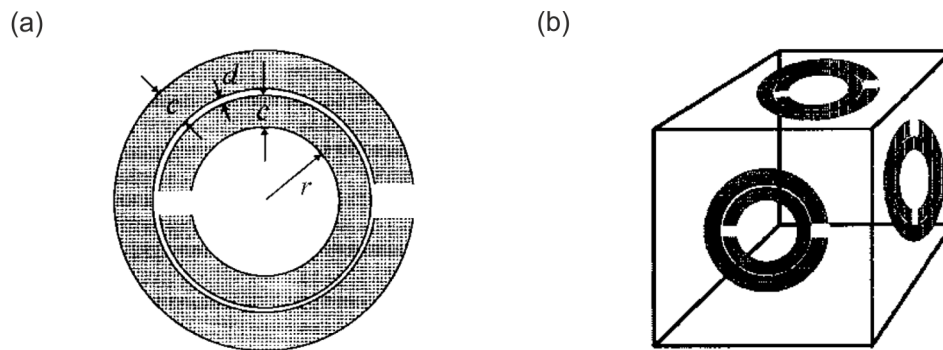


Figure 2.8 Cubic building block proposed in [5]. (a) Split-ring resonator design, and (b) arrangement in the unit cell of a cubic lattice. (©2012 by IEEE)

J. B. Pendry [5] and a cubic building block (figure 2.8) was proposed in order to achieve more isotropic metamaterials.

The mentioned points should make clear that it is highly desirable to fabricate 3D metamaterial structures. In the last years, designs with 3D structures have been proposed [5,49–51] and methods have been developed which allow to fabricate 3D structures or several layers of planar structures. In section 4.1, we will give an overview of existing fabrication methods and describe the method we developed.

2.2. Polarization of Electromagnetic Plane Waves

We want to start the section about polarization by stating what *unpolarized* light is. Sources like the sun or a light bulb irradiate natural light which is unpolarized. This light is generated by many atoms which emit electromagnetic waves randomly. Let us consider the superposition of electromagnetic waves with one frequency. When looking along one certain propagation direction at a fixed time, the orientation (and the amplitude) of the electric field vector changes arbitrarily within different planes normal to the wave vector. Thus, an unpolarized wave has a randomly changing polarization in space and time.

In contrast, in optics we usually want a well-defined situation where we can predict what value an electromagnetic wave will take at a certain time and position. For this purpose, it is crucial to control the polarization state. This is particularly the case when bianisotropic or chiral media are involved, as they can possess quite different properties for different polarizations.

In the following, we will describe different polarization states of a transverse electromagnetic wave and show that they are eigenpolarizations of an isotropic medium. We will also introduce the Jones calculus that can be used to represent and calculate polarization states of plane waves which have been transmitted or reflected through a helical metamaterial.

2.2.1. Polarization States

Imagine a transverse electromagnetic wave propagating along the positive z -direction of a Cartesian coordinate system in an isotropic medium. Using the unit vectors \hat{x} , \hat{y} and \hat{z} , the electric field can be written as

$$\vec{E}(\vec{r}, t) = \begin{pmatrix} E_x \\ E_y \end{pmatrix} e^{i(\vec{k}\hat{z}-\omega t)} = \hat{x}E_{0,x}e^{i(\vec{k}\hat{z}-\omega t)} + \hat{y}E_{0,y}e^{i\phi}e^{i(\vec{k}\hat{z}-\omega t)}. \quad (2.35)$$

The factor $e^{i\phi}$ expresses, that a phase-shift (with the phase ϕ) can be present between the two components in (2.35). We rewrite the equation for the physically relevant, real part of the electric field $\vec{\mathcal{E}}(\vec{r}, t) = \text{Re}\{\vec{E}(\vec{r}, t)\}$:

$$\vec{\mathcal{E}}(\vec{r}, t) = \hat{x}E_{0,x} \cos(kz - \omega t) + \hat{y}E_{0,y} \cos(kz - \omega t + \phi). \quad (2.36)$$

For $E_{0,y} = 0$, the wave is polarized along the x -direction. At a position z_0 , the electric field vector oscillates parallel to the x -axis with time, and at a certain time t_0 , it describes a sinusoidal curve in the xz -plane (figure 2.9 (a)). This is a linear polarization which can more specifically be called x -polarization. If $E_{0,y} \neq 0$ and $\phi = 0$, the superposition of the two vector components has a constant orientation and the wave is still linearly polarized. An unpolarized electromagnetic wave can be polarized linearly by a linear polarizer. In the simplest case of a so called wire-grid polarizer, this can be a layer of parallel metal wires with a period smaller than the wavelength — we could call this a metamaterial. The components of the incident light which are oriented parallel to the wires will couple to them and be reflected while components which are oriented perpendicular to the wires will be transmitted. Thus, the transmitted light will be polarized perpendicular to the wires.

When both components have the same amplitude value, $E_{0,x} = E_{0,y} = E_0$, but a phase difference of $\phi = \pm\pi/2$, the wave has a circular polarization. For $\phi = -\pi/2$, it can be written in the form

$$\vec{\mathcal{E}}(\vec{r}, t) = \hat{x}E_0 \cos(kz - \omega t) + \hat{y}E_0 \sin(kz - \omega t). \quad (2.37)$$

When we calculate the length of the vector $\vec{\mathcal{E}}(\vec{r}, t)$, we see that it is equal to E_0 at all times and positions. At a position z_0 , the electric field vector rotates clockwise in the xy -plane when looked at from the receiver (against the propagation direction). This is depicted in the upper row of figure 2.9 (b). The lower row shows the spatial behavior for a specific time t_0 . We see that the electric field vector describes a helix with its axis parallel to \hat{z} . As this helix rotates with the same sense as a right hand does when the thumb is parallel to z -direction, this is called right-circular polarization (RCP). The polarization with the opposite sense of rotation is called left-circular polarization (LCP) and is shown in figure 2.9 (c). If the phase difference is $\phi = \pi/2$, a plane wave has LCP¹.

¹Sometimes a plane wave is defined differently from (2.35): the exponential term in (2.35) is written as $e^{-i(kz-\omega t)}$. Then $\phi = -\pi/2$ leads to LCP while $\phi = \pi/2$ leads to RCP. The temporal and spatial behavior of the electric field for a specific polarization remains as described above.

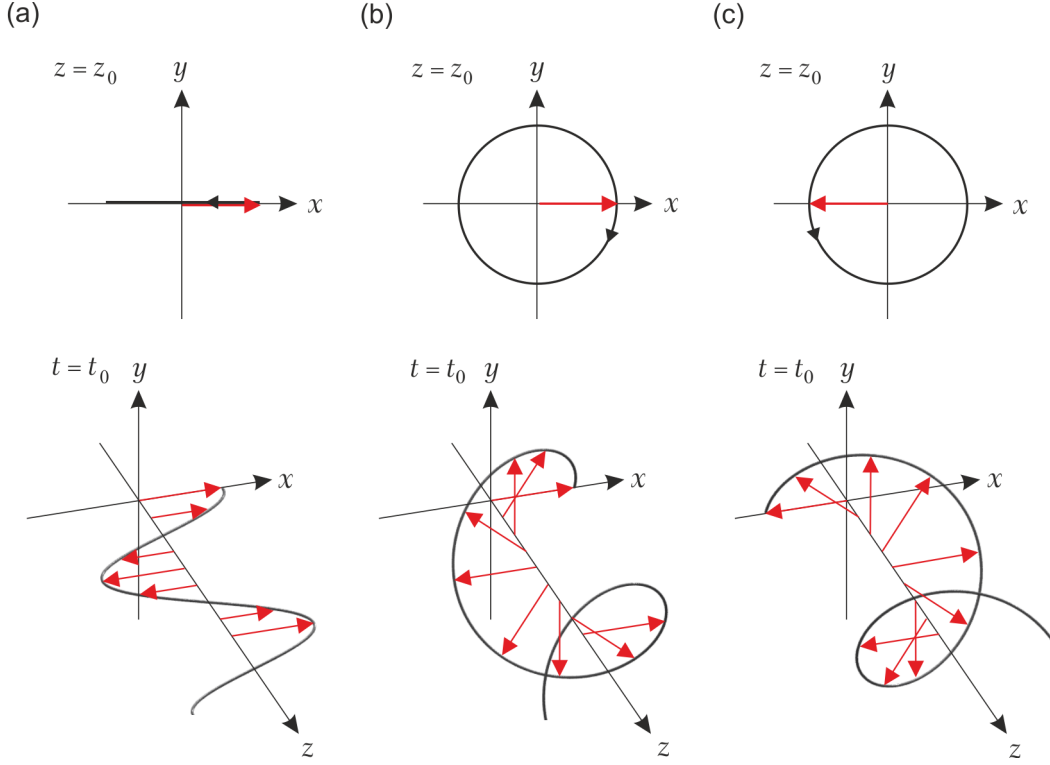


Figure 2.9 Depiction of polarization states. In the upper row, the states are depicted at a certain position $z = z_0$ while in the lower row, they are depicted at a fixed time $t = t_0$. The red arrows are electric field vectors while the thick black lines and arrows mark the way of the tip of the electric field vector in time (upper row) and space (lower row). (a) Linear polarization, (b) right-circular polarization (RCP), and (c) left-circular polarization (LCP).

A circular polarization is usually achieved by first polarizing the incident light linearly. Then, it is transmitted through a wave retarder (see section 5.1) to adjust circular polarization.

For other values of ϕ , $E_{0,x}$, and $E_{0,y}$ the wave is in general elliptically polarized. In that case, the electric field vector at a specific position describes an ellipse in time and for a specific time, it describes a flattened helix along the z -direction. It can be shown (see, *e.g.*, [27]) that the ellipse is given by

$$\left(\frac{\vec{\mathcal{E}}\hat{x}}{E_{0,x}}\right)^2 + \left(\frac{\vec{\mathcal{E}}\hat{y}}{E_{0,y}}\right)^2 - 2\left(\frac{\vec{\mathcal{E}}\hat{x}}{E_{0,x}}\right)\left(\frac{\vec{\mathcal{E}}\hat{y}}{E_{0,y}}\right)\cos(\phi) = \sin^2(\phi) \quad (2.38)$$

and its major semi-axis includes an angle α with the x -axis given by

$$\tan(2\alpha) = 2\frac{E_{0,x}E_{0,y}}{E_{0,x}^2 - E_{0,y}^2}\cos(\phi). \quad (2.39)$$

Table 2.2 Normalized Jones vectors in the linear basis for linear and circular polarization states. α is the angle between the polarization direction and the x -axis.

linear polarization		circular polarization	
x-polarization	$\vec{J}_{L,x} = \begin{pmatrix} 1 \\ 0 \end{pmatrix}$	RCP	$\vec{J}_{L,RCP} = \frac{1}{\sqrt{2}} \begin{pmatrix} 1 \\ -i \end{pmatrix}$
with angle α	$\vec{J}_{L,\alpha} = \begin{pmatrix} \cos(\alpha) \\ \sin(\alpha) \end{pmatrix}$	LCP	$\vec{J}_{L,LCP} = \frac{1}{\sqrt{2}} \begin{pmatrix} 1 \\ i \end{pmatrix}$

The ratio of the major semi-axis divided by the minor semi-axis is the axial ratio (AR) of the polarization ellipse. For $AR = 1$, the plane wave is circularly polarized, while for $AR \rightarrow \infty$, it is linearly polarized.

If the polarization state of a plane wave does not change when it propagates through a medium, it is called an eigenpolarization of this medium. In an isotropic medium, all polarizations are eigenpolarizations. Two orthogonal polarizations (not necessarily eigenpolarizations) constitute a basis that can be used to express all other polarizations. Often used bases are the linear basis with x - and y -polarization and the circular basis with LCP and RCP. A circular basis is often used for the description of chiral media as they have circular eigenpolarizations (see section 2.3.4).

2.2.2. Jones Calculus

Using Jones calculus, the effect of materials and optical components on plane waves can be calculated and represented in a convenient way. A polarization state in the linear basis L with x - and y -polarization is displayed using a Jones vector \vec{J}_L :

$$\vec{J}_L = \begin{pmatrix} E_x \\ E_y \end{pmatrix} \quad (2.40)$$

with the complex electric field components defined in (2.35). Often, normalized Jones vectors are used. Table 2.2 gives an overview of some polarization states expressed by normalized Jones vectors.

The transmission of a plane wave by an optical system or a material slab can be described using a Jones matrix $M_{T,L}$. It connects the Jones vectors of the incident (i) and the transmitted (t) wave:

$$\vec{J}_{L,t} = \begin{pmatrix} E_{x,t} \\ E_{y,t} \end{pmatrix} = \begin{pmatrix} t_{xx} & t_{xy} \\ t_{yx} & t_{yy} \end{pmatrix} \begin{pmatrix} E_{x,i} \\ E_{y,i} \end{pmatrix} = M_{T,L} \vec{J}_{L,i}. \quad (2.41)$$

Table 2.3 Normalized Jones vectors in the circular basis for linear and circular polarization states.

linear polarization		circular polarization	
x-polarization	$\vec{J}_{C,x} = \frac{1}{\sqrt{2}} \begin{pmatrix} 1 \\ 1 \end{pmatrix}$	RCP	$\vec{J}_{C,RCP} = \begin{pmatrix} 0 \\ 1 \end{pmatrix}$
with angle α	$\vec{J}_{C,\alpha} = \frac{1}{\sqrt{2\cos(2\alpha)}} \begin{pmatrix} \cos(\alpha) \\ \sin(\alpha) \end{pmatrix}$	LCP	$\vec{J}_{C,LCP} = \begin{pmatrix} 1 \\ 0 \end{pmatrix}$

The diagonal elements t_{xx} and t_{yy} are the transmission coefficients and the off-diagonal elements t_{xy} and t_{yx} are the conversion coefficients. The conversion coefficients describe transformations between different polarization states. When the Jones matrix is expressed in a basis constructed by eigenvectors, the conversion coefficients are zero. Reflections are calculated analogously.

In chiral media it is helpful to use a circular basis. The change from the linear basis L to the circular basis C is done using a matrix M_{LC} :

$$\vec{J}_C = \begin{pmatrix} E_{LCP} \\ E_{RCP} \end{pmatrix} = \begin{pmatrix} 1 & i \\ 1 & -i \end{pmatrix} \begin{pmatrix} E_x \\ E_y \end{pmatrix} = M_{LC} \vec{J}_L. \quad (2.42)$$

Table 2.3 shows the Jones vectors which we have already seen in table 2.2, but for the circular basis. Using M_{LC} and its inverse M_{LC}^{-1} , the Jones matrix $M_{T,L}$ can be transferred from linear to circular basis, too:

$$M_{T,C} = \begin{pmatrix} t_{ll} & t_{lr} \\ t_{rl} & t_{rr} \end{pmatrix} = M_{LC} M_{T,L} M_{LC}^{-1}. \quad (2.43)$$

The indices l and r represent LCP and RCP, respectively.

2.2.3. Description of Asymmetric Transmission using Jones Calculus

Asymmetric Transmission can occur in metamaterials with asymmetric building blocks. We will discuss the optical properties of such materials in the next section. However, the basic idea of asymmetric transmission can be described without knowing the exact properties of such a material.

The transmission of a plane wave through a material slab can be described by the Jones matrix $M_{T,L}$ (2.41) in the linear basis L. When the same wave travels through the slab in

the opposite direction, we can use a matrix

$$M_{T,L,b} = \begin{pmatrix} t_{xx} & -t_{yx} \\ -t_{xy} & t_{yy} \end{pmatrix} \quad (2.44)$$

for the description of the transmission. The transmission coefficients of this matrix, t_{xx} and t_{yy} , stay the same as for forward propagation due to reciprocity [52]. However, the off-diagonal elements t_{yx} and t_{xy} have switched their positions and are now negative [53]. This can lead to a difference, or asymmetry, in the transmittance for forward and backward propagation of a plane wave. Please note that if the polarization vectors constituting the base are eigenvectors, asymmetric transmission is not possible because the off-diagonal elements are zero. Asymmetric transmission of a linearly polarized wave was measured in [53].

The same applies for the propagation of a plane wave expressed in the circular basis. The Jones matrix for the transmission can then be written as

$$M_{T,C,b} = \begin{pmatrix} t_{ll} & t_{rl} \\ t_{lr} & t_{rr} \end{pmatrix}. \quad (2.45)$$

Again, the off-diagonal elements switch places, however without changing their signs [53]. The diagonal elements remain unaltered. An asymmetric transmission of circularly polarized waves was reported in [54].

2.3. Chiral and Bianisotropic Metamaterials

Helical metamaterials are chiral. In this section, we want to explain what chirality means and why helices have chiral properties. Chirality is closely linked to bianisotropy. Or, more accurately, a subset of bianisotropic media are chiral media. Hence, helical metamaterials are also bianisotropic. In the case of materials consisting of oriented helix arrays, uniaxial bianisotropy can result. Therefore, an overview of different classes of bianisotropic media and special cases in which they can be treated as chiral media is given. We will describe plane wave solutions and optical phenomena which can occur in chiral metamaterials like circular dichroism, optical activity, and a negative refractive index. The next section examines the optical properties of our metamaterial building blocks, namely helices. In the end of this section, we give a short overview of chiral optical metamaterial structures which have been realized in the past years in order to provide a comparison to our structures (presented in chapter 6).

2.3.1. Geometrical Definition of Chirality

Chirality is a property describing a certain asymmetry in geometrical structures. It was defined by Lord Kelvin in 1884 [1]: *“I call any geometrical figure, or group of points, chiral, and say that it has chirality if its image in a plane mirror, ideally realized, cannot be brought to coincide with itself.”*

A very illustrative example for chirality are human hands. Actually, the Greek word for

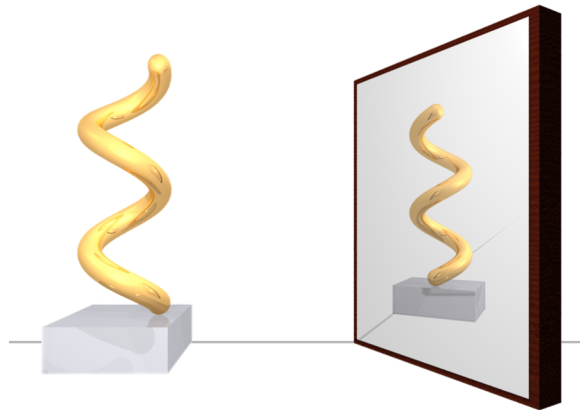


Figure 2.10 3D chiral object: a left-handed helix and its mirror image [25].

hand is *cheri* ($\chi\acute{\epsilon}\rho\iota$) [55]. The mirror image of your right hand is a left hand. You can not overlap them with palms down because the palm is different to the back of a hand. A property which can be assigned to 3D chiral objects is handedness: When you rotate the fingers of your right hand around the thumb and move the hand in the direction the thumb points, it will spiral up *right-handedly*. Doing the same with the left hand, we see that it spirals up, too, but with a different sense of rotation, called *left-handed*.

Another prominent example for chiral objects are helices. Figure 2.10 shows a left-handed helix and its mirror image which is a right-handed helix. No matter how they are rotated or translated, they can not be brought to coincide. This also implies the fact that the handedness of a helix (and a chiral object in general) does not depend on the direction from which we look at it.

Chirality is present everywhere around us and can take very different forms: hands and helices, screws and screw conveyors, snail shells and chiral molecules like glucose or DNA, the combination of spin and momentum vectors of elementary particles, and circular polarization states of light - just to name some examples.

Two-dimensional Chirality

Chiral objects can also exist in two dimensions (2D). For example, we see a spiral and its mirror image in figure 2.11. Through translations and rotations within the plane, they can not coincide and hence are chiral. However, if we move them into 3D space, the planar chiral structures lose their chirality. Then we can simply flip the mirror image in figure 2.11 and overlay it with the original.

When one fabricates a planar chiral structure, it usually lies on a substrate. Then, chirality is obviously restored because of the asymmetry introduced by the substrate. However, the expected effects are much weaker than those from 3D chiral metamaterials (see section 2.3.7).

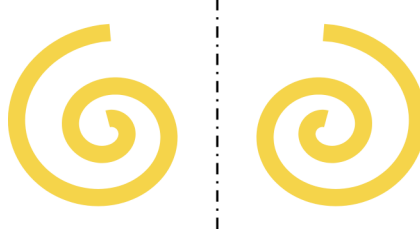


Figure 2.11 2D chiral object: a spiral (left) and its mirror image (right). The mirror line is indicated by the dash-and-dot line.

2.3.2. Bianisotropy and Chirality

The properties of an effective optical medium are described by the constitutive relations, as we have seen for *isotropic* linear materials in section 2.1.2. In the general case of *bianisotropic* linear materials, they can be expressed in the form [31]

$$\vec{D}(\vec{r}, \omega) = \varepsilon_0 \vec{\varepsilon} \vec{E}(\vec{r}, \omega) + \vec{\xi} \vec{H}(\vec{r}, \omega), \quad (2.46)$$

$$\vec{B}(\vec{r}, \omega) = \vec{\zeta} \vec{E}(\vec{r}, \omega) + \mu_0 \vec{\mu} \vec{H}(\vec{r}, \omega). \quad (2.47)$$

In contrast to isotropic materials, here all material parameters are complex tensors of the order two. We call $\vec{\varepsilon}$ the electric permittivity parameter, $\vec{\mu}$ the magnetic permeability parameter and $\vec{\xi}$ and $\vec{\zeta}$ the magnetoelectric cross-coupling parameters. The magnetoelectric cross-coupling parameters describe the *bianisotropy* of the medium, *i.e.* the fact, that the electric (magnetic) field does induce a magnetization (polarization) in the medium. In addition, in a bianisotropic medium, excited magnetizations and polarizations are, in general, not parallel to exciting magnetic and electric fields.

Depending on their parameters, bianisotropic materials can be divided into different classes. A very detailed classification has been proposed in [56]. Here, we show the basic division into four different classes:

- **Isotropic media:** $\varepsilon, \mu \in \mathbb{C}$ and $\xi, \zeta = 0$.
The medium has equal properties in all directions. Electric (magnetic) fields excite a polarization (magnetization) parallel to them. These media have been discussed in section 2.1.
- **Biisotropic media:** $\varepsilon, \mu, \xi, \zeta \in \mathbb{C}$.
The external electric field can induce a parallel polarization and a parallel magnetization. Analogous, the external magnetic field can induce a parallel polarization and a parallel magnetization.
- **Anisotropic media:** $\vec{\varepsilon}, \vec{\mu}$ are tensors and $\xi, \zeta = 0$.
An excited polarization (magnetization) is not necessarily parallel to the exciting electric (magnetic) field. Hence, the medium has different properties in varying directions.

- Bianisotropic media: $\vec{\epsilon}$, $\vec{\mu}$, $\vec{\zeta}$, $\vec{\xi}$ are tensors.

This is the most general case where the external fields can excite both a polarization and a magnetization that is not necessarily parallel to them.

The magnetoelectric cross-coupling parameters $\vec{\xi}$ and $\vec{\zeta}$ can be expressed in terms of the chirality tensor $\vec{\kappa}$ and the nonreciprocity (or Tellegen) tensor $\vec{\chi}$ [56]:

$$\vec{\xi} = (\vec{\chi}^T - i \vec{\kappa}^T) \frac{1}{c_0}, \quad (2.48)$$

$$\vec{\zeta} = (\vec{\chi} + i \vec{\kappa}) \frac{1}{c_0}, \quad (2.49)$$

where T denotes the transpose of a tensor. There are some differences between $\vec{\kappa}$ and $\vec{\chi}$. Let us imagine that both were real and insert (2.48) and (2.49) in (2.46) and (2.47). Then, we see that through the chirality tensor, there is always a 90° phase-shift between exciting and excited fields. For the nonreciprocity tensor, such a phase-shift is not present. Also, there is an asymmetry in the sign of $\vec{\kappa}$ while there is none for $\vec{\chi}$.

One example for properties of nonreciprocal media is the magnetoelectric effect. It was first reported in [57]. There, an internal static magnetic field (due to ferro- or antiferromagnetism) was responsible for the nonreciprocal effect. Another example is the Faraday effect where an external magnetic field is present and causes the nonreciprocal behavior. For a detailed discussion of (non)reciprocity, see *e.g.* [32, 52].

Within this thesis, only reciprocal materials are considered. This leads to the following conditions [32]:

$$\vec{\epsilon} = \vec{\epsilon}^T, \quad \vec{\mu} = \vec{\mu}^T, \quad \vec{\xi} = -\vec{\zeta}^T. \quad (2.50)$$

This means that the nonreciprocity tensor $\vec{\chi} = 0$, as one would expect for a reciprocal medium. For reciprocal bianisotropic media, (2.46) and (2.47) have the form

$$\vec{D}(\vec{r}, \omega) = \epsilon_0 \vec{\epsilon} \vec{E}(\vec{r}, \omega) - i \frac{1}{c_0} \vec{\kappa}^T \vec{H}(\vec{r}, \omega), \quad (2.51)$$

$$\vec{B}(\vec{r}, \omega) = i \frac{1}{c_0} \vec{\kappa} \vec{E}(\vec{r}, \omega) + \mu_0 \vec{\mu} \vec{H}(\vec{r}, \omega). \quad (2.52)$$

We want to discuss the effect of the chirality tensor $\vec{\kappa}$ on the material properties. Written as a 3×3 matrix, it has the form

$$\vec{\kappa} = \begin{pmatrix} \kappa_{xx} & \kappa_{xy} & \kappa_{xz} \\ \kappa_{yx} & \kappa_{yy} & \kappa_{yz} \\ \kappa_{zx} & \kappa_{zy} & \kappa_{zz} \end{pmatrix}. \quad (2.53)$$

In connection with (2.51) and (2.52), we see that the diagonal elements describe the excitation of electric (magnetic) dipoles parallel to the exciting magnetic (electric) field,

which is a basic property of chiral media. Thus, a material is called chiral if the diagonal elements of $\vec{\kappa}$ are not zero. If all off-diagonal elements are zero at the same time, the material is said to show “pure” chirality. This is because the off-diagonal elements of $\vec{\kappa}$ lead to excited electric (magnetic) dipoles which are perpendicular to an exciting magnetic (electric) field. A material where all diagonal elements are zero is called purely bianisotropic.

Reciprocal bianisotropic media can be realized by using many different building blocks. These building blocks obey some common rules [58].

- **Inversion symmetry:** We mentioned in section 2.3.1, that a chiral object can not be brought into congruence with its mirror image. This is identical to the fact that no inversion symmetry is present for chiral objects. This is even the case for bianisotropic media in general. For spatial inversion, obviously spatial coordinates have to be inverted: $\vec{r} \rightarrow -\vec{r}$. This also leads to a replacement of \vec{k} , \vec{E} and \vec{B} (see, e.g. [29]): $\vec{k} \rightarrow -\vec{k}$, $\vec{E} \rightarrow -\vec{E}$ and $\vec{B} \rightarrow \vec{B}$. \vec{B} keeps its sign because it is a pseudo vector. Or, more intuitively, by this means the orthogonal system $(\vec{k} - \vec{E} - \vec{B})$ (see (2.17)) stays right-handed. Looking at (2.51) and (2.52), we see that when inserting the given replacements, the equations can only be fulfilled if $\vec{\kappa} = 0$.
- **Mirror plane parallel to propagation direction:** For a mirror plane in the yz -plane and propagation in z -direction, the electric field in x -direction has to be replaced as $E_x \rightarrow -E_x$. E_y is parallel to the mirror plane and hence does not change sign. The system $(\vec{k} - \vec{E} - \vec{B})$ stays right handed, if B_x keeps its sign and $B_y \rightarrow -B_y$. Then, equation (2.52) is only fulfilled if $\kappa_{xx} = \kappa_{yy} = 0$, while there is no restriction on κ_{xy} and κ_{yx} . The same results if the mirror plane lies in the xz -plane. Imagining propagation along y - and x -direction with parallel mirror planes, it becomes clear that all diagonal elements of $\vec{\kappa}$ have to be zero. This means that a medium with mirror symmetry parallel to the propagation direction can be bianisotropic but not chiral.
- **Mirror plane perpendicular to propagation direction:** In this case $\vec{k} \rightarrow -\vec{k}$ and \vec{E} keeps sign as it is parallel to the mirror plane. In order to keep $(\vec{k} - \vec{E} - \vec{B})$ right-handed, $\vec{B} \rightarrow -\vec{B}$. Like for inversion symmetry, this can only be fulfilled by (2.52) if $\vec{\kappa} = 0$ and hence no bianisotropy is possible for a system with mirror symmetry perpendicular to the propagation direction. We will shortly come back to this point when considering planar chiral structures in section 2.3.7.

Biisotropy and “Pure” Chirality

Biisotropic media possess no preferred direction just like isotropic media. The difference is that in a biisotropic medium, both electric and magnetic fields can couple to electric as well as magnetic dipoles in the medium. As noted above, in biisotropic media the parameter tensors all reduce to complex scalars. When a medium is reciprocal, it is “purely” chiral.

With the chirality parameter κ , the constitutive relations can be written as

$$\vec{D}(\vec{r}, \omega) = \epsilon_0 \epsilon \vec{E}(\vec{r}, \omega) - i \frac{1}{c_0} \kappa \vec{H}(\vec{r}, \omega), \quad (2.54)$$

$$\vec{B}(\vec{r}, \omega) = i \frac{1}{c_0} \kappa \vec{E}(\vec{r}, \omega) + \mu_0 \mu \vec{H}(\vec{r}, \omega). \quad (2.55)$$

Such a material could be realized by completely randomly distributing metallic helices [31].

As introduced in section 2.3.1, taking the mirror image of a chiral building block leads to a change in the handedness of the structure. In terms of κ , this is expressed by the fact that taking the mirror image of a biisotropic chiral medium corresponds to changing the sign of the chirality parameter: $\kappa \rightarrow -\kappa$. Spatial inversion has the same effect as taking the mirror image and leads to a change of the sign of κ , too. This is a nice illustration of the symmetry conditions discussed above because fulfilling these conditions demands $\kappa = -\kappa \rightarrow \kappa = 0$ and hence the material would not be chiral.

A solution of the wave equations of bianisotropic media is only possible in some special cases. Solutions for bianisotropic but non-chiral media have been proposed in [59–62]. For biisotropic chiral media, solutions can easily be derived as we will show in section 2.3.4. Solutions have also been found for uniaxial bianisotropic media [63], but are complicated in general. However, their properties are similar to biisotropic chiral media in some special cases that we will describe in the following subsection.

2.3.3. Uniaxial Bianisotropy

Uniaxial bianisotropic media possess one preferred spatial direction. A detailed discussion can be found in [63]. Such a medium can be realized by using metal helices made of thin metal wires and arranging them either parallel or perpendicular to the z -axis of a coordinate system but otherwise randomly, as depicted in figure 2.12. There, \hat{k} is the unit vector in propagation direction and θ is the angle between \hat{k} and the z -direction.

In an uniaxial reciprocal bianisotropic medium, the material parameters become much simpler than for the general form discussed in the previous section and can be expressed using \hat{z} and a unit dyadic transverse to it, $\vec{I}_t = \hat{x} \cdot \hat{x}^T + \hat{y} \cdot \hat{y}^T$, where t denotes components perpendicular to the z -axis [63]:

$$\vec{\epsilon} = \epsilon_z \hat{z} \cdot \hat{z}^T + \epsilon_t \vec{I}_t, \quad (2.56)$$

$$\vec{\mu} = \mu_z \hat{z} \cdot \hat{z}^T + \mu_t \vec{I}_t, \quad (2.57)$$

$$\vec{\kappa} = \kappa_z \hat{z} \cdot \hat{z}^T + \kappa_t \vec{I}_t. \quad (2.58)$$

This means that there are only six parameters left. Also, all material parameter tensors have entries only along their diagonals. Expressions for the wave vectors of eigenwaves and eigenpolarizations can be derived in this case and are given in [63]. There are two eigenpolarizations present which will be denoted as \vec{k}_\pm

The reflection and transmission of plane waves through slabs of reciprocal uniaxial

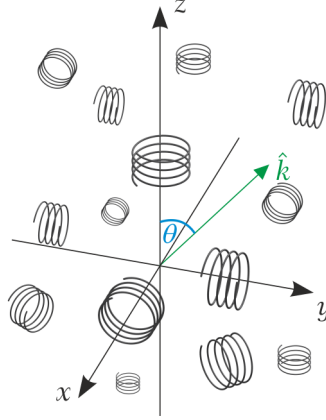


Figure 2.12 Possible realization of a uniaxial bianisotropic medium with metal helices oriented either parallel or perpendicular to the z -direction. \hat{k} points in the propagation direction which includes an angle θ with \hat{z} (following [63]).

bianisotropic media is discussed in [64]. In order to get an intuition of the effects of the six parameters despite the rather complicated expressions of the wave vectors and eigenpolarizations, we will consider three special cases [63].

Axial Propagation

Propagation along the z -direction is called axial propagation. In this case, the axial symmetry demands that the eigenwaves are polarized transverse to the z -direction, *i.e.* they are transverse electromagnetic waves. Because they are perpendicular to the z -axis, the fields are only affected by the transverse material parameters denoted by t . The two wave vectors then point along \hat{z} and have the absolute value

$$k_{\pm} = \omega(\sqrt{\varepsilon_t \mu_t} \pm \kappa_t \frac{1}{c_0}). \quad (2.59)$$

This situation corresponds to two plane eigenwaves in a biisotropic medium [63]. They are circularly polarized with k_+ corresponding to RPC and k_- corresponding to LCP. For angles θ deviating from axial propagation, the eigenwaves become elliptically polarized as is shown for some material parameter values in [63].

Axial Bianisotropy

In the case of axial bianisotropy, the medium has chiral properties only along the z -direction. This is reflected by the fact that $\kappa_t = 0$. Such a medium can be realized by randomly distributing helices which are all oriented parallel to the z -direction. In this case, the z -axis is the optical axis which means that for axial propagation, the two wave eigenvectors k_{\pm} in (2.59) are degenerate. For axially bianisotropic materials, plane wave solutions with wave vectors and eigenpolarizations have been derived [31, 65–68]. These media have been proposed for application as polarization transformers [31, 66, 69]. Such a polarization transformer would allow to change both the amplitude values and

the phase between the polarization components of a propagating wave. Basically, these properties arise from different phase velocities of the two, in general elliptically polarized, eigenwaves. Indeed, a wave plate has been demonstrated [70] using square arrays of long helices for centimeter waves.

Transverse Bianisotropy

For transverse bianisotropy, chirality is present only transverse to the z -direction and $\kappa_z = 0$. These media can be realized through randomly distributed helices oriented perpendicular to the z -axis. Transverse bianisotropic media have been discussed in [71]. They can also be used as polarization transformers. In contrast to axial bianisotropic materials however, they do not possess an optical axis.

2.3.4. Wave Propagation in Chiral Media

In the following, we assume a biisotropic, purely chiral medium described by the chirality parameter κ . However, the derived equations also apply to uniaxial bianisotropic media for the special cases discussed above.

In order to obtain solutions for plane waves in chiral media, it is helpful to express the electric field in terms of two electric fields that we call wavefields. Analogously, the magnetic field is expressed in terms of two magnetic wavefields. This has been done in [31] for biisotropic materials. We follow this scheme, however exclusively for chiral media.

It is assumed that for a chiral medium, the fields $\vec{E}(\vec{r}, \omega)$ and $\vec{H}(\vec{r}, \omega)$ can be written in the form

$$\vec{E}(\vec{r}, \omega) = \vec{E}_+(\vec{r}, \omega) + \vec{E}_-(\vec{r}, \omega), \quad \vec{H}(\vec{r}, \omega) = \vec{H}_+(\vec{r}, \omega) + \vec{H}_-(\vec{r}, \omega), \quad (2.60)$$

where the wavefields $\vec{E}_+(\vec{r}, \omega)$, $\vec{H}_+(\vec{r}, \omega)$, $\vec{E}_-(\vec{r}, \omega)$, and $\vec{H}_-(\vec{r}, \omega)$ behave as if being in an isotropic medium. It is also defined that components denoted with “+” do not couple to components denoted with “-”. Hence, they can be handled independently. As the equations for both wavefields have the same form in chiral media, we will denote them by using the index \pm . The assumption that the medium is isotropic for the wavefields leads to the replacements

$$\vec{D}_\pm(\vec{r}, \omega) = \varepsilon_0 \varepsilon \vec{E}_\pm(\vec{r}, \omega) - i \frac{1}{c_0} \kappa \vec{H}_\pm(\vec{r}, \omega) = \varepsilon_0 \varepsilon_\pm \vec{E}_\pm(\vec{r}, \omega), \quad (2.61)$$

$$\vec{B}_\pm(\vec{r}, \omega) = i \frac{1}{c_0} \kappa \vec{E}_\pm(\vec{r}, \omega) + \mu_0 \mu \vec{H}_\pm(\vec{r}, \omega) = \mu_0 \mu_\pm \vec{H}_\pm(\vec{r}, \omega). \quad (2.62)$$

When solving the right parts of (2.61) and (2.62) for $\vec{E}_\pm(\vec{r}, \omega)$, we see that the wavefield must satisfy the conditions

$$\vec{E}_\pm(\vec{r}, \omega) = i \frac{\kappa}{c_0 \varepsilon_0 (\varepsilon - \varepsilon_\pm)} \vec{H}_\pm(\vec{r}, \omega), \quad (2.63)$$

$$\vec{E}_\pm(\vec{r}, \omega) = i \frac{c_0}{\kappa} \mu_0 (\mu - \mu_\pm) \vec{H}_\pm(\vec{r}, \omega). \quad (2.64)$$

The Maxwell equations for the wavefield components have the same form as introduced in section 2.1.2, (2.7) – (2.10). After replacing $\vec{D}_\pm(\vec{r}, \omega)$ and $\vec{B}_\pm(\vec{r}, \omega)$ by $\vec{E}_\pm(\vec{r}, \omega)$ and $\vec{H}_\pm(\vec{r}, \omega)$, we get

$$\nabla \times \vec{E}_\pm(\vec{r}, \omega) = i\omega\mu_0\mu_\pm\vec{H}_\pm(\vec{r}, \omega), \quad (2.65)$$

$$\nabla \cdot \vec{E}_\pm(\vec{r}, \omega) = 0, \quad (2.66)$$

$$\nabla \times \vec{H}_\pm(\vec{r}, \omega) = -i\omega\varepsilon_0\varepsilon_\pm\vec{E}_\pm(\vec{r}, \omega), \quad (2.67)$$

$$\nabla \cdot \vec{H}_\pm(\vec{r}, \omega) = 0. \quad (2.68)$$

Using the conditions (2.63) and (2.64) and the Maxwell equations (2.65) and (2.67), the relations between the material parameters for the decomposed wavefields and the original material parameters can be found (see appendix A.1). Until now, the equations for both wavefield components were equal. However, the obtained relation leads to a quadratic equation and the two solutions lead to different behavior for the wave fields:

$$\mu_\pm = \mu\left(1 \pm \frac{1}{n}\kappa\right), \quad \varepsilon_\pm = \varepsilon\left(1 \pm \frac{1}{n}\kappa\right). \quad (2.69)$$

The relations also show, that the impedance does not depend on the chirality parameter and hence is equal for both wavefields (appendix A.1, (A.9)):

$$Z_\pm = \sqrt{\frac{\mu_\pm}{\varepsilon_\pm}} = \sqrt{\frac{\mu}{\varepsilon}} = Z. \quad (2.70)$$

For the propagation of a plane wave with

$$\vec{E}_\pm(\vec{r}, t) = \vec{E}_{0,\pm}e^{i(\vec{k}_\pm\vec{r}-\omega t)}, \quad (2.71)$$

$$\vec{H}_\pm(\vec{r}, t) = \vec{H}_{0,\pm}e^{i(\vec{k}_\pm\vec{r}-\omega t)}, \quad (2.72)$$

we get the same solutions as for an isotropic medium:

$$\vec{k}_\pm \times \vec{E}_\pm(\vec{r}, t) = \omega\mu_0\mu\left(1 \pm \frac{1}{n}\kappa\right)\vec{H}_\pm(\vec{r}, t), \quad (2.73)$$

$$k_\pm = k_0n_\pm, \quad (2.74)$$

where the refractive index has the form

$$n_\pm = \sqrt{\varepsilon_\pm\mu_\pm} = n \pm \kappa. \quad (2.75)$$

From equation (2.73), we see that the electric field, the magnetic field, and the wave vector form a right-handed system. Thus, we have two independent plane waves. The polarizations of these plane waves are eigenpolarizations in the chiral medium because it acts like an isotropic medium on them as defined above. To determine the polarization,

we replace $\vec{H}_\pm(\vec{r})$ in (2.73) using the condition (2.64) and get

$$\vec{k}_\pm \times \vec{E}_\pm(\vec{r}) = \pm ik_\pm \vec{E}_\pm(\vec{r}), \quad (2.76)$$

$$(2.77)$$

which implies that the dot product of $\vec{E}_\pm(\vec{r})$ with itself is zero:

$$\vec{E}_\pm(\vec{r}) \cdot \vec{E}_\pm(\vec{r}) = 0. \quad (2.78)$$

This condition is satisfied by a circularly polarized wave. This can be seen, for example, by inserting (2.35) in (2.78) and solving for ϕ : $E_{0,x}^2 = E_{0,y}^2$ and $\phi = \pm \frac{\pi}{2}$ will result. By inserting the Jones vectors for LCP and RCP in (2.76), it is easy to show that \vec{E}_+ corresponds to RCP and \vec{E}_- to LCP. Thus, LCP and RCP are eigenpolarizations of a chiral medium.

2.3.5. Optical Phenomena in Chiral Media

The dependence of the refractive index on the chirality parameter leads to interesting phenomena. Circular birefringence and circular dichroism are well known from natural chiral media like quartz or solutions of molecules with a certain handedness. In chiral metamaterials, these phenomena can be strongly enhanced in comparison to natural media. Using metamaterials, a negative refractive index can be achieved as we mentioned in section 2.1.5. Although chirality is not necessary to achieve a negative refractive index, it offers a different approach to it that we will discuss in the last part of this section.

Circular Birefringence and Circular Dichroism

A chiral material can be described with isotropic material parameters for each of the two circular polarizations, however, these parameters are in general not equal. As we see in (2.75), the two circular polarizations have different refractive indices. We insert the wave vector (2.74) into the expression for the plane wave (2.71):

$$\vec{E}_\pm(\vec{r}, t) = \vec{E}_{0,\pm} e^{i(k_0(n \pm \kappa)\hat{k}\vec{r} - \omega t)}. \quad (2.79)$$

In general, $n \pm \kappa$ is a complex number. Through its real part, the two circular polarizations have different phase velocities in the medium. This is called circular birefringence. The imaginary part of $n \pm \kappa$ leads to different attenuation of the circular polarizations called circular dichroism. Figure 2.13 (a) depicts two plane waves propagating through a chiral material slab at a time t_0 . The left wave has RCP and the right wave has LCP. Their polarization states are not changed as they are eigenpolarizations. However, the phase velocity of RCP is smaller in the medium leading to a smaller wavelength while the phase velocity of LCP merely changes. The amplitude of LCP is strongly attenuated while the amplitude of RCP mainly stays the same. The real and the imaginary parts of the material parameters are connected through the Kramers-Kronig relations [29]. Thus, a medium with circular birefringence will also show circular dichroism and *vice versa*.

We also want to give a brief explanation of linear birefringence and linear dichroism. They

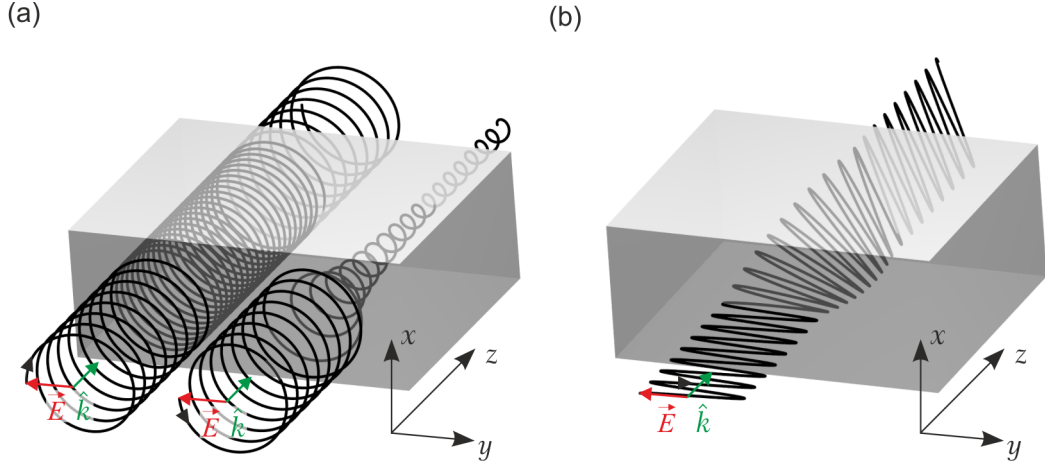


Figure 2.13 Optical phenomena in chiral media. (a) Propagation of light with RCP (left side) and LCP (right side) through a medium with circular birefringence and circular dichroism. (b) Propagation of a plane wave with x -polarization through a medium with circular birefringence. The polarization plane is rotated due to optical activity. In both figure parts, the black lines show the ways described by the tips of the electric field vectors \vec{E} in space at a time t_0 . For one position, the electric field vector (red) is shown together with a vector \hat{k} (green) which points in the direction of the propagation.

are the equivalents to circular birefringence and circular dichroism, however for a linear polarization. They can occur in anisotropic and bianisotropic materials like crystals [27]. If such a material is uniaxial, it has a preferred spatial direction and an optical axis (also called ordinary axis) in this direction. Imagine two linearly polarized plane waves which travel through this material. If one is polarized parallel to the ordinary axis and the other is polarized perpendicular to it, they have different refractive indices and hence different phase velocities. This effect is widely used, for example in wave plates. We will come back to linear birefringence when explaining the used optical characterization setup in section 5.1.

Optical Activity

In chiral media, the polarization plane of a linearly polarized plane wave is rotated, which is called optical activity. Recalling table 2.2, we see that an x -polarization can be obtained by the superposition of RCP and LCP. When an x -polarized wave enters a chiral medium, we can imagine it decomposed into RCP and LCP. In the medium, the circular polarizations have different refractive indices and hence different phase velocities. Let us assume that $n_- > n_+$. After a distance d , the two circularly polarized waves have a phase difference of $\Delta\phi = (k_0 n_- d) - (k_0 n_+ d)$. The superposition of these waves leads to a linear polarization. When looking against the propagation direction, the polarization plane is rotated counter-clockwise by the angle $\alpha = \frac{1}{2}\Delta\phi$. We immediately see that when $n_- < n_+$, α will be negative and the rotation will be clockwise. Intuitively, the polarization rotation can also be understood by looking at (2.55).

There we see that the electric field excites a parallel magnetization $i\frac{1}{c_0}\kappa\vec{E}(\vec{r},\omega)$. On the other hand, the electric field emitted by a magnetic dipole is perpendicular to it. The superposition of excited and exciting electric fields leads to a rotation of the polarization plane. Depending on κ , the magnetization is parallel or antiparallel to the exciting field and the polarization plane will be rotated clockwise or counter-clockwise.

Negative Refractive Index

One possibility to achieve a negative refractive index is to overlay a magnetic and an electric resonance in such a way, that permittivity and permeability are negative at the same time. This does not require chirality and has been realized in [10, 11] for optical frequencies.

A different route to a negative refractive index has been proposed in [16]: a negative refractive index can be realized by electric dipole resonators embedded in an chiral material. In (2.75), we directly see that the refractive index n_{\pm} can be negative if the value of the chirality parameter κ is sufficiently big and is subtracted from n . We also see, that the negative value can only be achieved for one circular polarization, while it will be positive for the other.

Chiral metamaterials can combine an electric resonance with strong chirality to obtain a negative index of refraction. This has been realized in [72–76], however for frequencies of 1 THz or below. A negative refractive index in the optical regime has not been realized by means of chirality to our knowledge.

2.3.6. Helices as Metamaterial Building Blocks

We already introduced the helix as a chiral object. Artificially made helices have been used for the manipulation and investigation of electromagnetic waves for a long time: In 1920, K. F. Lindman conducted microwave experiments using randomly oriented and distributed metal helices with a cross-section of 1 cm [4, 77]. In 1947, the helical beam antenna was presented by J. D. Kraus [78].

How do helices interact with electromagnetic waves? When a voltage is applied to the ends of a macroscopic metal helix, the resulting current along the helix line leads to a magnetic field parallel to the helix axis.

Now, imagine the electric field of an electromagnetic wave which is polarized parallel to the helix axis of a microscopically small helix. It excites a current in the helix. The current gives rise to a magnetic dipole \vec{m} which will oscillate accordingly to the oscillation of the electric field. Figure 2.14 (a) depicts this for a right-handed helix. The electric field \vec{E} leads to an electric dipole moment \vec{p} and a magnetic dipole moment \vec{m} parallel to it. For a left-handed helix, the magnetic dipole moment is antiparallel to the electric field (figure 2.14 (b)) [27].

When the composition of such building blocks can be viewed as a homogeneous material, its magnetization will be parallel to the exciting electric field. Thus, the medium will exhibit magnetoelectric cross-coupling and chiral optical properties.

In section 2.3.2, we stated that the chirality parameter κ changes sign when taking the mirror image of a chiral medium. We can understand this intuitively for media

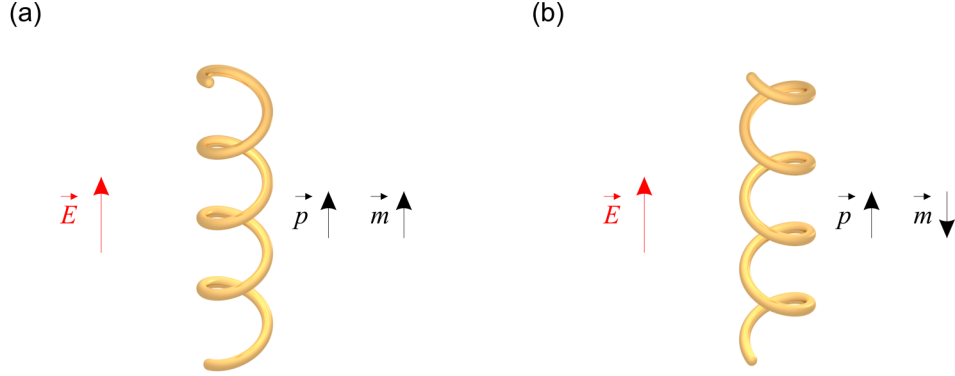


Figure 2.14 Electric (\vec{p}) and magnetic (\vec{m}) dipole moments of a metal helix induced by an electromagnetic plane wave with an electric field \vec{E} oriented parallel to the helix axis of a (a) right-handed helix, and (b) left-handed helix.

composed of helices as the mirror image of a left-handed helix is a right-handed helix. As the magnetic dipoles of single helices are parallel or antiparallel to the exciting field depending on the handedness, the magnetization of a material composed of helices will be, too. A change in the sign of the magnetization directly changes the sign of κ . In terms of plasmon resonances, the described excitation corresponds to a fundamental resonance. The current flows along the entire helix without current nodes. Higher resonant modes will be discussed in section 6.1.

For the application of helices as metamaterial building blocks, analytical expressions for ε , μ , and κ would be helpful. Such expressions have been derived for the fundamental resonances of so called canonical helices [31, 79, 80]. The canonical helix is a simplified helix model. It consists of a loop and two wires. They are attached perpendicular to the loop plane at the ends of the loop and point in opposite directions which makes the object chiral (see figure 2.15 (a)). When the wire is thin, the inductance of the loop and the capacitance of the wires can be used to obtain effective parameters [31].

In [81], an analytical model for thin helices has been proposed. There, a solution of the equation of electron motion along the helix line is given. Provided that the resonance frequency is known, the material parameters for an isotropic helix distribution can be calculated.

In our case however, the wire is thick due to fabrication and higher modes play an important role. Hence, these simple models can not be applied.

For our work, a comparison to helical antennas in the so called endfire geometry [82] is very instructive because many properties of such antennas can be transferred to the properties of helical metamaterials [83]. Figure 2.15 (b) shows a helix with helix radius R , pitch height p , wire thickness $2r$, pitch angle β , and $N = 4$ pitches. The pitch angle is given by $\tan \beta = \frac{p}{2\pi R}$. Helical antennas in the endfire geometry emit light which is nearly circularly polarized and strongly directed along the helix axis [82]. This functionality is present at a certain wavelength λ if the circumference of the helix fulfills $2\pi R \approx \lambda$. The

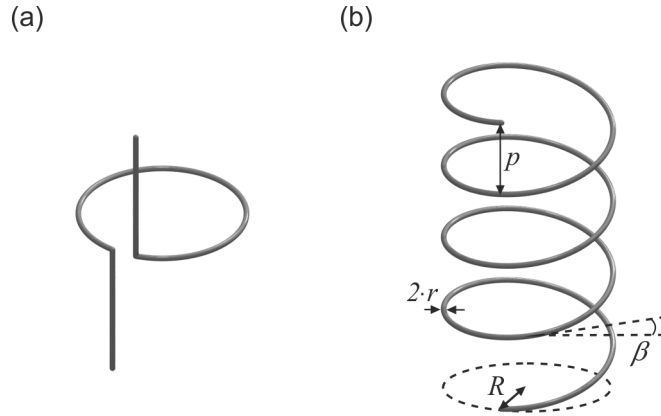


Figure 2.15 Helical structures. (a) Canonical helix, and (b) metal helix with a thin wire and $N = 4$ pitches.

directionality of the emission is increased with growing number of pitches. The axial ratio of the polarization ellipse is given by $AR = (2N + 1)/(2N)$ [82]. Although a circular polarization can only be realized for infinitely long helices, it is approached quite good even for helices with only two or three pitches. The functionality also depends on the pitch angle and is best for $\beta = 12 - 14^\circ$, corresponding to $p \approx 1.45 R$. Another important property of helical antennas is their broad band of functional wavelengths. According to [82], a single helical antenna with a thin wire and at least $N = 3$ helix pitches has a free-space operation bandwidth of

$$\lambda \in 2\pi R \cdot \left[\frac{3}{4}, \frac{4}{3} \right]. \quad (2.80)$$

The ratio of maximum to minimum wavelengths $\frac{\lambda_{\max}}{\lambda_{\min}} = \frac{16}{9} \approx 1.8$. This is almost one octave, which is quite a broad operation band.

In section 6.1, we will see that many properties of helical antennas can be found in helical metamaterials, too.

2.3.7. Realizations of Chiral Optical Metamaterials

We pointed out some phenomena of chiral materials. In particular, the presence of chirality in chemistry, applications of circular polarization in optical technologies and the chiral route to a negative refractive index motivated research on chiral metamaterials. In the following, we give a short overview of chiral *optical* metamaterial structures which have been realized. Although there has also been a lot of work done on chiral metamaterials in the microwave and centimeter wavelength region [72–76, 79, 84, 85], our focus is on optical wavelengths. A summary of existing methods for the fabrication of 3D optical metamaterials will be given in section 4.1.

As we have mentioned in section 2.3.1, 2D chiral structures can exhibit chiral properties if they are located on a substrate, because then, mirror symmetry in propagation direction is broken [17–19]. In [18], optical activity of a planar chiral metamaterial was reported.

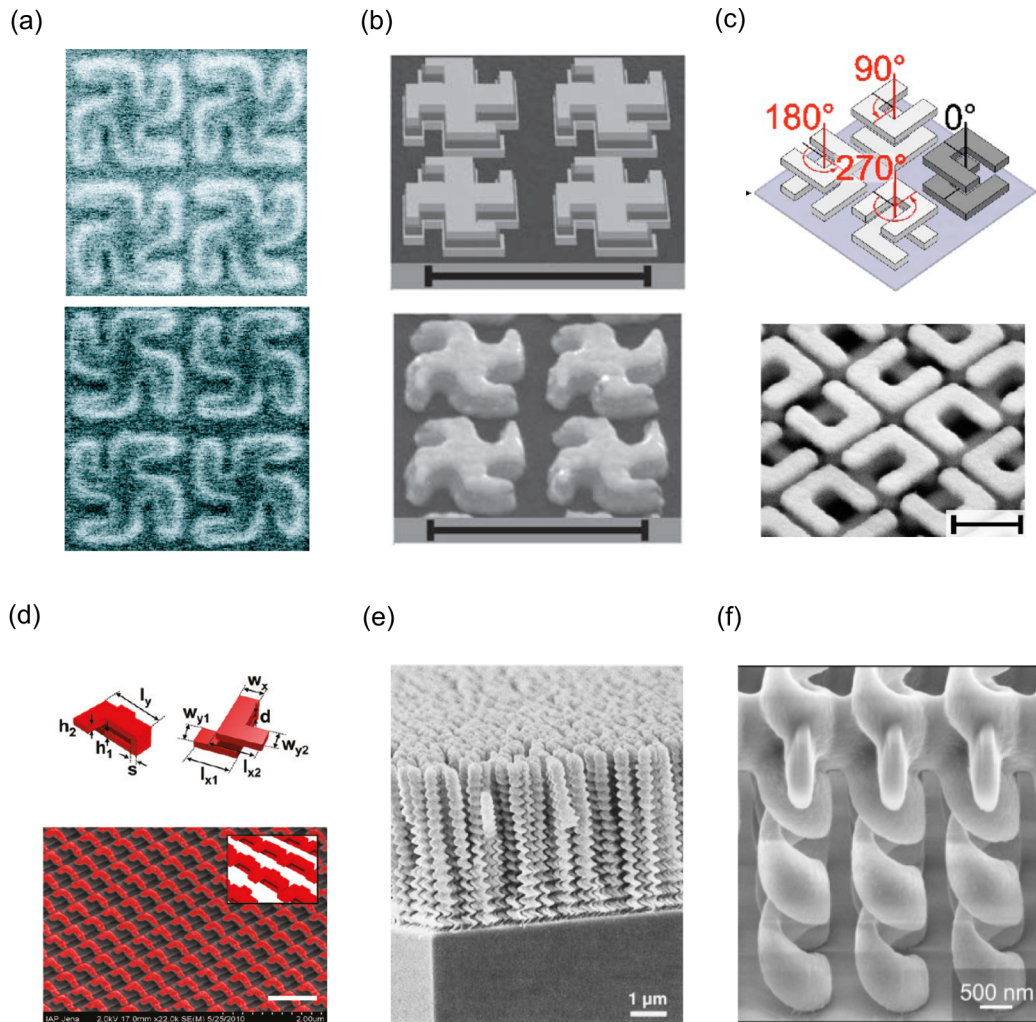


Figure 2.16 Realizations of chiral photonic structures. (a) Planar chiral structures with different sense of rotation [18]. The lateral period is 500 nm. (b) Designed (top) and fabricated (bottom) double-layer planar chiral metamaterial [19]. The scale bar is 500 nm. (c) Designed (top) and fabricated (bottom) chiral metamaterial with two stacked layers [21]. The scale bar is 400 nm. (d) Designed (top) and fabricated (bottom) chiral metamaterial with two stacked layers [22]. The scale bar is 1 μm . (e) Sculptured thin film [86]. (f) Chiral photonic crystal [87]. (©2012 by the American Physical Society for (a); ©2012 by OSA for (b) and (c); ©2012 by the American Chemical Society for (d); ©2012 by Macmillan Publishers Ltd for (e); ©2012 by John Wiley and Sons for (f).)

The structure depicted in figure 2.16 (a) showed a rotation² of $\alpha = 1.5^\circ/100$ nm for a wavelength $\lambda = 630$ nm. Circular dichroism was measured in a double-layer planar chiral metamaterial [19] that is shown in figure 2.16 (b). The difference of the measured transmittances for RCP and LCP ($\Delta T = T_{\text{RCP}} - T_{\text{LCP}}$) for a wavelength $\lambda = 900$ nm was $\Delta T \approx 0.05$.

Through the stacking of mutually rotated structures (see figure 2.16 (c)), optical activity with a rotation of $\alpha = 15^\circ/100$ nm, and very small conversions were achieved at $\lambda \approx 3$ μm [21]. In [22], even $\alpha \approx 20^\circ/100$ nm was measured for wavelengths $\lambda \approx 1$ μm (figure 2.16 (d)).

In truly 3D, helical metamaterials [89–92], chiral effects can be even more enhanced. We will present structures with very high and broadband circular dichroism [89,92] for wavelengths $\lambda \approx 3.5 - 6.5$ μm in sections 6.1 and 6.3.

Chiral effects at optical wavelengths have also been measured in other artificial materials. For example, in sculptured thin films [86] (figure 2.16 (e)), a rotation $\alpha \approx 0.03^\circ/100$ nm was shown for wavelengths $\lambda \approx 600$ nm. In cholesteric liquid crystals [93], $\alpha \approx 4000^\circ/100$ μm [27] (please note the different length scale). In chiral photonic crystals [87,94] a very high difference in transmittances $\Delta T \approx 0.9$ has been measured [87] for wavelengths $\lambda \approx 1.8$ μm . The helical polymer structures are shown in figure 2.16 (f). Recently, a circular polarization filter was presented that uses a planar spiral nanoantenna to selectively transmit one circular polarization through a sub-wavelength hole while transmission of the other circular polarization is suppressed [95].

²In comparison, the rotation of a quartz crystal for a wavelength $\lambda = 590$ nm is $2.2^\circ/100$ μm [27] and the rotation of a sucrose solution for the same wavelength is $(6 \cdot 10^{-4})^\circ/100$ μm (for a concentration of 1 g/100 ml) [88]. Please note that here the length scale is μm .

3. Fundamentals of Electrochemical Deposition

In this chapter, we will introduce the basic terms used in electrochemistry as they obviously belong to a different subject area that a physicist may not be familiar with. The electrochemical equilibrium, processes due to applied currents, and the electrochemical deposition (ECD) of metals will be discussed. In the last part, we describe special requirements connected to the inversion of nanostructured templates by ECD.

For the interested reader we want to recommend the book “*Electrochemistry*” by C.H. Hamann, A. Hamnett, and W. Vielstich [96] which contains both a good introduction and profound information on this topic. A book containing a good description of ECD is “*Fundamentals of Electrochemical Deposition*” by M. Paunovic and M. Schlesinger [97]. A handy resource for chemical expressions is the RÖMPP online lexicon [88].

The origins of electrochemistry go back to antiquity. In old Egypt, it was known that iron objects can be covered by a Cu layer if they are dipped into a solution of copper sulfate. The onset of modern electrochemistry lies at the end of the eighteenth century and the beginning of the nineteenth century. At this time, L. Galvani conducted experiments with frog legs and A. Volta built the Voltaic pile, a forerunner of modern batteries. In 1832, M. Faraday formulated the basic laws of electrochemistry.

One application of electrochemistry is ECD, in an industrial context often called electroplating. ECD is the deposition of materials from an electrolyte solution. Modern ECD has its origins in the end of the eighteenth century. W. Cruikshank experimented with the electrolysis of solutions of heavy metal salts and saw that metals were deposited at the negative pole of his experimental setup [98].

Today, ECD is widely used for industrial as well as research purposes. A broad spectrum of different materials can be deposited: metals, alloys, metal oxides, and exotic mixtures, for example a Cu-multiwalled carbon nanotube composite has been reported [99]. By choosing appropriate materials and process parameters, it can be possible to deposit multilayers of different materials or to choose between polycrystalline and single crystal deposition [100].

3.1. Basic Terms in Electrochemistry

A term very often used in electrochemistry is the electrolyte. It signifies a solid or a liquid which contains ions and is able to conduct them. A typical electrolyte solution used in ECD can contain positively charged metal ions, negatively charged inorganic ions, and further components like organic molecules as we will describe later in detail.

Typically, an electrolyte is made by dissolving an ionic crystal in water. When an ionic

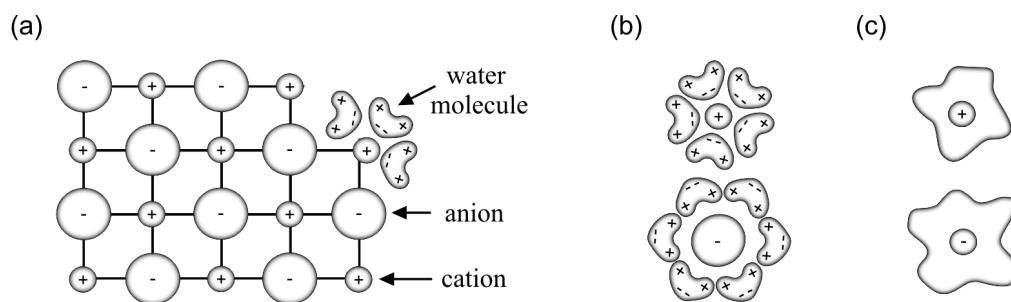


Figure 3.1 Ionic lattice and ions in an aqueous solution. (a) A cation in an ionic lattice is surrounded by water molecules and dissociated. (b) A cation and an anion with hydration shells. (c) Schematic representation of the solvated ions.

crystal is brought in contact with water (H_2O), ions are detached from the crystal lattice as depicted in figure 3.1 (a), they dissociate. This is due to the dipole nature of water molecules. For example, the negatively poled side of a water molecule orients towards a positive ion, called cation, due to the Coulomb force. In this manner, a solvation shell builds up around the ion. It is associated with the gain of solvation energy which delivers the dissociation energy needed to detach the ion. The difference between solvation energy and dissociation energy is either delivered by or dissipated in thermal energy. This leads to heating or cooling of the solution.

If the solvation shell consists of water molecules, it is also called hydration shell. Figure 3.1 (b) depicts a solvated, positively charged cation and a solvated, negatively charged anion. Two important facts are indicated: the anion has a bigger radius than the cation. This is due to its additional electron that is built into an outer orbital, thereby enlarging the radius. The bigger ion radius of the anion leads to a weaker binding of the hydration shell than in the case of a cation. In figure 3.1 (c), schematic representations of the ions are shown.

Electrolytic Cell

When two electrodes are connected to a constant current source and dipped into an electrolyte solution, the electric circuit is closed by ionic conduction of the solvated ions. Figure 3.2 shows such a simple electrolytic cell. The terminal voltage applied between the electrodes will be denoted as E_t . The cations move towards the negatively charged cathode and the anions towards the positively charged anode. At the electrodes, the ions are discharged. This can lead to the deposition of material at the electrode, the development of gas, the precipitation of solids in the electrolyte, or combinations thereof. For example, if the electrolyte contains metal cations me^{2+} and the electrode consists of metal atoms me , a reaction can take place at the cathode according to



The metal cation accepts two electrons and is deposited. This process, where electrons are accepted by an atom, ion, or molecule (in our case a metal ion), is called *reduction*. The opposite process happens from the viewpoint of a metal atom at the electrode. It donates

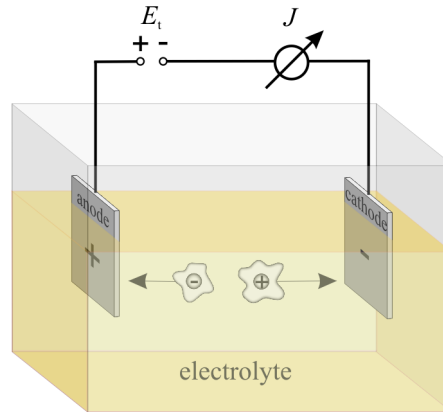


Figure 3.2 Simple electrolytic cell in a glass container. The electrolyte solution contains water, cations, and anions. A voltage E_t is applied between the electrodes and a current J flows.

electrons, which is called *oxidation*. The pair of one species which is oxidized and one species which is reduced is called a redox pair (a species can be a charged or uncharged atom or molecule).

Through the discharge of ions at the electrodes, a current flows through the electric circuit. The flow of ions through the electrolyte equals to the electron flow in the remainder of the electric circuit. The mass m of the ions which are transformed at one electrode is proportional to the amount of charges Q which has been transferred between the electrode and the electrolyte. This is expressed in the first Faraday law:

$$m = \text{const} \cdot Q. \quad (3.2)$$

When the amount of ions which have been transformed through the electrode reaction equals one mole, the associated amount of charges is

$$Q = n_e e N_A \cdot 1 \text{ mol}, \quad (3.3)$$

where n_e gives the amount of electrons exchanged each time the electrode reaction takes place and $N_A = 6.022 \cdot 10^{23} \frac{1}{\text{mol}}$ is the Avogadro constant. The quantity

$$F = N_A e = 96485 \frac{\text{As}}{\text{mol}} \quad (3.4)$$

is called the Faraday constant. It is equal to the amount of electrons exchanged by one mole of ions with the electrode if only one charge is transferred each time an electrode reaction takes place. The electrical energy necessary to transform one mole of ions at the electrode can be introduced as

$$W = n_e F E_t. \quad (3.5)$$

Conditions of Electrochemical Reactions

Whether a reaction takes place without external activation or not, depends on the sign of the free enthalpy of reaction ΔG . It is a sum of the chemical potentials μ_s of the species s which would take part in the reaction.

$$\Delta G = \sum_s \gamma_s \mu_s. \quad (3.6)$$

The stoichiometric number γ_s tells us how many units of each component take part in one reaction. In the case of an electrolytic cell, there are three possible states, depending on the free enthalpy of the reaction at each electrode and the associated electric energy W :

- $\Delta G = -W$. The system is in an electrochemical equilibrium. The amounts of negative and positive charges which are exchanged at each electrode are equal.
- $\Delta G < -W$. The reaction takes place without external activation and a current is generated. This is called a Galvanic cell. Examples for Galvanic cells are batteries, accumulators, and fuel cells.
- $\Delta G > -W$. The reaction only takes place if the electric energy W is provided. In this case, we have an electrolytic cell. Examples for the use of electrolytic cells are the industrial production of many different substances like metals, chlorates or oxygen. Another important example is the ECD of metals.

Chemical Potential and Activity

The chemical potential μ_s of a species s can depend on its concentration in a medium. An ion which is solvated in an electrolyte solution will be surrounded by solvated ions with the opposite charge. Before the ion can take part in a chemical reaction, it has to get rid of the surrounding ions, first. Thus, its chemical potential is lowered. This effect grows stronger with growing ion concentration in the solution and is expressed with the help of an effective concentration, the activity a_s :

$$a_s = f_s c_s, \quad (3.7)$$

where the coefficient f_s considers the deviations from $a_s = c_s$ that can be present in an ion solution. Using the activity coefficient, the chemical potential of a species can be written as

$$\mu_s = \mu_s^0 + RT \ln a_s, \quad (3.8)$$

with μ_s^0 being the chemical potential under standard conditions, $R = 8.31 \frac{\text{J}}{\text{mol K}}$ the gas constant, and T the temperature.

The pH Value

The pH value provides a measure for the acidity or the basicity of aqueous solutions. It is defined as the negative decimal logarithm of the activity of hydrogen ions H^+ which are present in an aqueous solution:

$$pH = -\log a_{H^+}. \quad (3.9)$$

An acid solution has a $pH < 7$ while a basic solution has a $pH > 7$. Solutions with $pH = 7$ are neutral.

The pH value is an important parameter in ECD as it can influence which reactions take place at the electrodes. Usually, a constant pH value is desired during ECD. In order to keep the pH value of a solution constant, buffers are used. These are solutions with a pH value that stays constant if a reasonable amount of an acid or a base is added.

3.2. Electrochemical Equilibrium

In this section, we will discuss the electrochemical equilibrium. We will look at the interface between an electrolyte solution and different types of electrodes which are used later on for our fabrication process. At such an interface, an electrochemical double-layer builds up which will be described. The electrochemical double-layer is accompanied by an electrical potential of the electrode that has strong influence on the ECD at an electrode. This can be estimated using the standard potential which we will explain in the last part of this section.

3.2.1. Interface between Electrode and Electrolyte Solution

When an electrode is brought in contact with an electrolyte, depending on the system, different processes will take place. We will describe these processes for the case of a metal electrode, an inert metal electrode, and a semiconductor electrode as these are used in our fabrication processes.

Metal Electrode

Imagine a piece of metal (me) that is immersed into an aqueous electrolyte solution which contains z -fold charged ions of this metal. Usually, the chemical potentials of the metal and the electrolyte solution are different:

$$\mu_{me} \neq \mu_{me^{z+}}. \quad (3.10)$$

For example, if $\mu_{me} < \mu_{me^{z+}}$, metal cations from the solution will be discharged and deposited at the electrode. Through the reduction of the metal ions, the electrode loses electrons and becomes positively charged. Hence, it attracts the anions which are present in the solution as shown in figure 3.3 (a). After a short time, a potential difference $\Delta\varphi$, called Galvani potential difference, results and a so called electrochemical double-layer is built up. $\Delta\varphi$ is associated with a Coulomb force that repels further cations from the electrode and the system is in electrochemical equilibrium.

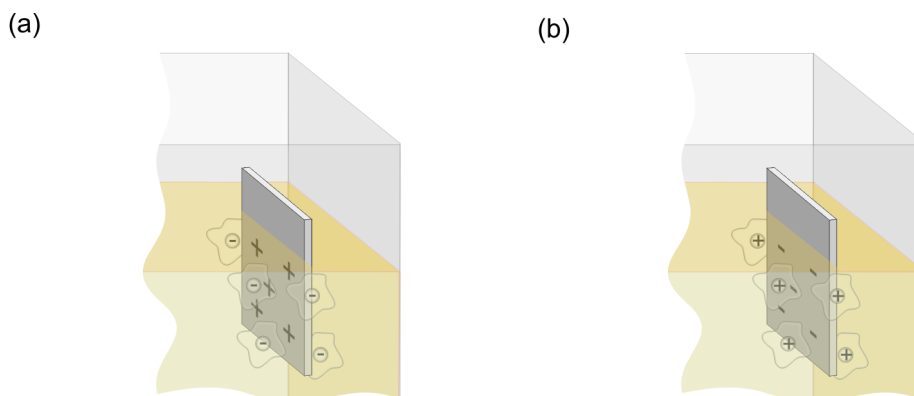


Figure 3.3 A metal electrode dipped into an electrolyte solution containing ions of the same metal in electrochemical equilibrium. (a) $\mu_{\text{me}} < \mu_{\text{me}^{z+}}$ leads to positive charges at the metal side and negative charges at the electrolyte side of the interface. (b) $\mu_{\text{me}} > \mu_{\text{me}^{z+}}$ leads to negative charges at the metal side and positive charges at the electrolyte side of the interface.

If $\mu_{\text{me}} > \mu_{\text{me}^{z+}}$, cations will be dissociated from the metal and solvated by water molecules in the solution. Thus, the electrode will be charged negatively and surrounded by positively charged cations as depicted in figure 3.3 (b). Again, the reaction is stopped through the build-up of a Galvani potential difference and an electrochemical double-layer.

Redox Electrode

If we dip an electrode made of an inert metal like platinum into an electrolyte solution, it will develop an electrode potential, too. This is because an electrolyte, in general, contains redox pairs. They can donate or accept electrons at the electrode which serves as a catalyst. As the chemical potential of the electrons is different inside the electrode metal and inside the electrolyte, a Galvani potential difference and an electrochemical double-layer results and the process is stopped.

Semiconductor Electrode

If a semiconductor is dipped into an electrolyte, the electrochemical equilibrium state will be different from what we discussed for metal electrodes. For example, if the electrode is oxidized through the deposition of positive ions, it will be charged positively. In a semiconductor, this leads to a depletion region. As the conductivity of the electrolyte is higher than the conductivity of the semiconductor, no depletion region evolves in the electrolyte and there will be only a monolayer of anions at the interface to the electrode. Thus, a potential drop is present inside the semiconductor but not within the electrolyte.

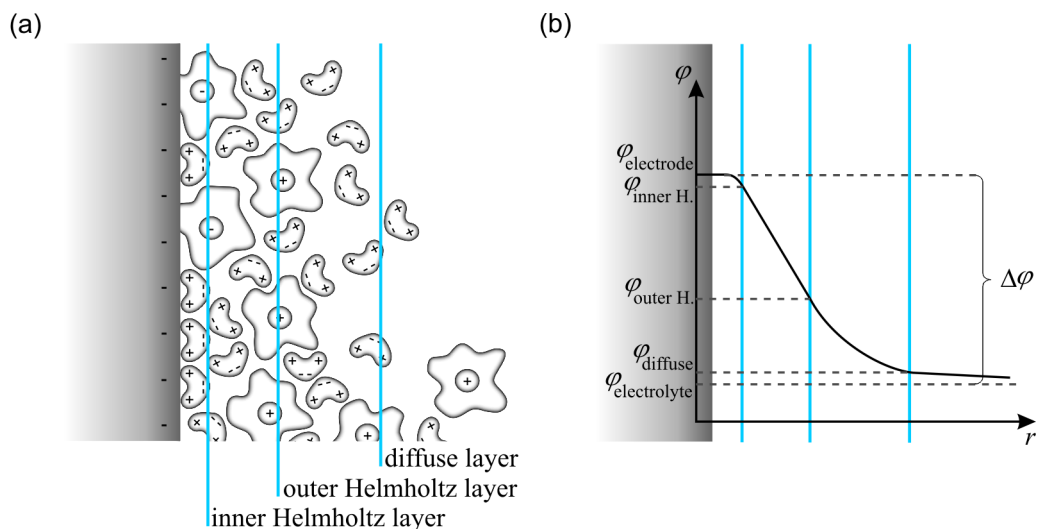


Figure 3.4 The electrochemical double-layer. (a) A schematic depiction of anions, cations, and water molecules in the electrochemical double-layer of a negatively charged electrode. The blue lines indicate the positions of different layer boundaries. (b) Qualitative diagram of the electrode potential depending on the distance to the electrode r (following [96]).

3.2.2. Electrochemical Double-Layer

We already mentioned the electrochemical double-layer. Now, we want to describe its structure. Imagine a negatively charged electrode as depicted in figure 3.4 (a). It will be surrounded by cations due to the Coulomb force. However, further forces act at the electrode surface: Van der Waals and chemical forces. Thus, beneath cations, there will also be adsorbed anions, oriented water molecules, and other components of the electrolyte solution at the electrode.

The adsorption is due to Van der Waals forces and thus affects both anions and cations. Before adsorption, an ion has to strip off its hydration shell. As the binding of the hydration shell is weaker for anions, they are adsorbed preferentially. Thus, directly at the electrode, mainly adsorbed anions and oriented water molecules will be present. The plane through the gravity centers of the adsorbed anions is called the inner Helmholtz layer. It is shown in figure 3.4 (a). As indicated in figure 3.4 (b), the potential drop between the electrode and the inner Helmholtz layer is small.

The next layer is a monolayer of cations. They are attracted by electrostatical forces. The plane through the gravity centers of the cations is called the outer Helmholtz layer. The potential drop between inner and outer Helmholtz layer is assumed to be linear.

The outer Helmholtz layer is followed by a region with enhanced cation concentration, the diffuse layer. There, the potential drop is exponential. The outer limit of the diffuse layer is marked by a drop of the potential to $1/e$. The resulting structure and qualitative course of the potential drop are shown in figure 3.4.

3.2.3. The Standard Potential

Because of the Galvani potential difference $\Delta\varphi$ at the interface between electrode and electrolyte, the condition for electrochemical equilibrium does not only depend on the chemical potentials of the metal and the metal ions, μ_{me} and $\mu_{\text{me}^{z+}}$, but also on the respective electrical potentials. In order to move one mole of a z -fold charged ion along a potential difference $\Delta\varphi$, the electrical energy $W = zF\Delta\varphi$ is required. Thus, the condition for electrochemical equilibrium is given as

$$\mu_{\text{me}^{z+}} + zF\varphi_{\text{me}^{z+}} = \mu_{\text{me}} + zF\varphi_{\text{me}}. \quad (3.11)$$

The Galvani potential difference for the equilibrium state $\Delta\varphi_0$ can be deduced from (3.11) and (3.8):

$$\Delta\varphi_0 = \varphi_{\text{me}} - \varphi_{\text{me}^{z+}} = \frac{\mu_{\text{me}^{z+}}^0 - \mu_{\text{me}}^0}{zF} + \frac{RT}{zF} \ln \frac{a_{\text{me}^{z+}}}{a_{\text{me}}}. \quad (3.12)$$

Usually, it is advantageous to measure the electrode potential φ_{me} not with respect to the electrolyte but with respect to a reference electrode. The electrode potential of a reference electrode is zero per default. In that case, the term in (3.12) which contains the difference of chemical potentials is called the standard potential φ_{00} . The activity of the metal electrode is $a_{\text{me}} = 1$ for a pure metal. With these replacements, we finally arrive at the equilibrium electrode potential φ_0 of a metal electrode. It is given by the Nernst equation:

$$\varphi_0 = \varphi_{00} + \frac{RT}{zF} \ln a_{\text{me}^{z+}}. \quad (3.13)$$

The Nernst equation for a redox electrode is

$$\varphi_0 = \varphi_{00} + \frac{RT}{zF} \ln \frac{a_{\text{ox}}}{a_{\text{red}}}, \quad (3.14)$$

where a_{ox} and a_{red} are the activities of the oxidized and reduced species.

As we mentioned, it is often desirable to have a value for the equilibrium electrode potential φ_0 . However, it is hard to acquire the electrolyte potential $\varphi_{\text{me}^{z+}}$. In a measurement, one can only get the potential difference between two electrodes which are dipped in the electrolyte. Thus, a fixed, standardized electrode has been introduced, the standard hydrogen electrode. Its potential is set to zero per definition.

The Galvani potential difference in equilibrium, $\Delta\varphi_0$, of an electrode measured against the hydrogen electrode is the standard potential of the electrode φ_{00} . When a redox pair has a large, positive standard potential, the oxidized species will tend to be reduced while the reduced species will be stable. For example, this is the case for Au and other noble metals. For a large, negative standard potential, the situation is reversed and the reduced partner is oxidized.

The standard hydrogen electrode is rarely used in experiments because of its complicated

setup. Usually, one uses electrodes with a well-known potential which is very stable under experimental conditions. In our case, a silver chloride electrode will be used.

3.3. Electrochemical Deposition of Metals

Imagine an electrolytic cell with two electrodes in equilibrium. In this section, we want to discuss the conditions for the deposition of a metal when a terminal voltage is applied at these two electrodes and describe how metal layers form.

3.3.1. Terminal Voltage and Current Flow

In order to get a certain current flow through an electrolytic cell, a terminal voltage has to be applied to the two electrodes. This voltage depends on the ohmic resistance of the electrodes and wires, but also on the potential of the electrodes.

Before charge transfer, solvated ions have to arrive at the double-layer of an electrode and have to be transferred to the electrode. Also, some chemical reactions may be necessary before, during or after the charge transfer. These processes can slow the current flow and lead to a deviation of the electrode potential from the equilibrium electrode potential φ_0 . This deviation is called the overpotential $\nu = \varphi - \varphi_0$. The difference in the potentials of the two electrodes, φ_1 and φ_2 , gives the minimal terminal voltage that is necessary to achieve current flow:

$$E_{t,\min} = (\varphi_{0,1} + \nu_1) - (\varphi_{0,2} + \nu_2). \quad (3.15)$$

The value of the current flow is determined by the slowest of the processes which lead to the overpotential. In the following, we describe the most important involved processes:

- Often, a big part of the overpotential is due to the penetration of ions from the electrolyte to the electrode: the ions have to cross the Helmholtz layers in order to arrive at the electrode interface and they have to be discharged.
- As ions are transformed at the electrode, they need to be replaced by new ions. First, new ions have to arrive at the outer limit of the diffuse layer. This is achieved either by migration of the ions due to the electric field between the electrodes, or by convection, for example by stirring of the electrolyte. Then, the ions have to diffuse to the inner Helmholtz layer. When less new ions arrive than are transformed, this results in a concentration gradient between the inner Helmholtz layer and the electrolyte and a concentration overpotential.
- The electrochemical process can involve one or several chemical reactions which lead to a reaction overpotential if they are slower than the remaining processes. For example, such reactions might be necessary to provide reaction partners for the electrode reaction.
- In the case of metal cations at a metal electrode which is not inert, the discharged metal atoms have to be built into the metal lattice.

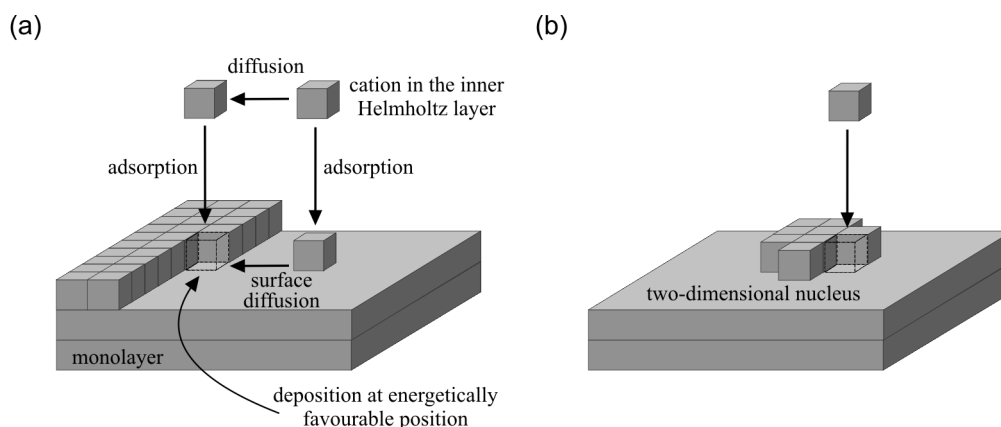
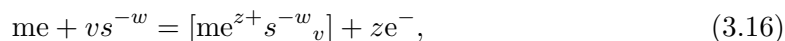


Figure 3.5 Depiction of different deposition schemes for growth on a single crystal. (a) Deposition at the edge of a monolayer, and (b) 2D nucleus on a big flat area.

- A further step that can lead to an overpotential is an adsorption or desorption of species at an electrode.

If the applied terminal voltage between two electrodes has a sufficiently high value, metal cations will be deposited at the cathode. Imagine z -fold charged cations me^{z+} which are surrounded by v complexing¹, w -fold charged, species s^{-w} . The reaction at the cathode can be written as:



where the square brackets indicate the complex. At one electrode, cations will be reduced while at the other electrode, anions will be oxidized. Thus, the reactions can be reversed if the sign of E_t is changed and if no irreversible chemical reactions are involved.

3.3.2. Metal Growth

How do metal films evolve during ECD? Let us look at the lattice of a single crystal (see figure 3.5). A cation in the inner Helmholtz layer has two possibilities: either it moves to an energetically favored position and is built into the crystal there, or it is adsorbed directly and moves to an energetically optimal position *via* surface diffusion. There, it detaches remainders of its hydration shell or complexing agents, is discharged, and deposited onto the crystal lattice.

Energetically favorable positions often are edges and steps of monolayers as indicated in figure 3.5 (a). Usually, this leads to the growth of monolayers along the crystal surface. In big, flat areas of a single crystal, a 2D nucleus can be built by adsorbed ions (figure 3.5 (b)). Through the deposition of further ions, a new monolayer evolves.

¹A complex is formed by a central atom that is surrounded by one or several species which deliver at least one free electron pair for a bond. The resulting bond is polar and covalent.

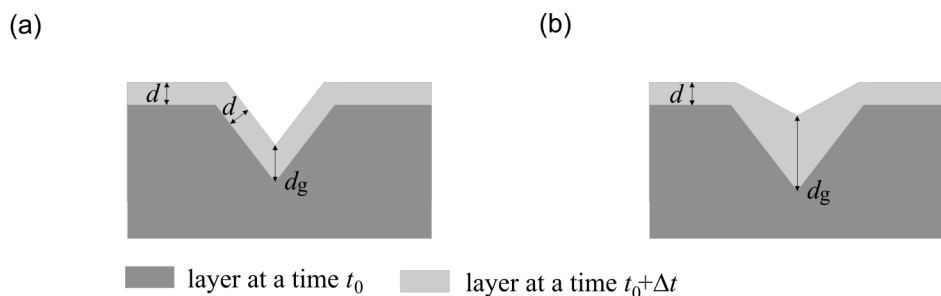


Figure 3.6 Different leveling mechanisms. (a) Geometrical leveling, and (b) electrochemical leveling.

The electrodes used within this work are polycrystalline and have a certain degree of roughness. Hence, the deposited metal layer will also be rough. After a first layer of nuclei has been deposited, there are two possibilities: The present nuclei can grow upwards, leading to a columnar structure of the deposit. This is usually the case for small current densities. The other possibility is the growth of new nuclei on the first layer. This results in a polycrystalline structure and is usually the case for high current densities. A high current density leads to a high deposition rate. Thus, the adsorbed cations have less time to diffuse and many new nuclei start growing on the existing layer.

As described in section 3.3.1, the growth rate increases with increasing terminal voltage. More importantly, it is also increased locally at positions with a high electric field. Such positions are spikes and sharp edges. This can result in a roughening of the surface. In combination with a small conductivity of the electrolyte or a very high current, even dendritical growth can result. In our case, flat surfaces are required. This can be achieved by using geometrical or electrochemical leveling.

In geometrical leveling, the thickness of the deposit normal to the substrate d is independent of the local geometry. This leads to a slightly higher layer thickness d_g inside of a groove as shown in figure 3.6 (a). Geometrical leveling is achieved through homogeneous current distributions, for example by the use of a high cation concentration.

For electrochemical leveling, inhibitors are used to slow the growth at the surface (see figure 3.6 (b)) [97]. Inhibitors are substances which are adsorbed at the surface more easily than the cations. They will preferentially be adsorbed at positions with a high electric field, where they hinder the adsorption of cations and thus enhance the growth in grooves, where the electric field is small. Inhibitors can be components of the electrolyte solution, colloidal particles or organic substances. The last are often used in ECD in order to improve the quality of deposited materials.

3.4. Inversion of Nanostructured Templates

The fabrication of metallic nanostructures by ECD can be achieved by different means. One possibility is the direct growth of nanostructures using dendritic growth [101, 102] or the direct deposition or dissolution of metal structures using a scanning tunneling

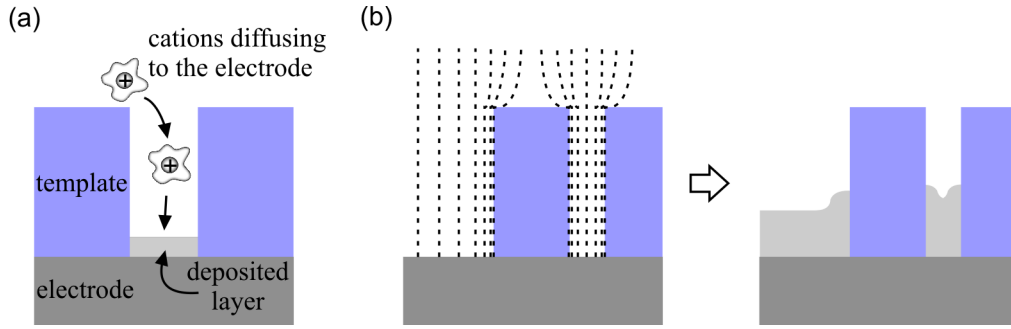


Figure 3.7 Growth inside template channels. (a) Diffusion of cations through a small template channel, and (b) distribution of electric field lines and the resulting deposited layers (following [26]).

microscope [103]. The other possibility is to use nanostructured templates. These can be either metalized by electroless deposition [104] or inverted by ECD. We chose the last method as it is best suited for our purpose. It is a well established method for the fabrication of two- and partially 3D metal microstructures within the LIGA² process [105]. It has also been used for the fabrication of metal photonic crystals as reported in [106,107].

The electrochemical inversion of templates with narrow channels on the size scale of tens of nm to several μm imposes certain requirements to the whole ECD processes [26,108]. First of all, the templates have to stand on a conducting substrate that can be used as cathode. Also, the electrolyte has to get into the channels. This can be problematic because of the viscosity of aqueous solutions. We will come back to these two points in section 4.2.

Let us assume that the electrolyte has completely wetted the template and the substrate. When the deposition starts, the cation concentration near the substrate will be depleted. Because of narrow channels, a convection is not possible inside the template. Thus, the cations have to diffuse all the way from the top of the template to the conducting layer as depicted in figure 3.7 (a). This imposes an additional concentration overpotential. Thus, if only part of the substrate is covered by the template, the deposition rate inside the template will be decreased in comparison to the open substrate. Also, depending on the length of different channels, the growth inside the template may vary locally.

When the voltage is switched on, the distribution of the electric field will vary locally. On the one hand, this is due to high field intensities at spikes and edges as described above. On the other hand the electric field can be enhanced at the edges of template channels [26]. In figure 3.7 (b), the distribution of field lines along channels in the template is shown. This leads to enhanced growth in small channels and at template edges and competes with hindered growth due to the concentration overpotential.

In order to achieve metal surfaces which are as uniform as possible both inside and outside of a template, in addition to geometrical and electrochemical leveling, pulsed

²LIGA is an acronym which stands for the German expression “**L**ithographie, **G**alvanoformung und **A**bformung”, lithography, electroplating, and molding.

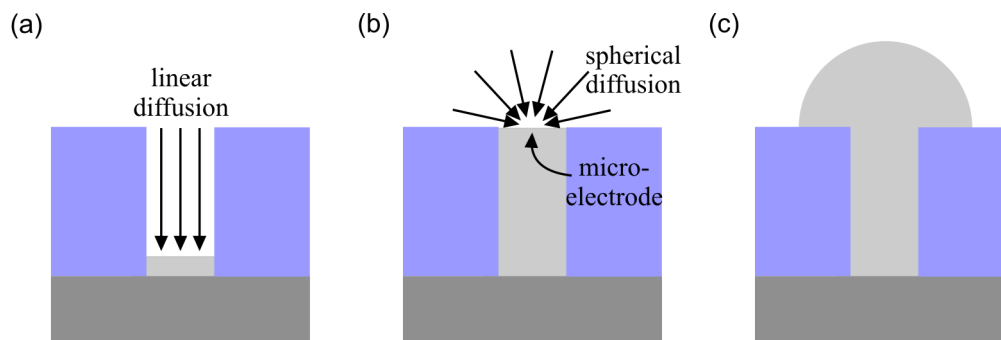


Figure 3.8 Growth of metal at microelectrodes. (a) Linear diffusion, (b) resulting microelectrode, and (c) spherical growth above the microelectrode.

deposition can be used [109]. The basic idea is to apply a voltage for such a short time that the concentration overpotential is negligible. Then, the voltage is switched off and the cation concentration can recover by diffusion. When the voltage is applied, first the electrochemical double-layer has to be built up and loaded. This can be compared to the loading of a plate capacitor. This means that the voltage has to be applied for at least as long as this loading time in order to achieve deposition. Pulsed deposition has yet another advantage: cation depletion can be neglected and, therefore, high currents can be applied in the growth phase. We already mentioned that a high current enforces the formation of many nuclei. In addition, these will be smaller because the adsorbed ions do not have enough time to form larger clusters. The resulting deposit will usually have a finer, polycrystalline structure and a good uniformity of the deposited metal.

During the growth of a metal in a template cavity, cations arrive at the electrode by linear diffusion through the template as indicated in figure 3.8 (a). If the cavity is completely filled, a so called microelectrode results (figure 3.8 (b)). The diffusion towards microelectrodes is spherical, which leads to a spherical growth behavior above the microelectrode as shown in figure 3.8 (c) [110]. The SEM micrograph in figure 3.9 corresponds to figure 3.8 (c). It shows fabricated Au structures after the template has been removed.

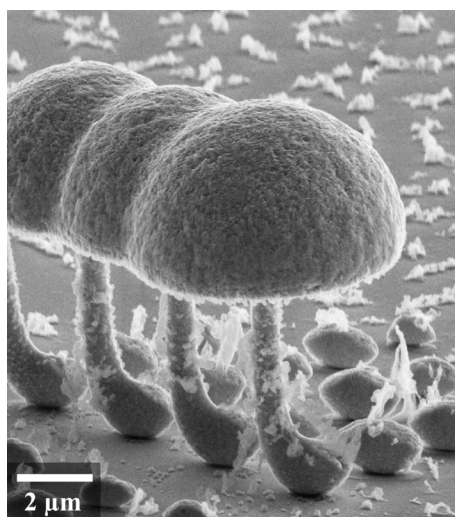


Figure 3.9 Au structures with spherical shapes due to spherical diffusion. The white flakes are residues of the template.

4. Fabrication of Helical Metamaterials

3D fabrication techniques are of major importance for the realization of optical metamaterials. We already pointed out in section 2.1.5 that they are necessary if one wants to design truly isotropic building blocks or if one wants to fabricate bulk metamaterials rather than thin films. More importantly, 3D fabrication methods allow to make structures with completely new properties that are not possible with planar metamaterial layers.

This is even more the case for chiral metamaterials. In 3D space, chirality cannot be realized by flat, 2D objects. In section 2.3.7, we gave some examples of chiral materials which show that chiral effects are much stronger in 3D metamaterials than in “thin-film” metamaterial layers. The realization of *helices* and thus helical metamaterials is impossible without 3D fabrication techniques.

In the first part of this chapter, we want to give an overview of existing 3D fabrication methods in order to motivate the method which was developed within this thesis. In the following section, we will give an overview of the single steps in our fabrication process, focusing on the new aspects of these steps. The major new process step was to implement the ECD of different materials within our fabrication process and hence, we will present this in separate sections.

We established the deposition of four different materials. One is Au, which is the metal of choice for the fabrication of optical metamaterials, as we pointed out in section 2.1.4. The helical optical metamaterials which will be discussed in chapter 6 are made of Au.

In addition, we set up further ECD methods. We deposited Ni, as it could be interesting in the realization of metamaterial functionalities based on high absorption as well as for its ferromagnetic properties. Also, the ECD of copper(I) oxide (Cu_2O) was established because it could be used for the realization of metal-dielectric heterostructures in the infrared spectral region, and because it is interesting due to its semiconductor properties. We will see, that from the same electrolyte solution as used for Cu_2O , also Cu can be deposited.

4.1. Fabrication Methods for Three-Dimensional Metamaterials

Optical metamaterials usually demand the fabrication of metal nanostructures with feature sizes of tens of nanometers to several micrometers. The most common approach is to use electron-beam lithography (see, *e.g.* [6]). With an electron beam, a photoresist mask is created and a material is evaporated onto it. Afterwards, the mask is removed, resulting in planar nanostructures. Extensions of this process enable the fabrication of layered structures. One possibility is to evaporate several layers of different materials [19, 46]. Another way is to planarize the first layer, apply new resist onto it, and by this means

fabricate further layers [20, 48, 111]. Yet another possibility is to first evaporate different materials and then structure them using a focused ion beam (FIB) [47]. However, these approaches either yield structures with no geometrical variation normal to the substrate, or structures consisting of multiple planar layers and thus still not being truly 3D. In addition, multilayer processes are very time-consuming.

The combination of different resists [112] or different materials and etching processes [113] with electron-beam lithography leads to the fabrication of “2.5-dimensional” structures, however at the expense of structure quality.

Reference [114] reported the fabrication of single metallic 3D structures by using electron-beam induced deposition. A very recent approach, membrane projection lithography, uses an electron-beam structured membrane through which Au is evaporated into an underlying void [115, 116]. By changing the incidence angle, structures can be evaporated onto different walls of the void. Although the structures are quite large, this is a promising approach under the condition that the void material does not disturb the optical properties.

3D nano- and microstructures with almost arbitrary shapes can be fabricated using direct laser writing (DLW) [23, 24, 117, 118] into a photoresist. The direct writing of metal structures by DLW has been demonstrated in [119, 120]. However, both resolution and structure quality of directly written metal structures are not sufficient for the fabrication of 3D optical metamaterials. Thus, polymer structures are made by DLW and metallized or inverted by a metal in a second step. Metallization of polymer structures has been realized by means of chemical vapor deposition [40, 60] and, recently, by electroless plating [91]. However, by using these techniques, the substrate is also metallized and strongly influences the material properties. If the structures are connected and stable, they can be detached from their substrate and put onto a new one [91]. In [104, 121], only the polymer was metallized through a functionalization of the substrate. Recently, even optical measurements have been reported [121], though with rather low structure quality. Our approach is to invert polymer templates by a metal using ECD. This method allows to fabricate 3D metal metamaterials that are standing on a substrate which is not metallized. In addition, the metal structures are mechanically stable and hence, the polymer resist can be removed before optical measurements. A disadvantage of our and the other DLW approaches in comparison to electron-beam written layered structures is, that electrically disconnected structures normal to the substrate cannot be fabricated. This could be achieved by using a heterostructure process (see chapter 7).

Many other methods for the fabrication of 3D metal nano- and microstructures have been published that might be or have been used to make metamaterials. However, they either are limited to fixed structure designs or lead to inhomogeneous arrays of structures [90, 122, 123]. We also want to point out some methods based on self-organization that can lead to the fabrication 3D structures [102, 124–127].

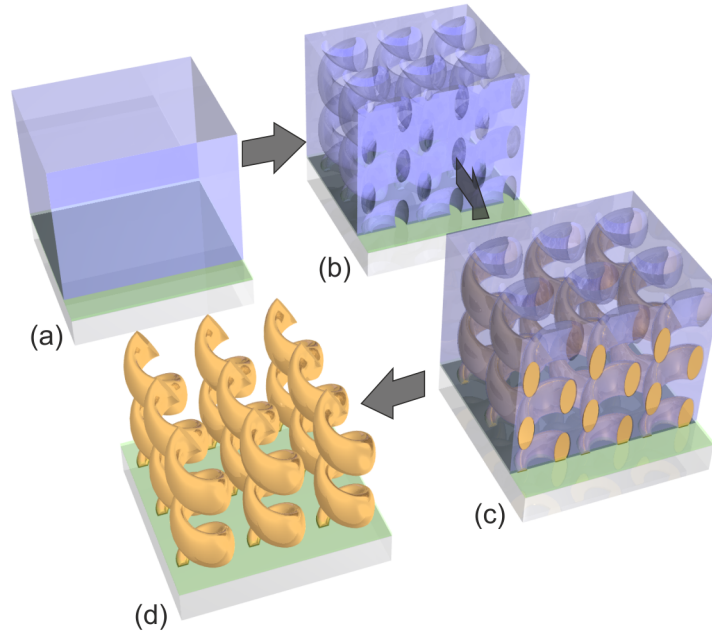


Figure 4.1 Overview of the fabrication steps. (a) A glass substrate (gray) is coated with a transparent conducting electrode (green) and a photoresist layer (blue). (b) After DLW (in this case, arrays of helices are written into a positive tone photoresist) and development, a template with helical channels results. (c) Then, the template is inverted with a material (golden) by using ECD. (d) After resist removal, an array of 3D structures, in this case helices, results [89].

4.2. Our Fabrication Method

We want to describe our fabrication method in this section. First, we will give an overview of the whole process and then explain the single steps in more detail. We start our fabrication process with a glass substrate. Onto it, a conducting, transparent electrode and a photoresist layer are placed as depicted in figure 4.1 (a). The photoresist contains a photoactive substance which is exposed by a laser using DLW. Through exposure, the photoactive substance leads to a solubility change in the exposed regions. After DLW and development, a template on the electrode results. In case of a positive tone photoresist, the exposed regions are dissolved as shown in figure 4.1 (b), while the unexposed regions are dissolved in the case of a negative tone photoresist. Then the template is wetted, so that the electrolyte solution can fill the template channels, and subsequently inverted with metal by ECD (figure 4.1 (c)). In a last step, we remove the resist and obtain freestanding 3D metal metamaterials (see figure 4.1 (d)).

Using this method, high aspect ratio 3D structures with very diverse structure designs and feature sizes of half a micrometer can be fabricated. We will now give a more detailed description of the single process steps. The ECD step will be described separately for different materials in sections 4.3 to 4.5.

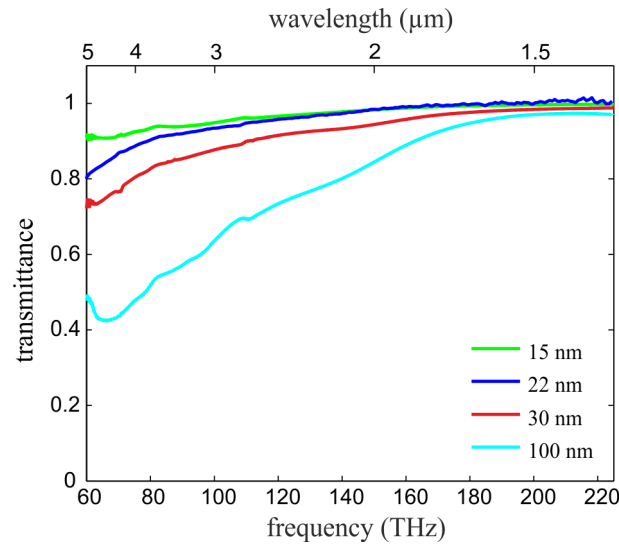


Figure 4.2 Optical transmittance spectra of ITO films with different film thicknesses.

Indium Tin Oxide Electrodes

We start with a clean cover glass for microscopy (*e.g.* Menzel Gläser, $22 \times 22 \times 0.17 \text{ mm}^3$). Using electron-beam evaporation, indium(III) oxide (In_2O_3) doped with 10% tin dioxide (SnO_2) is deposited on the glass substrate [128]. The resulting indium tin oxide (ITO) film is grey and reflecting. It is annealed for one hour per nm film thickness at 450°C in order to get a transparent film with good conductivity [129, 130]. We deposited ITO films with a thickness between 15 nm and 100 nm and evaluated their properties. For DLW and optical measurements, high transparency is necessary, which increases with decreasing film thickness. Figure 4.2 shows transmittance spectra of ITO films with different thicknesses (the spectra were measured with the setup described in section 5.1). While the transmittances are high towards high frequencies, they decrease for low frequencies. For the ECD, we want high electrical conductivity in order to prevent inhomogeneous deposits, which is improved with increasing film thickness. Within this work, we use ITO films with a thickness of 22 nm. They combine a good transmissivity and a sufficiently low sheet resistance: we typically measured about $500 \Omega/\square$ using a four-point probe setup.

Direct Laser Writing

In the next step, a suitable photoresist is spun onto the ITO film and exposed by DLW. As the requirements to the photoresist result from the DLW, we want to describe it first. In DLW, a photoresist is exposed by a focused, usually pulsed laser beam. The chemical reaction involved in the exposure takes place when the laser intensity lies above a certain threshold value. This value is exceeded only within an isointensity surface of the focal volume. Thus, the photoresist is only exposed within this small volume. In analogy to a picture element (pixel), this volume element is called voxel. As the focus is elongated along the propagation direction of the laser beam, voxels have an ellipsoidal form. By moving the substrate with respect to the laser beam, 3D structures can be written into

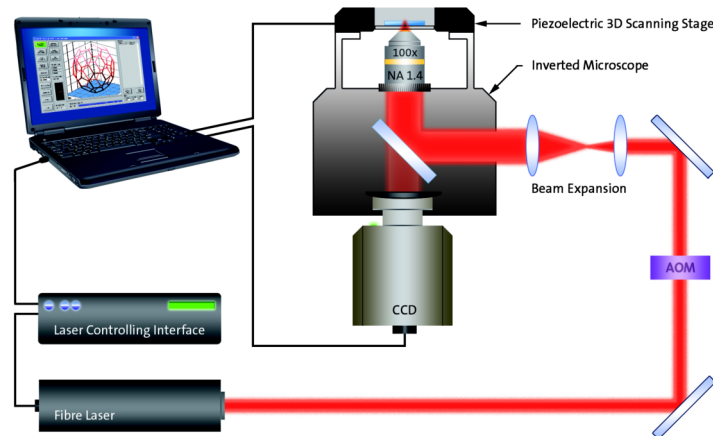


Figure 4.3 Schematic of the used DLW system Photonic Professional [137].

the photoresist.

Obviously, the resolution strongly depends on the size and the ellipticity of the voxel. It can be reduced by using a microscope objective with high numerical aperture, oil immersion, and a refractive index matched photoresist, as this directly leads to a smaller focal volume. The size of the isointensity surfaces can also be reduced by using a smaller laser intensity. However, below a certain intensity level, the process becomes unreliable because of fluctuations of the laser intensity and varying properties of the photoresist.

An additional reduction of voxel size can be achieved by using two-photon absorption. To this end, a photoresist is used that is transparent at the wavelength of the laser but can be exposed at half of the wavelength. The absorption rate for two-photon absorption is proportional to the square of the intensity while for one-photon absorption, it is directly proportional to the intensity. The spatial shape of an isointensity surface is narrower and has much smaller side maxima for the square of the intensity than for the direct intensity, leading to a smaller voxel for two-photon absorption. More importantly, due to smaller side maxima, the so called proximity effect can be reduced. It can take place when enough energy for exposure is accumulated outside of a voxel.

Recently, techniques inspired by stimulated emission depletion microscopy [131, 132] have lead to further resolution improvement in DLW and to a strong reduction of the ellipticity of the voxel [133–136]. Due to material and processing constraints, these techniques are presently not incorporated in our method.

Within this thesis, we used the DLW system Photonic Professional, which is commercially available from Nanoscribe GmbH [137]. It uses a fiber laser with 150 fs pulse length, 100 MHz repetition rate, and a wavelength of 780 nm. As depicted in figure 4.3, the laser intensity is controlled by an acousto-optic modulator (AOM). After expansion of the beam, it is coupled into an oil-immersion microscope objective with a numerical aperture of 1.4 and focused into the resist. Depending on the photoresist, a resolution down to 100 nm is possible with this system. A piezoelectric 3D scanning stage with a sample holder is used to move samples with respect to the laser beam. Through a programmable

computer interface, the piezoelectric stage and the AOM are controlled, thereby allowing for exposure of a photoresist at predefined positions with a variable voxel size. In addition, the commercial system possesses an interface finder which can automatically find the interface between glass substrate and photoresist and a tilt correction system that can adjust writing coordinates when a glass substrate has a slight tilt with respect to the piezoelectric scanning stage. Additionally, up to ten substrates can be placed into the system simultaneously as the sample holder can be displaced by large distances with the help of an electrical moving stage.

Photoresists

Of course, the quality and resolution of a template does not only depend on the used DLW system but also on the photoresist, its optical and chemical properties, and its processing.

For our purposes, the photoresist should have a refractive index near 1.5 in order to match the refractive index of the used glass substrate. It should be transparent at 780 nm and absorbing for ultraviolet wavelengths smaller than 390 nm. For optical measurements, the photoresist should either be transparent for interesting wavelengths or it should be possible to remove it after ECD. Removal of the photoresist should be possible by ashing or dissolving it (we will describe this in detail in the last part of this section). A lift-off from the substrate is not compatible with our process because the deposited 3D structures would be dragged away by the photoresist. In addition, we need a photoresist that can be processed with a thickness of many micrometers (as this limits the height of our structures) and leads to a high resolution.

With respect to the ECD step, the photoresist should be stable in the electrolyte solution. For use in an ECD process, a positive tone photoresist is advantageous because it allows to directly write the desired structures during DLW. In a negative tone resist, one would have to write the shells of the desired structures which can be complicated because of the proximity effect. In addition, a positive resist covers the whole substrate. Thus, material will only be deposited in the written channels. This can be important if macroscopic deposited films tend to peel off the electrode (we will discuss this in more detail in section 4.3).

Within this work, we mainly used the positive tone resist AZ9260 from MicroChemicals GmbH [138]. Also, the negative tone resist SU8 from MicroChem Corp [139] was adapted for the process.

The AZ9260 Photoresist

The AZ9260 photoresist is based on the resin Novolak, a phenol-formaldehyde type polymer. The photoactive substance is diazonaphthaquinone (DNQ). The used solvent is 2-[1-methoxy]propyl acetate (PGMEA). Before exposure, DNQ leads to a low solubility of the resin. When exposed, DNQ transforms into a carboxylic acid, thereby separating nitrogen and incorporating a water molecule. This leads to a strong increase of the solubility in the exposed regions. Using the developer AZ400K (MicroChemicals GmbH) mixed with four parts of distilled water, the exposed part of the resist is dissolved.

We spin coated the AZ9260 with two different thicknesses: 9 μm in a one-step process,

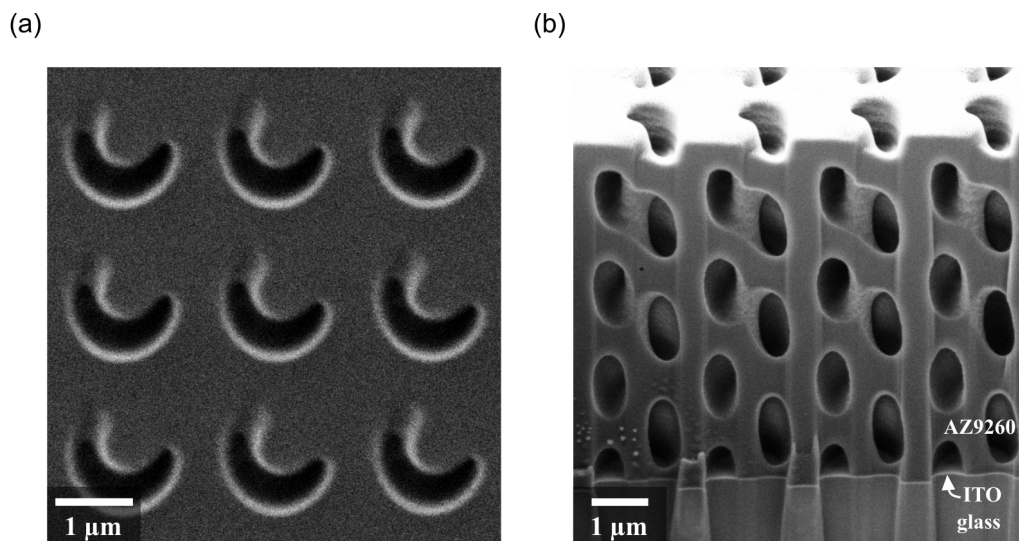


Figure 4.4 AZ9260 templates with helical channels. (a) Top view, and (b) oblique view on a cross-section. The template shown in part (b) was milled open with a FIB. These samples correspond to part (b) of figure 4.1.

and 20 μm in a two-step process. In the one-step process, a drop of the photoresist is spread to a predefined thickness on the substrate using a spin coater. The surplus solvent is evaporated during a baking step using a hot plate. In this step, also water is evaporated from the photoresist. Because water molecules are needed for the chemical reaction during exposition, a rehydration step is necessary. For rehydration, we put a wet tissue and a hygrometer into a transparent and airtight container. When the humidity has arrived at roughly 90%, the tissue is removed and a sample coated with AZ9260 is put inside. To adjust humidity to the desired value, the container can be opened shortly.

In the two-step process, a second photoresist layer is spread on the first layer. Through this and the following baking step, the first layer is strongly affected, leading to a reduction of the template quality in comparison to the one-step process. The optimal process parameters for both processes are given in appendix A.2. Figure 4.4 shows SEM pictures of AZ9260 templates with 9 μm height and arrays of helical channels. The ellipsoidal shape of the holes in figure 4.4 (b) is due to the ellipsoidal shape of the voxel during DLW. There are some points that have to be considered for optimal results:

- The AZ9260 is normally used for ultraviolet, 2D lithography. Depending on the 3D architecture of our template, the length of channels can be much bigger than the film height that has to be developed in 2D templates. In addition, we use the resist with slightly higher resolution than anticipated by the manufacturer. Thus, we use process parameters deviating from the proposed values. In particular, the development time is much longer in order to guarantee a development of the channels down to the substrate.
- The interface finder in the DLW system uses the refractive index contrast between substrate and resist to find the interface of both. As the AZ9260 has a rather small

film thickness of 9 μm , the interface between resist and air is found because it has a much higher refractive index contrast in comparison to the interface between resist and substrate. This can be avoided through an additional layer on top of the AZ9260, *e.g.*, a polydimethylsiloxane plaster can be used.

- The region of energy doses for DLW leading to good results is narrow and depends strongly on the parameters of the preceding process steps and on the humidity of the surrounding air during DLW. Thus, steady process parameters are important in order to obtain good reproducibility.
- During storage after spin coating, the AZ9260 degrades. One reason is that the photoinitiator decomposes at temperatures above 15°C (the AZ9260 supply has to be stored in a refrigerator). Another reason is that the AZ9260 dehydrates if the humidity is not sufficiently high [138]. Thus, we found that for best results, the resist should be exposed and developed within 48 hours after spin coating.
- Although chemically stable in our electrolyte solutions, an AZ9260 photoresist that has dried after ECD should not be dipped into an aqueous solution again. Then, after repeated drying, it often develops cracks or even detaches from the ITO electrode. This is probably due to the strong change of water concentration in the photoresist when it is dipped into an aqueous solution and then dried.

The SU8 Photoresist

The second photoresist that was used within this work is SU8. The use of SU8 for DLW is described in detail in [140]. Thus, we will only summarize it shortly here. It consists of three components: the photoinitiator CYRACURE UVI-6976, the epoxy resin EPON®SU8, and a solvent. During exposure, an acid is separated from the photoinitiator, which initiates a polymerization of the epoxy resin. The polymerization is completed after DLW by an additional baking step. To gain a polymer template, the substrate is developed in the developer solution mr-600 (MicroChem Corp.). It dissolves all photoresist except for the polymerized regions. A table with the used process parameters for a film thickness of 20 μm and 100 μm is given in appendix A.2. The resulting SU8 template is chemically stable in the used electrolyte solutions. Also, repeated dipping into aqueous solutions and drying does not affect the resist.

Wetting of Polymer Templates

An important step is the wetting of the templates with electrolyte solution before ECD. When some channels of an array are not filled with the electrolyte, no material will grow there leading to inhomogeneous arrays of structures or no growth inside the template at all. This is illustrated in figure 4.5 (a) by an AZ9260 template with straight channels which are only partially filled with Au. Figure 4.5 (b) shows a SU8 template which is partially filled with Ni. In contrast, in figure 4.5 (c), a sample is shown where helical channels have been completely filled with Au due to thorough wetting. The composite of AZ9260 and Au was cut open with FIB milling after ECD and corresponds to figure 4.1 (c). We use two different methods for the wetting of templates.

For the first method, the sample, with a drop of electrolyte on the template, is put

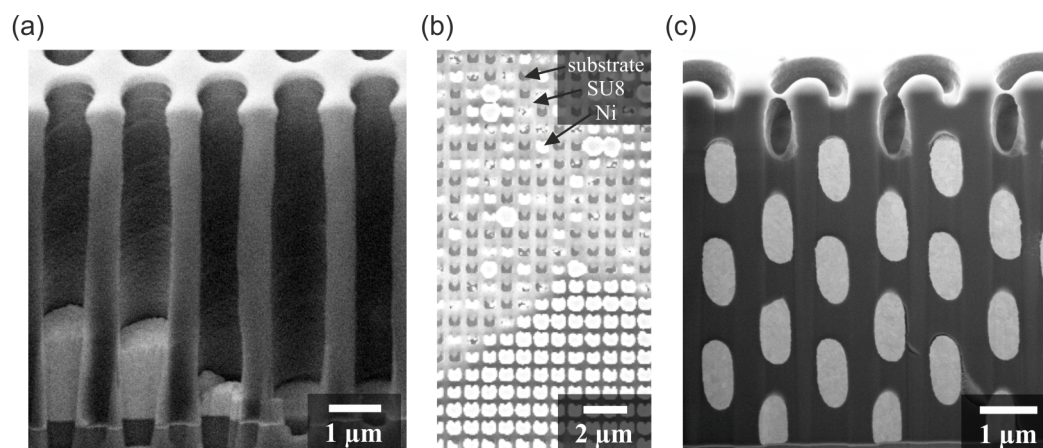


Figure 4.5 Influence of wetting on the homogeneity of arrays. (a) Cross-section of an AZ9260 template with straight channels which were only partially filled with Au, (b) top view on a SU8 template with arrays of u-shaped holes which were partially filled with Ni, and (c) cross-section of an AZ9260 template with helical channels that were completely filled with Au. Figure part (c) corresponds to figure 4.1 (c).

into a desiccator. The pressure is decreased to around 15 mbar¹ with a pump, which leads to an expansion of the air in the template channels until part of it leaves the template. When the pressure returns to its usual value, the air in the channels contracts and the electrolyte is drawn into the channels. After roughly 10 cycles, the wetting of the template is improved considerably. This method is well suited for templates with many interconnected channels [141]. When used for the wetting of templates with helical channels, however, usually some of the channels in these templates will not be filled. The idea of the second method is to replace the air in the template channels by carbon dioxide (CO₂). When an electrolyte drop is put on such a template, it is wetted very thoroughly. This is because CO₂ completely dissolves in water and thus can escape *via* the channels of a template. To use this method, we built a small setup consisting of a vacuum chamber with three ports. Through one port, the substrate can be put into the chamber. In case of AZ9260, we add a wet paper tissue to the substrate to prevent dehydration. Using the second port, the pressure is reduced to 100 mbar with a pump. Then, the chamber is filled with CO₂ (Minican CO₂ 4.5, from Linde AG) through the third port. After 15 min, the process is repeated. Then, an electrolyte drop is put on the template and the sample is built into the ECD setup. This method leads to a very good wetting of various templates and was tested with channel diameters down to 450 nm.

Resist Removal after Electrochemical Deposition

After ECD, we want to remove the polymer templates in order to conduct optical measurements because both used photoresists have absorption bands in the infrared frequency region. The AZ9260 can be dissolved by isopropyl, acetone, and many other

¹Pressures below 5 mbar lead to freezing of the droplet. At low pressures, water is vaporized from the electrolyte droplet, thereby cooling and eventually freezing it.

solvents. Thus, one could simply dip the substrate into acetone. However, then the deposited structures are often ripped off the substrate when the acetone vaporizes due to surface tension. This can be circumvented by using supercritical CO₂ drying [142]. We used the critical point dryer CPD 030 from Leica Camera AG for this process step. The idea is to prevent the vaporization of the solvent. To this end, the substrate is dipped into acetone and put into a pressure chamber. The acetone is replaced by liquid CO₂. Then, the chamber is heated up, thereby increasing the pressure until the CO₂ reaches its supercritical phase. By releasing the pressure, the CO₂ changes into the gas state. However, this method involves some risk as the deposited structures can be detached from the substrate if the process does not work properly.

Another possibility to remove a template is plasma etching in air. Using a high frequent electromagnetic field, a plasma is created from a reactive gas (in our case oxygen). The oxygen ions react with the polymer and ash it. During plasma etching, it is advisable to turn the substrate upside down in a watch glass. By this means, residues of the polymer can fall down instead of staying on the substrate. The plasma etching is done using the plasma etcher PlasmaPrep5 from Gala Instrumente GmbH. This method works well for AZ9260 inverted by metals. SU8 can also be removed by plasma etching. For templates inverted by Cu₂O, plasma etching with oxygen is not suited because it oxidizes the Cu₂O to copper(II) oxide (CuO). In this case, the supercritical CO₂ drying should be used.

4.3. Electrochemical Deposition of Gold

The ECD of Au was used for the fabrication of the helical metamaterials presented in sections 6.1 to 6.3. We will describe the Au electrolyte solution and its basic working principles in the first part of this section. The second part is concerned with the used setup and the ECD of Au films. In the last part, we will discuss issues concerning the inversion of polymer templates and show some studies on the design flexibility of resulting structures.

4.3.1. Composition of the Electrolyte Solution

We chose a sulphite-based aqueous Au electrolyte solution. It is being used and improved since many years for the LIGA process by K. Bade and coworkers (from the Institute of Microstructure Technology, KIT), who supplied us with this electrolyte solution. In [26], 2D Au structures on silicon wafers with lateral structure sizes below 1 μm and structure heights around 10 μm have been realized using the LIGA process.

The electrolyte solution contains the Au complex sodium gold sulfite (Na₃[Au(SO₃)₂]). This component delivers Au⁺ ions, complexed by sulfite as [Au(SO₃)₂]³⁻, to the electrolyte solution. During ECD, the complex is decomposed at the cathode, resulting in an Au⁺ cation and two sulfite anions (SO₃²⁻). The anions can also take part in the cathode reaction, thereby lowering the rate of deposited Au at a certain current flow. This rate was measured to be between 95% and 100% [26] (where 100% means that every charge transfer at the cathode is due to Au deposition). For stabilization and to improve conductivity,

Table 4.1 Components of the Au electrolyte solution and their concentrations.

component	concentration
sodium gold sulfite	25 $\frac{\text{g}}{\text{l}}$
sodium sulfite	30 $\frac{\text{g}}{\text{l}}$
titriplex	30 $\frac{\text{g}}{\text{l}}$
ethylene diamine	22 $\frac{\text{ml}}{\text{l}}$

sodium sulfite (Na_2SO_3) and ethylenediamine tetraacetic acid disodium salt dihydrate (titriplex, $\text{C}_{10}\text{H}_{16}\text{N}_2\text{Na}_2\text{O}_8 \times 2\text{H}_2\text{O}$) are added. The titriplex has the additional function to complex foreign ions and thereby improve the purity of the deposited Au. The next component, ethylene diamine ($\text{C}_2\text{H}_4(\text{NH}_2)_2$), complexes surplus Au^+ ions and stabilizes the electrolyte solution. The leveling and thus the brightness of the deposited Au can be improved through the addition of metals or metalloids like arsenic, thallium, selenium, and lead in a concentration of ppm [26]. All components are dissolved in water. The electrolyte solution has a stable pH of 8.5. The concentration of the components is given in table 4.1.

Once set up, the electrolyte solution is not entirely stable. A high concentration of Au ions can lead to precipitation of Au particles through $3\text{Au}^+ \rightarrow 2\text{Au} + \text{Au}^{3+}$ [143]. These particles are visible as a brown sediment in the transparent, yellowish electrolyte solution. They are nucleation cores for further precipitation of Au. Thus, the solution is stirred constantly, and filtered with a pore size below $0.22 \mu\text{m}$ once a sediment has evolved. One should also keep in mind that the concentration of the Au^+ ions is depleted over time by the ECD. In our case however, the deposited amounts are so small that adjustment of the Au ion concentration is not necessary over periods of years. The volume of the electrolyte solution is kept constant by refilling it with deionized water.

4.3.2. Gold Deposition Process

The electrolyte solution described above does not only allow to deposit high quality Au structures. It also has the advantage that a simple setup can be used for ECD, thereby increasing the reliability of this process step. Our setup is shown in figure 4.6. The electrolyte solution is in a glass beaker that stands on a heating magnetic stirrer (MR Hei-Standard, Heidolph Instruments GmbH & Co.KG). As anode, we use a platinized titanium mesh. It works as a redox electrode because platinum is inert in this electrolyte solution. The main reaction that takes place at the anode is the transformation of sulfite ions to dithionite ions ($\text{S}_2\text{O}_6^{2-}$) and sulfate ions (SO_4^{2-}) [26].

The cathode is our glass substrate with a conducting ITO film and a photoresist template. The substrate can be mounted in different ways that we will describe within the next paragraph. Both electrodes and a thermometer are dipped into the electrolyte solution. The thermometer is coupled to the heating magnetic stirrer, allowing for a temperature stabilization of $\pm 1 \text{ K}$. The electrodes are connected to a constant current source (6221 AC and DC current source, Keithley Instruments GmbH).

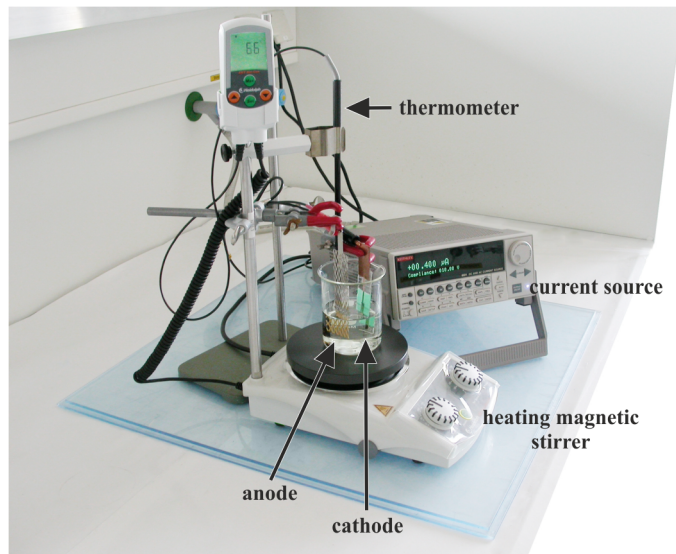


Figure 4.6 Photograph of the used ECD setup.

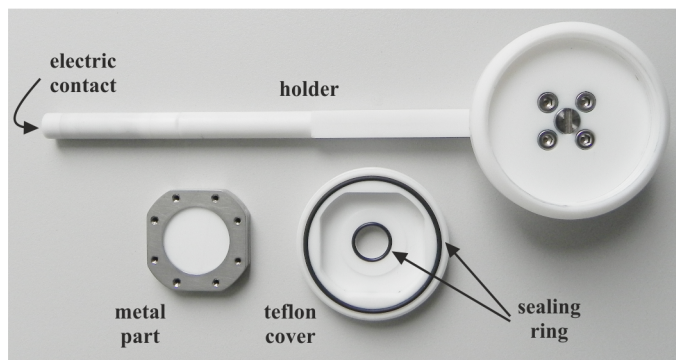


Figure 4.7 Photograph of the components of our custom made sample holder.

The simplest possibility to mount a sample is to put it on a microscope slide. A connection of the ITO to an alligator clip can be made with a conducting tape. To isolate the conducting tape from the electrolyte solution, it is covered with a technical tape that is chemically resistant to components of the electrolyte solution. This kind of sample holder was used in figure 4.6. However, the removal of the conducting tape after ECD can lead to cracks in the photoresist, thereby also destroying the deposited structures. Much better results are achieved by using a custom made teflon sample holder. It is shown in figure 4.7. It has an inner metal part that holds the substrate and makes an electric contact to the ITO layer. This part is flipped and put into a round teflon cover. Both parts are then flipped and mounted in the holder. It is mainly made of teflon and isolates the metallic parts electrically from the electrolyte solution. Sealing rings in the teflon cover make sure that no electrolyte solution can get into the holder. Only a small part of the substrate is exposed to the electrolyte solution by a hole in the teflon cover. The holder also provides an electrical connection at the end of the teflon rod.

Table 4.2 Optimal parameters for the ECD of Au.

parameter	value
current density	$3 \frac{\text{mA}}{\text{cm}^2} = 3 \cdot 10^{-5} \frac{\mu\text{A}}{\mu\text{m}^2}$
temperature	57°C
stirrer velocity	375 $\frac{1}{\text{min}}$

Once a sample is inside the electrolyte solution, we wait for 15 min before ECD because stress in deposited films is reduced when the electrolyte solution and the cathode have equal temperature. In order to achieve qualitatively good and reproducible results, the current density, the temperature, and the velocity of the magnetic stirrer have to be controlled during ECD. The optimal parameters for our process are summarized in table 4.2.

For the ECD of Au, a constant current is used. The applied voltage depends on the potentials of both electrodes and on the ohmic resistance of the ITO electrode. When the current is switched on, Au is deposited on the ITO film at the cathode, thereby changing its potential and hence the applied voltage. During the inversion of polymer templates, the voltage can also vary due to a change of concentration overpotentials. Thus it is favorable to control the current. It is calculated from the above current density and depends on the cathode area. A constant current has also the advantage of a homogeneous deposit because the rate of deposited Au atoms per area is constant at all deposit heights given that the cathode area is constant.

We measured the potential of an ITO cathode without a photoresist template using a reference electrode and a potentiostat that will be described in more detail in section 4.5. The potential was measured under deposition conditions, *i.e.* with the temperature and stirrer velocity given in table 4.2. Without an applied current, we measured potentials around 72 mV. During ECD with the above given current density, the potentials were around -740 mV.

As we could not find literature on the deposition of Au films or thick structures on ITO, we want to describe the growth of our Au films. The formation of Au on ITO electrodes is depicted in figure 4.8 (a) – (c). A closed film is formed after 3 – 4 min. Then, the thickness of the deposited film after a certain time is given by the deposition rate which is roughly $200 \frac{\text{nm}}{\text{min}}$ in our case. Figure 4.8 (d) and (e) shows an Au film with a very fine surface. The fine, polycrystalline structure of the deposit is visible in figure 4.8 (f), where the film was cut open with a FIB. We measured the macroscopic distribution of the film thickness on several samples and found a random thickness variation of around $\pm 12\%$. This rather high value [26] is probably due to the high ohmic resistance of the ITO.

With our usual ECD parameters, the Au films peel off the ITO substrate after about 5 – 10 min. The main reason may be that Au is a noble metal and has a low reactivity. As it is not polar, it adheres poorly to the polar ITO. Stress might also play a role, although the used electrolyte solution leads to deposits with low stress [26]. This is indicated by the fact that the peeling off does only occur for macroscopic films while our structures do adhere very well as we will see in the next part of this section. We tried

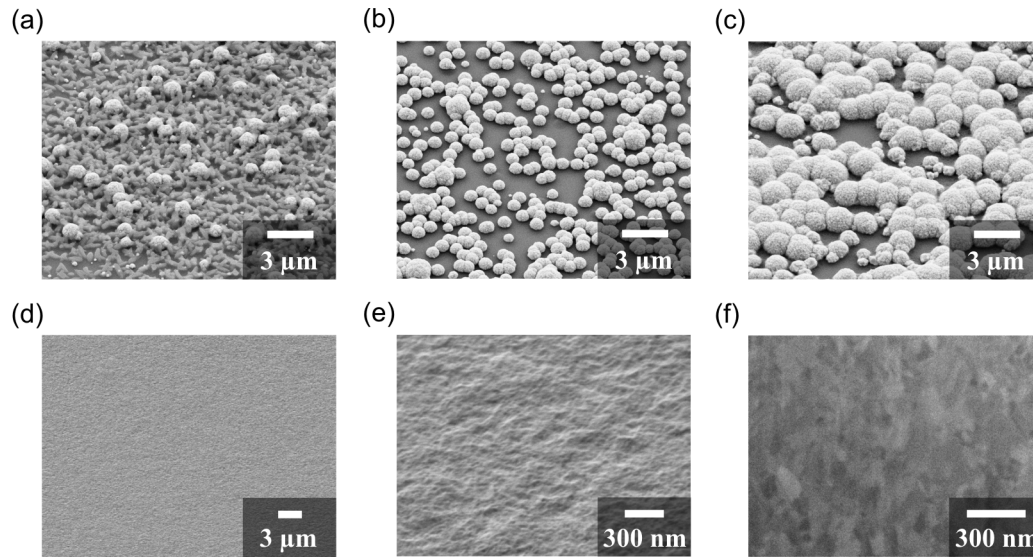


Figure 4.8 The upper row shows oblique views of Au deposits (bright) on ITO (dark) after (a) 15 s, (b) 60 s, and (c) 150 s. The grayish, lengthy structures in (a) are residues of the electrolyte solution. Figure parts (d) and (e) show an oblique view on the surface of a thick Au deposit with different magnifications. The cross-section of the same Au deposit after FIB milling is shown in part (f). There, a contrast results due to different crystal orientations of the polycrystalline Au.

different methods to increase the adhesion of Au films. An increase in the deposition time without peel off was found for: temperature gradients during deposition, current densities of $4.5 \frac{\text{mA}}{\text{cm}^2}$ or higher, pretreatment of the ITO with 3-mercaptopropyltrimethoxysilane, and higher thicknesses of the ITO. The best results with deposition times over one hour without peeling off were achieved with an ITO thickness of 100 nm. This might be due to mechanical anchoring of the Au film at the ITO surface that is becoming rougher with increasing thickness.

The quality of the Au deposit was checked with energy dispersive x-ray spectroscopy [144]. We found that the purity of the deposits is above 94.5%. This matches with the rate of deposited Au for a certain current flow of 95 – 100% as given above.

4.3.3. Inversion of Nanostructured Templates with Gold

We mainly use the AZ9260 for the inversion of nanostructured templates with Au. It is removed at the borders of the substrate with acetone to provide electrical contact to the ITO. As the borders are isolated from the electrolyte solution by the sample holder, Au is only deposited inside the template channels and no macroscopic film evolves. This leads to very small cathode areas. A single channel has a cathode area on the order of $0.25 - 1 \mu\text{m}^2$, depending on the energy dose during DLW and the structure design. Adding up all channels within one array and all arrays on one sample, we typically have cathode areas of $1000 - 30,000 \mu\text{m}^2$. With the fixed current density of $3 \cdot 10^{-5} \frac{\mu\text{A}}{\mu\text{m}^2}$,

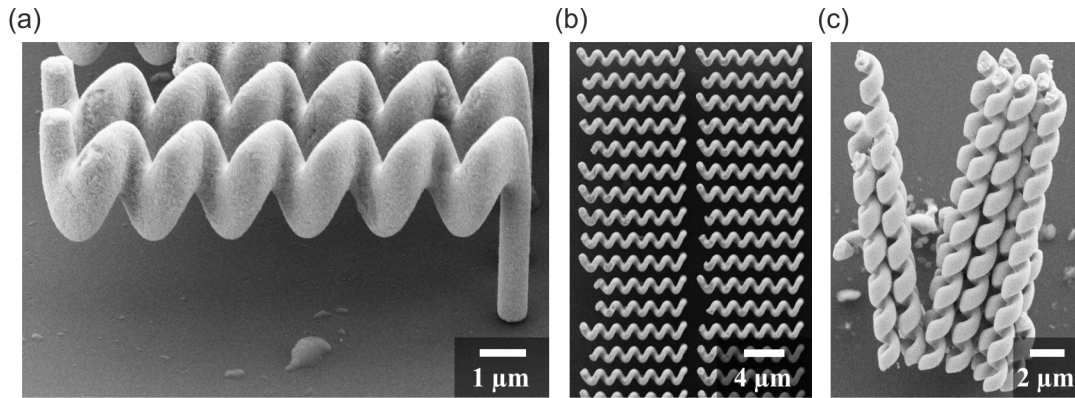


Figure 4.9 (a) Oblique view of an array of Au helices with six pitches length. The helix axes are parallel to the substrate. (b) Top view of the helices shown in (a). (c) Oblique view on an array of Au helices with nine pitches length. The helix axes were perpendicular to the substrate before the helices stuck together after being detached from the substrate.

current values usually lie between $0.03 \mu\text{A}$ and $0.9 \mu\text{A}$. In order to ensure a constant current value during ECD, we chose the above mentioned current source which has very low noise at these current levels.

To deposit only within template channels proved to be advantageous. As mentioned in section 3.4, the deposition rate inside small channels is different to the deposition rate on the open electrode, which is solved if material is deposited only inside the channels. More importantly, in contrast to macroscopic films, no peeling off occurs for nano- and microstructures and thus an ITO film thickness of 22 nm can be used (which is more transparent than a 100 nm thick film). The surface areas of single Au structures are too small in comparison to the structure height to build up considerable stress. In addition, attractive forces at the interface to the ITO layer have much more influence on nano- and microstructures than on macroscopic films, leading to better adhesion. This is clearly demonstrated by long Au helices with helix axes parallel to the substrate, which we fabricated. They are fixed to the substrate through rods that are attached to one end of the helices as can be seen in figure 4.9 (a) and (b) for helices with roughly six pitches length.

If Au structures are detached from the substrate, for example through cracks in the photoresist before its removal, they tend to stick to each other. This can be seen in figure 4.9 (c). It shows helices with nine pitches and a height of $18 \mu\text{m}$ that were fabricated using the two-step process for AZ9260. They had their helix axes perpendicular to the substrate before being detached from the substrate and sticking together. Please also note that the wire thickness merely changes throughout the entire structure length.

Through thorough wetting, a good homogeneity of arrays can be achieved in the sense that all channels are filled. But we also are interested in the height variation of structures within one array. The longer the filled channels are, the harder it is to achieve

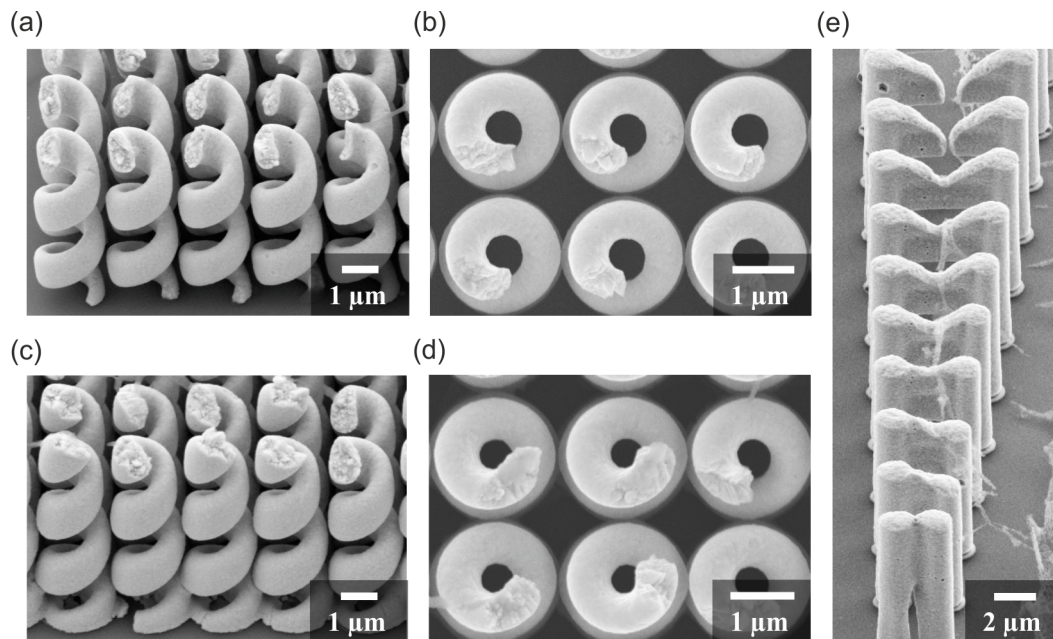


Figure 4.10 (a) Oblique view, and (b) top view of an array of helices with axes perpendicular to the substrate. (c) Oblique view, and (d) top view of an array of helices on the same substrate as (a) and (b), but with a bigger wire diameter due to a higher energy dose during DLW. (e) Inversion of horizontal bars between vertical channels with increasing distance of the bars.

homogeneous heights. For example, the number of pitches in the array in figure 4.9 (b) varies between 5.2 and 6.5.

In order to get good homogeneity of the height, good structure quality, and the desired height, it is crucial to use the above given current density. Thus, the value of the cathode area should be known. To this end, one can fabricate two samples with equal DLW parameters. For one, the current is calculated with an estimated cathode area. After ECD for a certain time and measurement of the resulting structure height, one can calculate the deposition rate. By comparison to the deposition rate of $200 \frac{\text{nm}}{\text{min}}$ at the optimal current density, the cathode area can be calculated. With this value, the second sample is fabricated, usually leading to much better results.

We explained in section 3.4, that the deposition rate in channels depends on the diffusion of ions through the channels and on the local density of field lines. For increasing channel diameter, the first effect tends to accelerate growth while the second effect tends to slow it down. Figure 4.10 (a) – (b) and (c) – (d) shows two helical metamaterial arrays. The arrays were written with different DLW energy doses on one substrate. We see that the structure height increases with increasing wire diameter. This indicates that the diffusion effect is dominant in our case.

In figure 4.10 (a) and (c), we can also see that the ends of the Au helices are not parallel

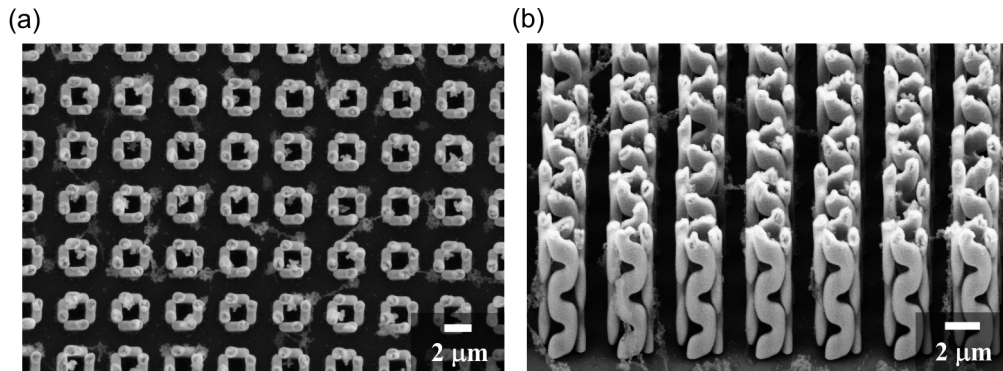


Figure 4.11 Au structures with very small mutual distances. (a) Top view, and (b) oblique view [40].

to the substrate as one might assume. This can be explained by the diffusion controlled growth inside the template channels. It means that an equal amount of material arrives everywhere at the surface because the diffusion inside the channels is linear. Assuming that all arriving ions are deposited, the volume of edges will be filled faster because it is smaller. In addition, leveling effects can lead to a faster filling of the edges.

This continues until the surface inside the channel is approximately normal to the channel direction. In the case of helical channels, it is normal to the helix line. This means that the length of the helix trajectory should be used as the desired thickness when calculating the deposition time for helices.

Figure 4.10 (e) shows that channels can only be filled if they are both connected to the cathode as well as to the electrolyte. We wrote the letter “H” into the AZ9260 and increased the length of the horizontal bar. We see spherical growth into this bar until the connection to the electrolyte and thus to the supply of new Au^+ ions is cut by the deposited Au.

We mentioned that detached Au structures tend to stick to each other. This poses the question whether structures are detached from the glass substrate if they are standing very close together, thereby imposing a limit on how close to each other structures can be fabricated. The unit cells of the arrays in figure 4.11 consist of four structures. Although they are close to each other and have a small footprint, the structures stand upright on the substrate. These arrays were fabricated in cooperation with M. Rill [40]. The design was proposed in [51] for the realization of 2D isotropic metamaterials with a negative refractive index.

If all process parameters are chosen correctly, homogeneous arrays with equal height of the single structures result. A helical metamaterial with good quality and homogeneity is shown in figure 4.12. It consists of an array of 20×20 helices with a height of 1.5 pitches.

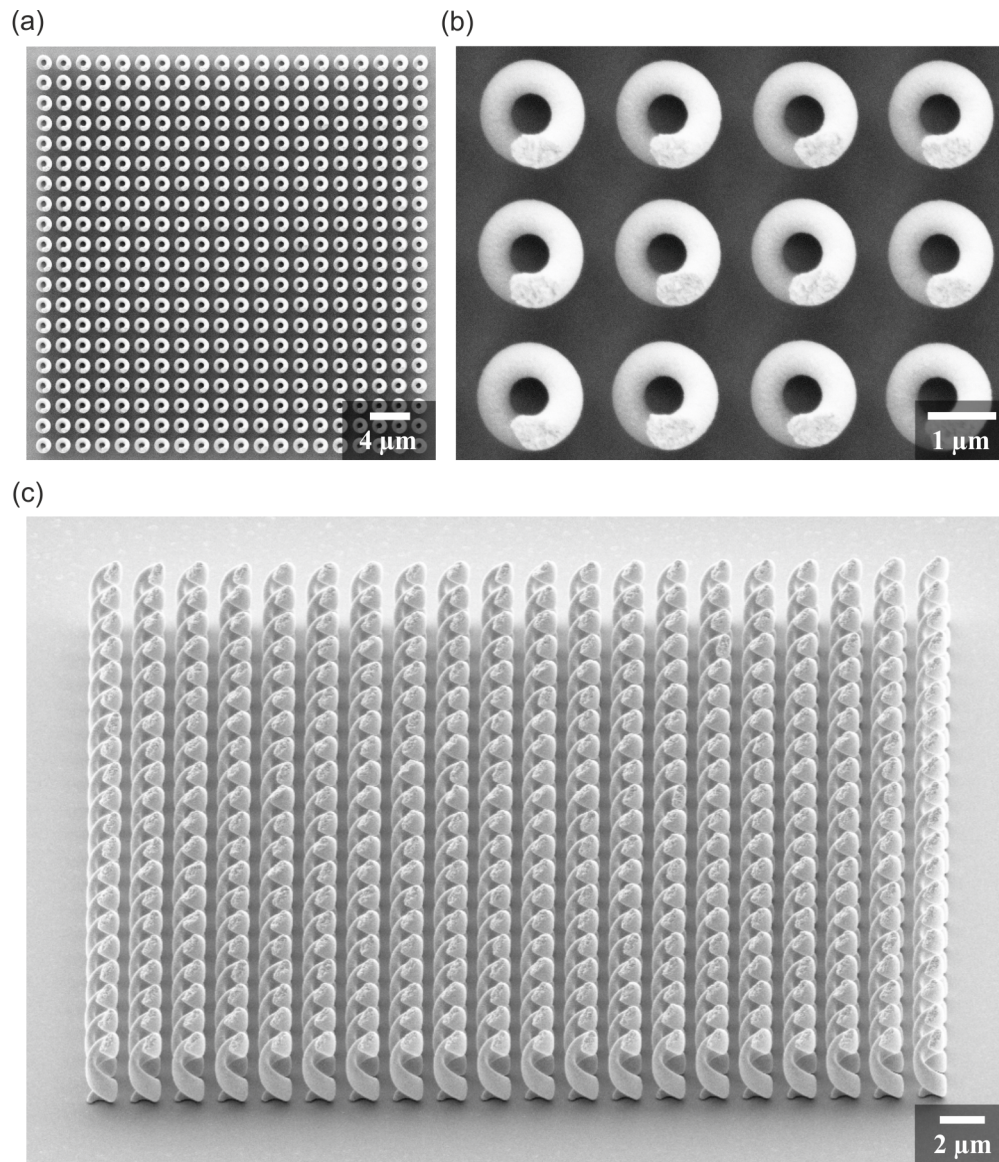


Figure 4.12 Array of helices with axes perpendicular to the substrate. (a) Top view, (b) a close-up of (a) reveals the structure quality, and (c) oblique view of the whole array of 20×20 structures.

Table 4.3 Concentrations of the components of the Ni crystal mixture and the brightener.

component	concentration
nickel sulfite hexahydrate	70 – 80%
nickel chloride hexahydrate	10 – 20%
boric acid	9 – 13%
saccharin	≤ 12%

4.4. Electrochemical Deposition of Nickel

The composition of the electrolyte solution for the ECD of Ni will be described in the beginning of this section. Then, the parameters for optimal deposition on ITO will be given. In contrast to Au, we found that our Ni films do not peel off the substrate within typical deposition times. This is probably due to the higher reactivity of Ni. Thus, we focused on the inversion of SU8 templates standing on a macroscopic ITO electrode, which will be described in the last part.

Composition of the Electrolyte Solution

The use of Ni for the inversion of photonic crystals [145, 146] has been reported in [106, 141]. Inspired by the results, we chose the electrolyte solution used in [141]. It is a commercially available nickel sulfate based electrolyte (Bright Nickel, Caswell Europe). The electrolyte solution contains nickel sulfite hexahydrate² ($\text{NiSO}_4 \cdot 6\text{H}_2\text{O}$). The nickel sulfite hexahydrate delivers the main part of Ni^{2+} cations for the ECD. The next component is nickel chloride hexahydrate ($\text{NiCl}_2 \cdot 6\text{H}_2\text{O}$). In contrast to the Au electrolyte, the Ni electrolyte is used with a Ni anode which is dissolved during the ECD. The nickel chloride hexahydrate plays an important role as an oxidizer: It accepts electrons at the anode and thus helps to produce new Ni^{2+} ions. It also delivers additional Ni^{2+} ions for the deposition and improves the conductivity of the electrolyte solution. The electrolyte solution also contains boric acid (H_3BO_3). It buffers the pH value of the electrolyte solution to 3.5 – 4.5. This is important at the cathode, where the pH value can increase when high currents are present. For pH values above 6, nickel hydroxide would be precipitated and deposited together with hydrogen at the cathode, leading to rough and dark deposits. The last component of the electrolyte solution is a brightener, mainly containing water and saccharin.

The electrolyte is delivered as a Ni crystal mixture and a separate brightener. The concentration of the components in the Ni crystal mixture and of the saccharin in the brightener is revealed only approximately by the supplier and given in table 4.3.

To make the electrolyte solution, 83.33 g of the Ni crystal mixture are dissolved in 250 ml water at 70°C. Then the solution is cooled to 30°C and 12.6 g of the temperature sensitive brightener are added. Once set up, the pH value of the electrolyte solution should be checked each month. We conducted pH measurements using pH test strips or an electronic pH measurement device (pH340 and SenTix®41, WTW GmbH). The

²Hydrates are solid crystals containing water molecules that are built into the crystal lattice. In our case, six water molecules are built in per each nickel sulfite molecule.

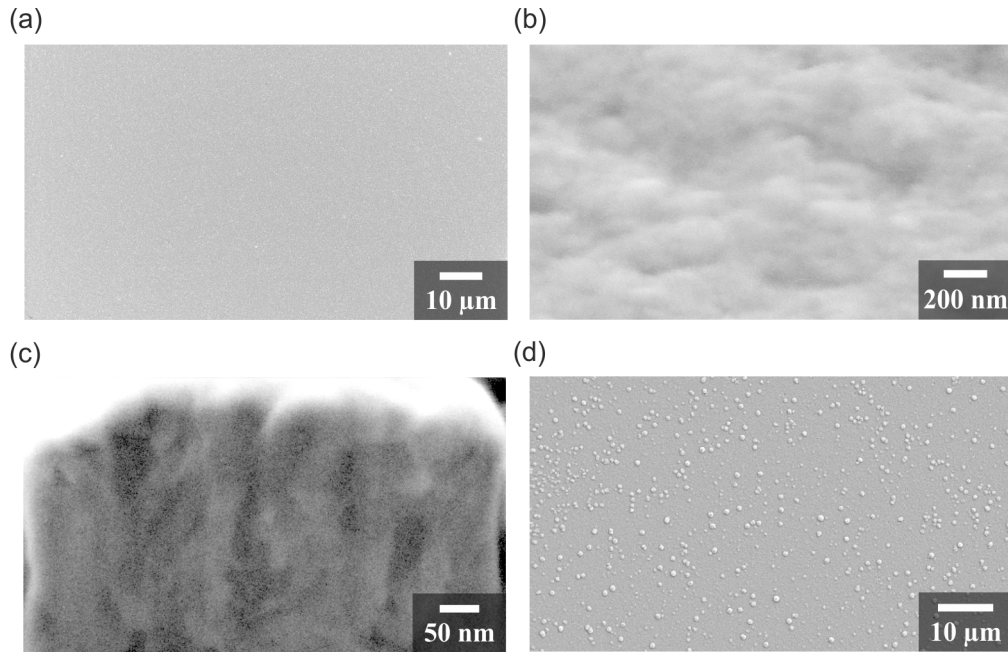


Figure 4.13 SEM pictures of Ni films. (a) Top view of the surface of a film with high quality, and (b) oblique view of the same surface with larger magnification. (c) A FIB cut through a Ni film shows a fine polycrystalline structure. (d) SEM picture of a Ni film with low quality. The magnification is the same as in (a).

check of the pH value is necessary because less ions can be transferred at the cathode than at the anode which leads to an increase of the hydrogen ion concentration and thus of the pH value at the anode. To correct the pH value, sulphuric acid solution with a concentration of 25% is added in portions of 0.15 ml. A constant or decreasing pH value would hint on problems at the anode like a bad electrical contact or a too small anode area.

Nickel Deposition Process

Ni can be deposited with a setup similar to the one described for Au. It is merely extended by the possibility to measure or adjust the applied voltage. In addition, the platinized titanium anode is replaced by a Ni anode. We conducted different parameter variations and will discuss the influence of the different parameters now.

The pH value can lie between 3.5 and 4.5, however the use of a constant value improves reproducibility. The quality of the Ni films can be increased by using a low temperature. Although this leads to smaller deposition rates, they are still sufficient for our purposes. The adhesion of the Ni films to the substrate can be improved by fast stirring and by the usage of small ITO electrodes as the stress is reduced with the cathode area. A reduction of the electrode area by 50% leads to a significant increase in deposition time until peel off occurs. As we mentioned in the beginning, the voltage needs to be controlled for the ECD of Ni in our case. This is due to the high ohmic resistance of the ITO. In order to achieve a good covering of the whole cathode, a high voltage is needed in the beginning. After a thin film has covered the cathode, a desired current can be adjusted.

Table 4.4 Optimal parameters for the ECD of Ni.

parameter	value
pH	3.8
temperature	35°C
stirrer velocity	900 $\frac{1}{\text{min}}$
cathode area	35 – 55 mm ²
voltage until whole cathode is covered	1.5 V
current density	0.025 – 0.1 $\frac{\text{mA}}{\text{mm}^2}$

The current needs to be controlled because too high deposition rates lead to a rough deposit. Also, the homogeneity of the deposits can be improved by using low currents. However, good results can be achieved within a broad region of current densities. The optimal parameters for the deposition of Ni films on ITO electrodes are given in table 4.4. Without the use of optimized parameters, deposited films were rough and peeled off the ITO electrode after several minutes. Using these parameters, we measured a deposition rate of 164 $\frac{\text{nm}}{\text{min}}$ for a current density of 0.097 $\frac{\text{mA}}{\text{mm}^2}$. Figure 4.13 (a) – (c) shows Ni films with good quality. As a comparison, a film with low quality is displayed in figure 4.13 (d) with the same magnification as was used for figure 4.13 (a).

Inversion of Nanostructured Templates with Nickel

The inversion of SU8 templates was established with Ni due to its better adhesion on the ITO electrodes. We will show SEM micrographs of some of the fabricated structures now. Figure 4.14 (a) and (b) shows FIB cuts of a so called woodpile structure [147] which was inverted with Ni. In figure 4.14 (a), rods oriented perpendicular to the cutting plane are visible. The cut in figure 4.14 (b) goes through rods which are parallel to the cutting plane. Figure 4.14 (c) shows an oblique view on a Ni film with u-shaped holes. They result from the inversion of u-shaped SU8 structures (which were written by M. Thiel) that were removed after ECD. In the lower left corner, part of the the film was cut open with a FIB to reveal the interior of the structure. Pillars that result from the inversion of a SU8 grating are shown in figure 4.14 (d).

4.5. Electrochemical Deposition of Copper(I) Oxide and Copper

Through the ECD of Cu₂O in combination with the ECD of a metal, electrically disconnected metamaterial structures normal to the substrate could be made. The work presented in this section was done together with M. Latzel within his diploma thesis. We will describe the composition of the used electrolyte solution, the used setup, and the deposition parameters. We will show deposited Cu₂O films and helices resulting from the inversion of AZ9260 templates. In the last part, we will shortly explain how Cu can be deposited from the same electrolyte solution and show resulting structures.

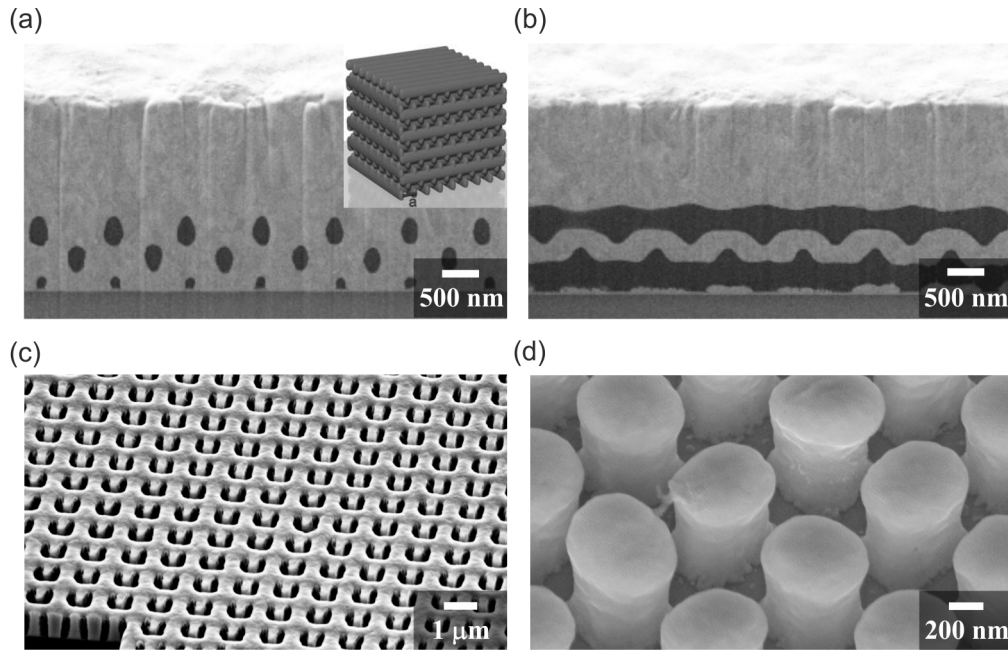


Figure 4.14 Fabricated Ni structures. (a) FIB cut through an inverted woodpile structure, the inset is taken from [140] and depicts a woodpile geometry. (b) FIB cut through the same structure as shown in (a), however further into the structure. (c) Oblique view on a Ni film with u-shaped holes, and (d) oblique view on Ni pillars.

Table 4.5 Components of the copper sulfate electrolyte solution and their concentrations.

component	concentration
copper sulfate	$0.4 \frac{\text{mol}}{\text{l}}$
lactic acid	$3 \frac{\text{mol}}{\text{l}}$
sodium hydroxide	until pH = 9

Composition of the Electrolyte Solution

We use a cupric sulfate based electrolyte solution. Such solutions have already been used for the deposition of Cu_2O films on ITO substrates [148–150] and for the inversion of photonic crystal templates [151]. The deposition of thin Cu_2O - Cu layers was reported in [152].

We chose the composition reported in [149]. It contains copper sulfate (CuSO_4) which delivers the Cu^{2+} ions for the ECD. The next component is lactic acid ($\text{C}_3\text{H}_6\text{O}_3$). In an aqueous solution, it produces the lactate ion ($\text{CH}_3\text{CH}(\text{OH})\text{COO}^-$). Two lactate ions complex a Cu^{2+} ion and thereby stabilize it. Otherwise, it would react with hydroxide ions (OH^-) and precipitate as copper hydroxide ($\text{Cu}(\text{OH})_2$). The third component is sodium hydroxide (NaOH) which is used to adjust the pH value of the electrolyte solution to 9. Sodium hydroxide and lactic acid constitute a buffer which stabilizes the pH value. The concentrations of the components are given in table 4.5.

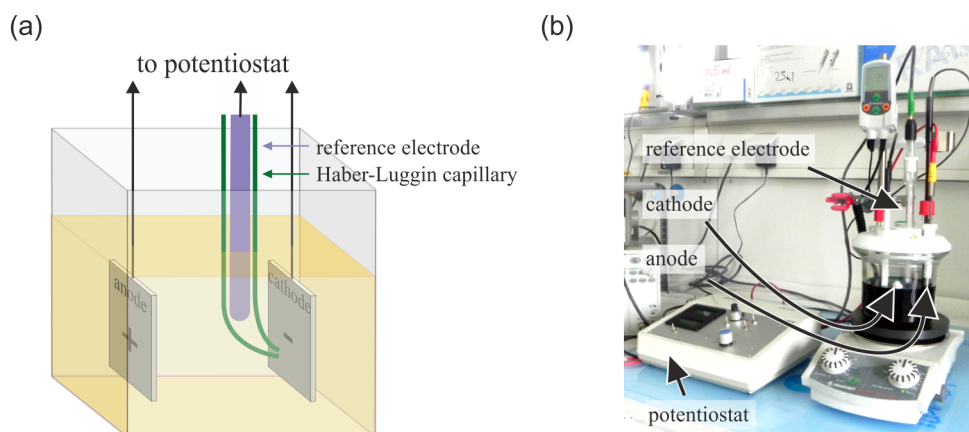


Figure 4.15 ECD of Cu_2O . (a) Schematic of the three used electrodes, and (b) photograph of the used setup. In contrast to the schematic, the real electrolyte solution has a dark blue color.

The electrolyte solution is set up by dissolving 25.53 g copper sulfate ($\geq 99.9\%$, Carl Roth GmbH + Co. KG) and 120.11 g lactic acid (DL-Milchsäure, Carl Roth GmbH + Co. KG) in 250 ml deionized water while constantly stirring. Then, the volume is increased to 400 ml by adding water. In the next step, the pH value is adjusted by adding sodium hydroxide ($\geq 99\%$, Merck KGaA). Only small amounts should be added at a time because the solution heats up due to solvation energy. When the value has arrived at 8.5, it can be adjusted precisely by using caustic soda solution (sodium hydroxide dissolved in water) with a concentration of $5 \frac{\text{mol}}{\text{l}}$. The pH value should be checked every week and adjusted with caustic soda solution or lactic acid if necessary. Despite the lactic acid, copper hydroxide does precipitate in small amounts over time. To minimize the precipitation, the electrolyte solution is stirred continuously.

Copper(I) Oxide and Copper Deposition Processes

In contrast to Au and Ni, Cu_2O is deposited with the use of a reference electrode (SE11, Sensortechnik Meinsberg GmbH) and a potentiostat (ScholarE, Bank Elektronik GmbH). This is because the cathode potential needs to be within a certain range in order to deposit Cu_2O . The ITO electrode is used as cathode and a platinized titanium rod as anode. Like for Au, the inert anode leads to a depletion of Cu^{2+} ions during deposition which is negligibly small in our case. All electrodes are connected to a potentiostat.

A schematic of the electrodes is shown in figure 4.15 (a). The reference electrode is a silver / silver chloride electrode with a constant potential of 197.6 mV against a hydrogen electrode [96]. The potential of the cathode will be given relative to the reference electrode. To prevent current flow between the electrodes, the input of the reference electrode at the potentiostat has a high ohmic resistance. The cathode potential is measured with the potentiostat and adjusted by changing the voltage between cathode and anode. Due to the resistance of the electrolyte solution, a voltage drop occurs between cathode and anode that falsifies the potential measurement with the reference electrode. To minimize this effect, the reference electrode is in a Haber-Luggin capillary. It allows to measure the

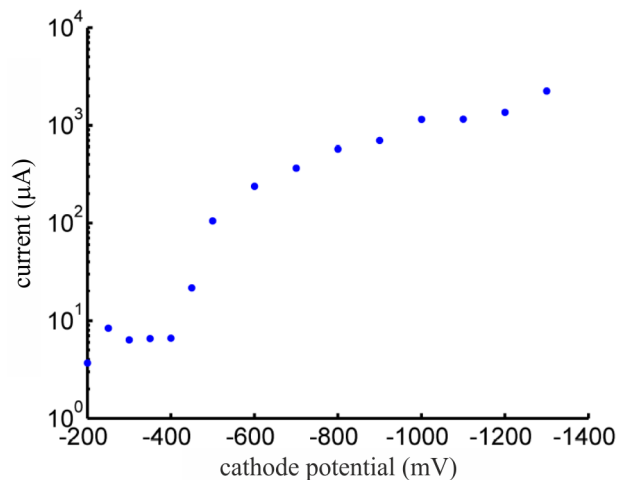
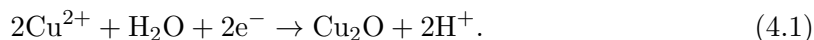


Figure 4.16 Dependence of the current (measured after 5 min deposition time) on the cathode potential that was applied during this time.

voltage between both electrodes with minimal disturbances by the voltage drop in the electrolyte solution. The remaining setup is analogous to the setup used for ECD of Au. Figure 4.15 (b) shows a photograph of the setup.

The control of the cathode potential is important because, depending on it, either Cu_2O , Cu, or a mixture of both is deposited. Cu_2O is deposited according to



For a higher potential, Cu is deposited, too:



The first reaction is slower than the second because more reactants are involved. For sufficiently high potentials, the first reaction can be neglected and only Cu is deposited. In order to determine the transition between the two reactions, films were grown on ITO electrodes with equal areas using different, but constant potentials. The measured current after 5 min deposition time is shown in figure 4.16. Cu_2O is grown for potentials between -200 mV and -400 mV. The current is very low as Cu_2O is a semiconductor. Together with the electrolyte, a kind of Schottky diode in reverse-biasing mode results. At around -400 mV, the deposition of Cu starts and the current increases strongly. This corresponds to a diode in breakdown mode. According to [149], the Cu_2O deposition stops below -956 mV. In our case, a potential of -1300 mV leads to the growth of bright Cu films. Like in the case of Au, the Cu films do easily peel off the substrate.

Besides the cathode potential, the temperature is another important parameter. For a temperature of 60°C , the AZ9260 is dissolved by the electrolyte solution, while low temperatures of 20°C yield bad quality of the deposits. For reproducible results, also the pH value and the stirrer velocity need to be controlled. The optimal parameters for ECD of Cu_2O and Cu are given in table 4.6.

Table 4.6 Optimal parameters for the ECD of Cu₂O and Cu.

parameter	value
pH	9
temperature	40°C
stirrer velocity	500 $\frac{1}{\text{min}}$
cathode potential for Cu ₂ O	-300 mV
cathode potential for Cu	-1300 mV

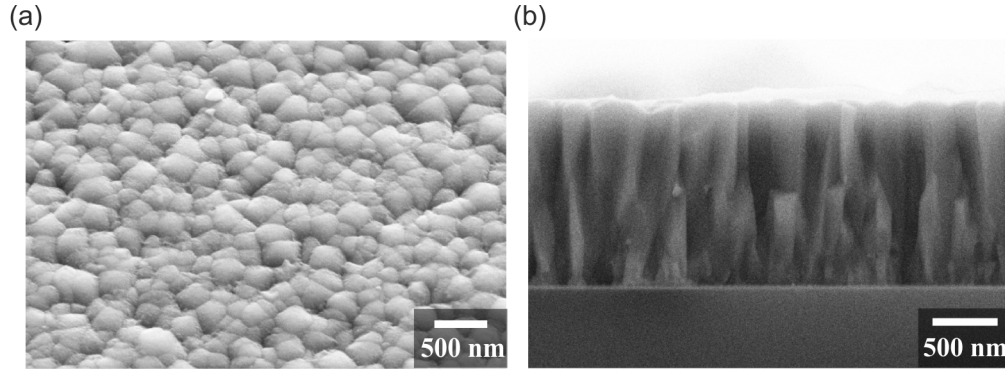


Figure 4.17 Fabricated Cu₂O films. (a) Oblique view, and (b) the cross-section of a substrate after deliberately breaking it shows a lamellar structure of the Cu₂O.

Figure 4.17 (a) shows an oblique view on the surface of a deposited Cu₂O film. After deliberately breaking the substrate, a cross-section of the film reveals a lamellar structure (figure 4.17 (b)). This is probably due to the low deposition rate: Adsorbed Cu₂O molecules have enough time to diffuse to existing nuclei and thus to continue their growth normal to the substrate.

The quality of Cu₂O films was checked in several ways. A transmittance spectrum taken with the setup described in section 5.1 is shown in figure 4.18 (a). It exhibits a strong decrease of the transmittance below 600 nm which is in agreement with the electronic band gap of Cu₂O of 2.1 eV (according to 590 nm) [149].

The spectrum shown in figure 4.18 (b) is the result of an investigation using X-Ray diffraction spectroscopy. Two peaks (at 42.7° and at 92.9° are visible. For comparison, also literature values [153] of Cu₂O and Cu are displayed. Within the measurement accuracy, the data confirm that Cu₂O has been deposited.

Inversion of Nanostructured Templates with Copper(I) Oxide and Copper

The used process for the inversion of AZ9260 templates with Cu₂O is the same as described for Au. However, the deposition rate is not constant over time because the voltage is controlled. Hence, the current adjusts depending on the ohmic resistance. In figure 4.19 (a), the length l of Cu₂O structures on three samples after different deposition times t is shown. The data can be fitted by a function $l(t) = v \cdot t^w$ with the fit parameters $v = 0.76 \frac{\mu\text{m}}{\text{h}^w}$ and $w = 0.79$. Fabricated Cu₂O helices with one pitch height are depicted in figure 4.19 (b).

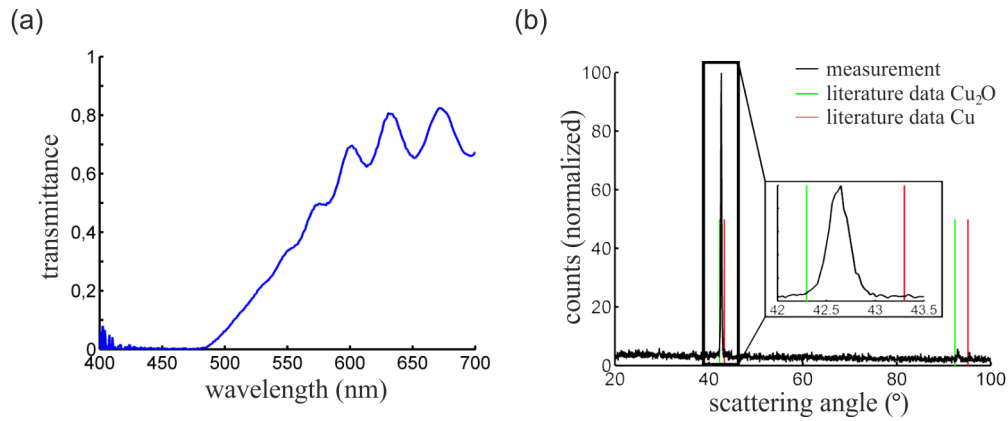


Figure 4.18 Characterization of Cu_2O films. (a) Transmission spectrum of a Cu_2O film, and (b) spectrum resulting from an X-ray scattering measurement in comparison to literature values [153] of Cu_2O and Cu.

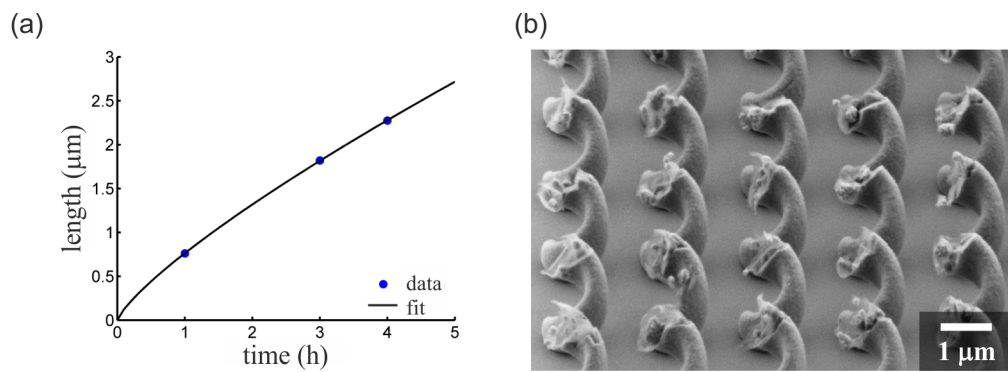


Figure 4.19 Template inversion with Cu_2O . (a) Length of deposited Cu_2O structures on three samples after different deposition times and a fit to the data. (b) Cu_2O helices with helix axis parallel to the substrate and one pitch height.

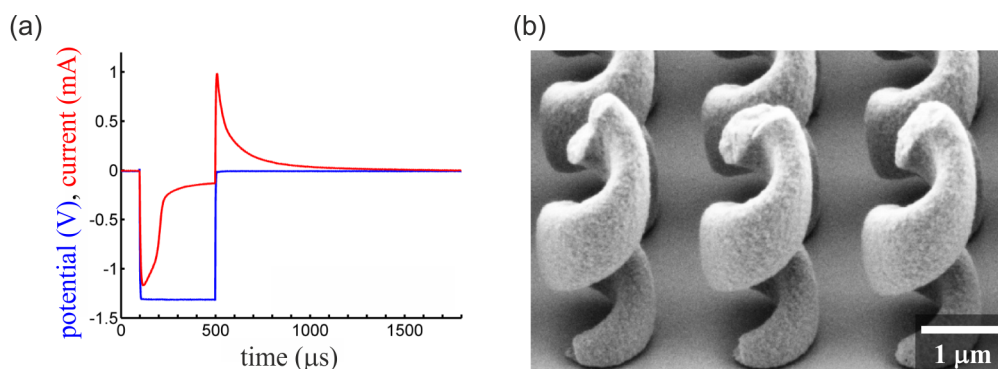


Figure 4.20 Template inversion with Cu. (a) Time dependence of the current during the application of one pulse of the potential. (b) Cu helices with 1.5 pitches height.

In contrast to Cu_2O , Cu is deposited with a high current as can be seen in figure 4.16. Thus, the initial deposition rate is higher than the diffusion rate and the Cu^{2+} ion concentration at the cathode is depleted. Then other reactions take place and lead to bad quality of the resulting structures. Hence, a deposition of Cu with a constant voltage was not possible. This was solved by pulsed ECD. We extended the setup by a function generator (Hewlett-Packard GmbH, HP33120A). It is used as a voltage input to the potentiostat and controls the pulsed voltage applied between anode and cathode. Also, an oscilloscope (Agilent Technologies GmbH, 54642A) was added for measurement of the voltage and the current.

As explained in section 3.4, the pulse duration cannot be chosen arbitrarily short. This is due to the build-up of the electrochemical double-layer. Like for a plate capacitor, the loading time depends on the capacitor area. Thus, the minimal pulse duration varies depending on the area of the template channels at the cathode. The recovery time between pulses should be sufficiently long so that the Cu ion concentration can return to its usual value. We found that a pulse duration of $400 \mu\text{s}$ in combination with a recovery time of $1600 \mu\text{s}$ leads to very good results. The applied potential and measured current are plotted over time in figure 4.20 (a). The high current and exponential decay at the beginning of the pulse are due to the development of the electrochemical double-layer. At around $100 \mu\text{s}$, a kink in the curve indicates the onset of Cu deposition. When the potential pulse ends, the current peaks in the opposite direction because of the double-layer. No material is deposited or dissolved during this time.

The deposition rate is constant as the process is not limited by diffusion. We measured a deposition rate of $760 \frac{\mu\text{m}}{\text{min}}$. However, this might change if the build-up time of the double-layer changes because then the effective deposition time is changed. Figure 4.20 (b) shows Cu helices with 1.5 pitches height and a good structure quality that is comparable to that of Au helices.

5. Characterization and Modeling Techniques

In the last chapter we have described how 3D nano- and microstructures made from Au, Ni, Cu₂O, and Cu can be fabricated by using DLW and ECD. A part of these structures were arrays of Au helices, *i.e.* Au helical metamaterials. Once a helical metamaterial is made, we want to study its optical properties. This is done experimentally with an optical characterization method that will be described in the first section of this chapter. In order to confirm our measurements and to learn more about the optical properties of our structures, we also conducted numerical calculations. The used numerical method will be presented in the second section.

5.1. Optical Characterization Setup

The arrays of helices that we showed in the last chapter typically have lateral lattice constants of $a = 2 \mu\text{m}$. In section 2.1.5, we argued that such arrays can be seen as a metamaterial if the condition $\lambda/(n_{\text{sub}} \cdot a) > 1$ is satisfied. With a refractive index of the glass substrate $n_{\text{sub}} = 1.5$, this means that we can treat these arrays as metamaterials for infrared frequencies. In the case of $a = 2 \mu\text{m}$, these are frequencies below 100 THz ($3 \mu\text{m}$). Thus, we use a Fourier transform infrared spectrometer (Tensor 27, Bruker Optik GmbH) for the measurement of optical spectra. As the metamaterial arrays usually have footprints of about $1000 \mu\text{m}^2$, the FTIR is coupled to an infrared microscope (Hyperion 1000, Bruker Optik GmbH) that allows to select one such array for a measurement.

The FTIR-microscope is equipped with a mercury cadmium telluride (HgCdTe) detector that is sensitive in the range of 22 – 300 THz (1 – 13.3 μm) and a potassium bromide (KBr) beam splitter that is transparent in the range of 11 – 230 THz (1.3 – 27 μm). Apart from the beam splitter, the optical components of the microscope are reflective, allowing for measurements in a large infrared frequency range. The light is focused on our samples and collected with two Cassegrain objective lenses ($36\times$, NA = 0.5) as depicted in figure 5.1 (a). Both for transmittance and reflectance measurements, linear polarizers can be used to polarize light before the sample and to analyze its polarization state after the sample.

As our helical metamaterials are chiral, we also want to measure spectra with circularly polarized light. Since no standard components are available for the broad spectral functionality region of our metamaterial, we use a custom made circular polarizer. It consists of a high-extinction wire-grid polarizer (Bruker Optik GmbH) and a super-achromatic MgF₂ quarter-wave plate (Bernhard Halle Nachfolger GmbH).

A quarter-wave plate is a linear birefringent optical component. The incident light has

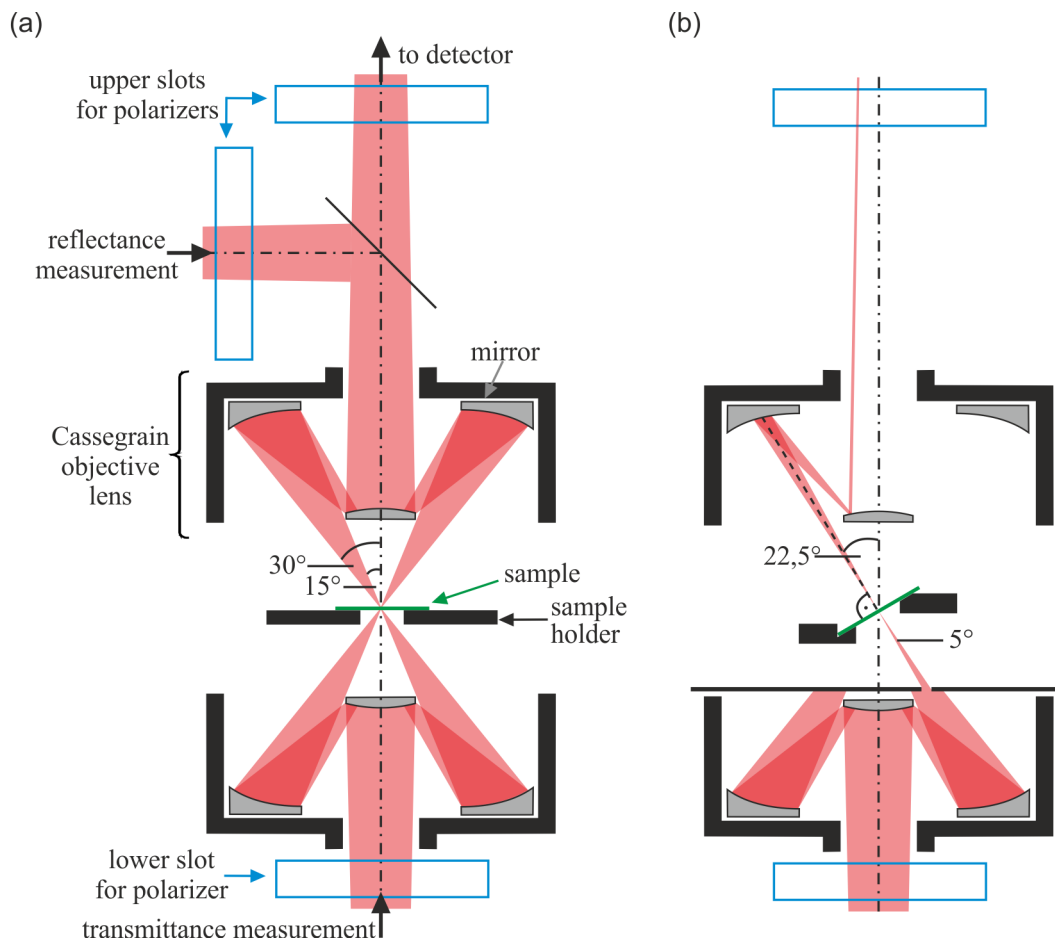


Figure 5.1 Scheme of the microscope setup for measurements (a) with incident angles between 15° and 30° , and (b) with normal incidence. In (a), the beam paths for transmission and reflection measurements are depicted simultaneously while in (b), only the beam path for transmission is depicted as reflection measurements have too low light intensity in this configuration.

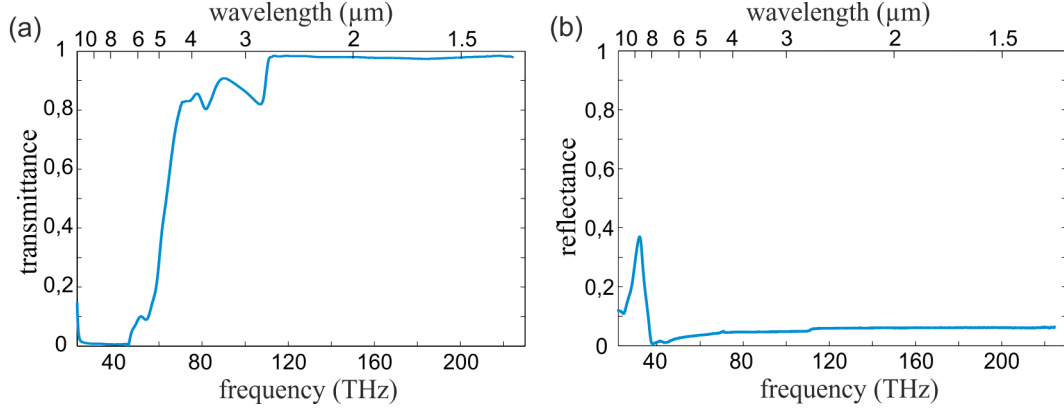


Figure 5.2 Optical spectra of a glass substrate in (a) a transmittance measurement, and (b) a reflectance measurement.

a linear polarization which is oriented with $\alpha = \pm 45^\circ$ toward the optical axis of the quarter-wave plate. After passing it, the component oriented parallel to the optical axis will have a phase difference $\phi = \pi/2$ with respect to the component oriented perpendicular to the optical axis, which corresponds to a spatial shift of $\frac{\lambda}{4}$. As both components have equal amplitudes, a circular polarization results after the wave plate. Depending on the sign of α , it is LCP or RCP.

With the wire-grid polarizer and the super-achromatic MgF_2 quarter-wave plate, a circular polarization results in a broad frequency range of 43 – 120 THz (2.5 – 7 μm) with an accuracy of $\frac{\lambda}{4} \pm 14\%$. However, due to the combination of two components, the size of our custom made circular polarizer allows to use it only in the lower polarizer slot for transmission measurements (see figure 5.1 (a)). Therefore, an analyzation of the polarization state behind the sample was not possible.

The used Cassegrain objective lenses have the disadvantage that light is incident on the sample with angles between 15° and 30° . For transmittance measurements, this can be improved by using a sample holder with a tilt of 22.5° in combination with a circular aperture at the lower Cassegrain objective lens as depicted in figure 5.1 (b). By this means, normal incidence on the sample with a total opening angle of 5° is achieved. This scheme can not be used for reflectance measurements because the collected light intensity is too small.

To determine the transmittance spectrum of a sample, first a reference spectrum $T_{\text{ref}}(f)$ has to be taken. The measurement $T_{\text{meas}}(f)$ is then divided by the reference to yield the transmittance spectrum $T(f)$. The same applies for reflectance spectra. For example, figure 5.2 (a) shows the transmittance spectrum of a glass substrate. The reference spectrum was taken in air. Figure 5.2 (b) shows the according reflectance spectrum. Here, a silver mirror was used as reference.

In the measurements shown in the next chapter, we use the ITO coated glass substrate of a sample as reference for transmittance measurements. As we can see in figure 5.2 (a), the measurements are limited to frequencies above 46 THz (6.5 μm) because the glass substrate becomes opaque below this value. A silver mirror is used as reference for

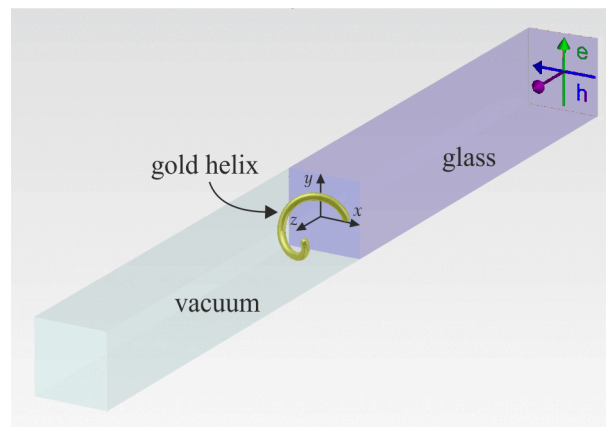


Figure 5.3 Picture of a typical calculation volume. The electric field vector (green), the magnetic field vector (blue), and the wave vector (purple) of the excitation pulse are shown.

reflectance measurements in the next chapter. In this case, the spectral region is limited to 37 THz (8.1 μm) because reflections of the glass substrate falsify the measurements for lower frequencies.

5.2. Numerical Modeling of Helical Metamaterials

Numerical calculations of our metamaterial designs were mainly done with the transient solver of the software package CST Microwave Studio (MWS, CST AG [154]). It is based on a finite integration time domain method, where the time development of electromagnetic fields through a meshed spatial volume is calculated using a leapfrog scheme. The time signals are then Fourier transformed to yield frequency spectra.

Figure 5.3 shows a typical calculation volume with a thin Au helix on a glass substrate. We use realistic parameters for the free-electron Drude model describing the optical properties of Au: The plasma frequency $\omega_{\text{pl}} = 1.37 \cdot 10^{16}$ rad/s and the collision frequency $\omega_{\text{col}} = 1.2 \cdot 10^{14}$ rad/s. The refractive index of the glass substrate is $n = 1.5$. Through periodic boundaries in x - and y -direction, an infinite array of periodic helices results. A Gaussian pulse is excited at the end of the glass half space. In figure 5.3, it is linearly polarized along the y -direction. For this polarization, the transient solver calculates the transmitted and reflected time signals along x - and y -direction. The same is repeated for an excitation pulse polarized along the x -direction.

After Fourier transformation of the resulting eight time signals, we get the frequency dependent, complex coefficients of the Jones matrices for transmission and reflection in the linear basis L . Using the matrix M_{LC} and (2.43), we can directly calculate the Jones matrices for transmission and reflection in the circular basis. The square of the absolute value of these complex coefficients corresponds the respective intensity transmittance and reflectance spectra.

It is also possible to use a circular polarization of the excitation pulse in the MWS

calculations, however only for one frequency at a time. When using this option, the chosen circular polarization is only correct, if the pulse propagates in positive z -direction. If it propagates in negative direction, the choice of “LCP” would lead to the calculation of RCP.

MWS also allows to calculate the spatial behavior of electric and magnetic fields and the complex current density vectors for different frequencies. For example, the current distribution of the split-ring resonator shown in figure 2.6 (c) could be derived in this way.

We used this method to calculate current distributions for different resonance frequencies of uniaxial helical metamaterials [89]. For each point along a metal helix, the current density vectors within a plane normal to the helix line at this point are used. The summation of the current density vectors yields a vector that is proportional to the effective current along the helix line and that points in the direction of the current flow (see section 6.1.1).

One drawback of MWS is that the calculated spectra are limited to wavelengths that are larger than the lateral size of the calculation volume — in our case the lattice constant. A further drawback is that the calculation of oblique incidence of an electromagnetic wave on an array is not possible. Thus, a few calculations have been done using two other software packages. We will mention these packages when a spectrum in chapter 6 was not calculated with MWS. One software package, used by S. Linden, is Lumerical (Lumerical Solutions Inc. [155]). It is based on a finite difference time domain approach. The other software package was used by S. Burger for calculations within a cooperation. It is based on a frequency domain finite element method (JCMsuite, JCMwave GmbH [156]).

6. Helical Optical Metamaterials

In this chapter, we want to present our findings about the optical properties of Au helical metamaterials. In the first section, we discuss the properties of uniaxial helical metamaterials for incidence of electromagnetic waves along the helix axis and the interaction of single helices with their neighbors in an array. We present fabricated structures which were designed for this excitation configuration. They exhibit strong circular dichroism in a broad spectral range and thus can be used as broadband circular polarizers. In the second section, other excitation geometries of helical metamaterials are discussed. In particular, we show a fabricated design for propagation of electromagnetic waves perpendicular to the helix axis. In the last section, we present metamaterial arrays of tapered helices. These structures are designed for application as improved broadband circular polarizers.

6.1. Uniaxial Helical Metamaterials for Axial Propagation

Our uniaxial helical metamaterials consist of arrays of parallel helices. We use numerical calculations to study the chiral optical properties of helical metamaterials in the case of axial propagation, and how these properties depend on different geometrical parameters of the helices. Our design is similar to the proposition of [31] for the composition of axial bianisotropic media (see section 2.3.3). However, while axial bianisotropic media are not chiral for axial propagation, we will see that our structures exhibit even stronger chiral properties for axial than for transversal propagation.

After having studied the optical properties by numerical calculations, we will discuss measurements of helical metamaterial arrays like the ones shown in figure 4.12. They reveal strong and broadband circularly polarizing properties.

As we will see, numerical calculations show that interaction effects between the helices are present. In the last part of this section, we experimentally reveal the influence of these interaction effects by using superlattices of helices with different configurations.

6.1.1. Optical Properties of Uniaxial Helical Metamaterials

We want to study the chiral optical properties of helical metamaterials by using numerical calculations. To this end, we use an idealized structure design. It is a left-handed Au helix with helix radius R , wire radius r , pitch height (or axial period) p , and lateral lattice constant a as indicated in figure 6.1 [83]. The number of pitches is $N = 1$. The helix wires are terminated with Au half spheres of the radius r and the helix rests on a glass substrate without intersections in order to avoid artificially sharp edges.

We calculate spectra for transmission of light incident normal to the glass substrate from the air side and exclusively show results for left-handed helices. By symmetry, for

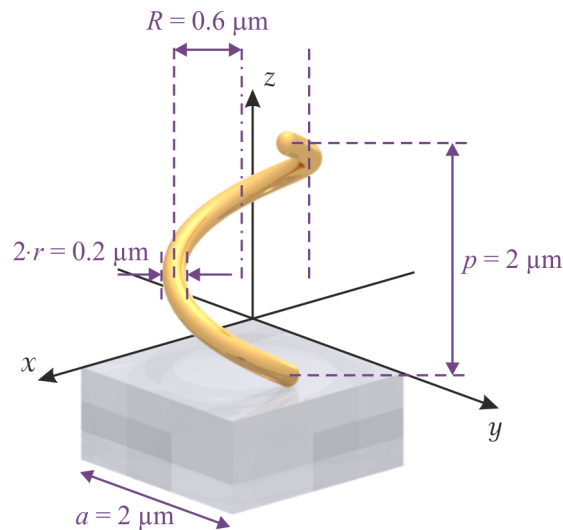


Figure 6.1 One lateral unit cell of the uniaxial helical metamaterial that was used for numerical calculations [83].

right-handed helices, the transmittance Jones matrices $M_{T,C}$ are strictly identical if “l” and “r” are interchanged for all four matrix elements.

Connection between Split-Ring Resonators and Helices

Before considering the spectrum of a helical metamaterial, let us start with a structure that is often used as a metamaterial building block: the split-ring resonator. We showed the spectrum of a split-ring resonator metamaterial for transmission of linearly polarized light in figure 2.7. An incident electromagnetic wave with circular polarization can also induce resonances in a split-ring resonator.

Figure 6.2 (a) shows spectra for a circular split-ring resonator with a radius $R = 0.6 \mu\text{m}$, a wire radius $r = 0.1 \mu\text{m}$, a lateral lattice constant $a = 2 \mu\text{m}$, and a gap of 200 nm between the wires. “LCP” and “RCP” refer to the total transmittance T of the respective incident circular polarizations with no analyzer behind the sample. First of all, we notice that the spectrum is identical for LCP and RCP. This is because a split-ring resonator is obviously not chiral for normal incidence. We see two distinct resonances. The corresponding current distributions are indicated to the right of the spectra. A continuous current mode is present for the long wavelength fundamental resonance while a current mode with one node is present for the short wavelength resonance.

Adiabatically pulling the right end of the circular split-ring resonator out of the plane (while keeping the diameter constant) leads to almost one pitch of a left-handed helix. If we make the helix line longer, so that the two ends are above each other when looking along the z -direction, we get a helix with one pitch height as indicated in figure 6.2 (b). The geometrical parameters are as depicted in figure 6.1. Due to the break in symmetry, now only LCP, which has the same handedness as the helix, can couple to the structure. Like for the split-ring resonator, two current modes are present: a continuous current for

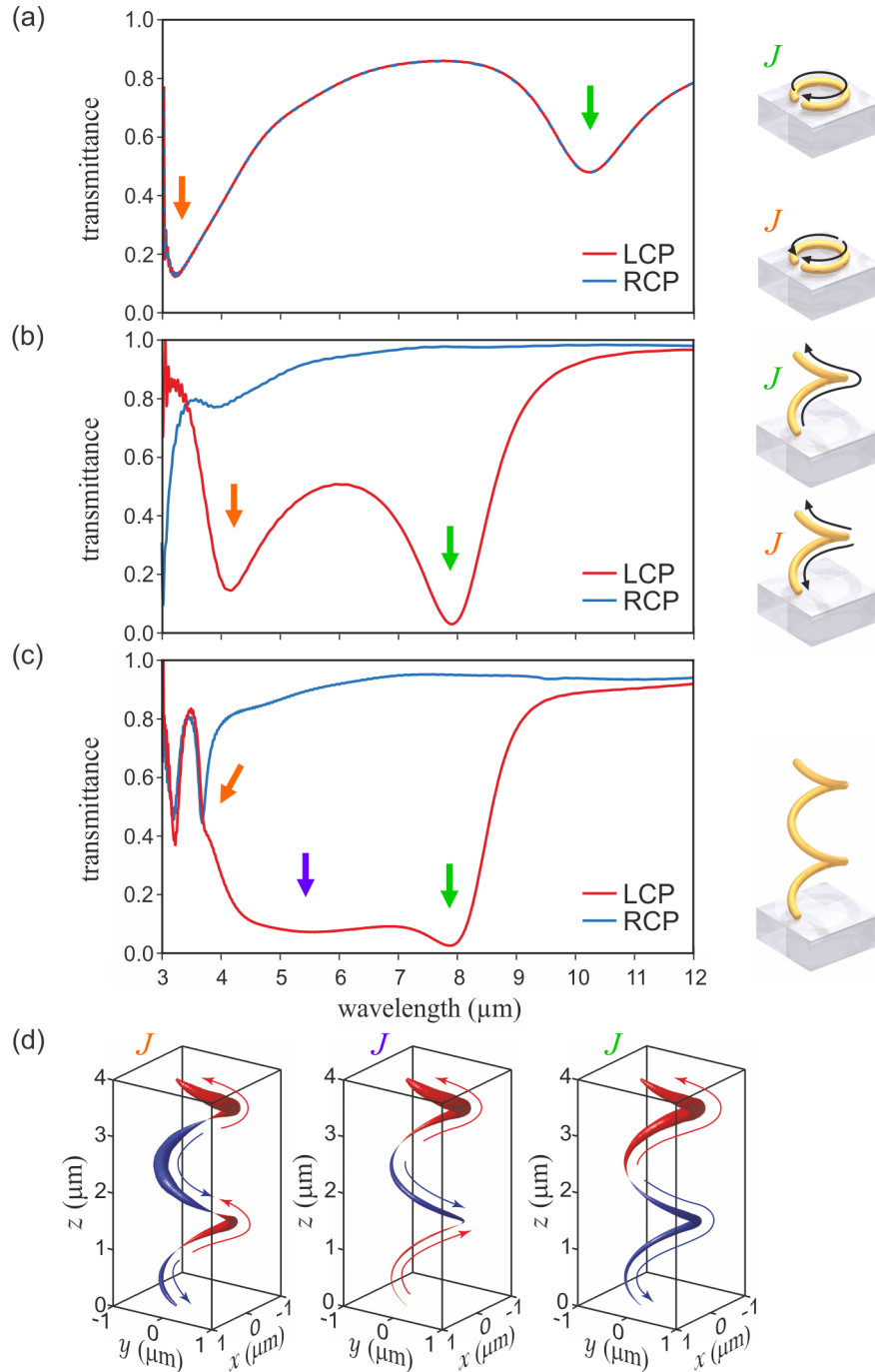


Figure 6.2 Connection between split-ring resonators and helices. Transmittance spectra of LCP and RCP incident light normal to the substrate are shown in the left column. The right column depicts the current distributions of resonances as indicated by the arrows. The spectra are calculated for: (a) A split-ring resonator, (b) one pitch of a helix, and (c) two pitches of a helix. (d) Snapshots of the electric current distributions along the helix line for the three resonances in (c). The absolute value of the current is encoded by the curve thickness and the sign by red and blue color (see red and blue arrows) [89].

the long wavelength resonance around $8\ \mu\text{m}$ and a current mode with one node for the short wavelength resonance around $4\ \mu\text{m}$. For RCP, we see a high transmittance.

We see that the electromagnetic modes of split-ring resonators and helices with one pitch are closely related [89]. Intuitively, a helix under normal incidence of light acts somewhat similarly to a split-ring resonator under oblique incidence. In fact, so called extrinsic chirality [85, 157] has been observed for planar arrays of split-ring resonators excited under oblique incidence [7]. This is due to the asymmetry introduced by the tilt between structures and incident light. In that case, the symmetry conditions mentioned in section 2.3.2 can also be fulfilled by a planar split-ring resonator. However, then also additional linear birefringence [7, 85] is present. Hence, in general, the polarization eigenstates do not correspond to circular but rather to elliptic polarizations.

In contrast, linear birefringence is largely eliminated in our helical metamaterial design [89]. For the conditions of figure 6.2 (b), intensity conversion of incident light with RCP to transmitted light with LCP is below 5% in the $3.75\ \mu\text{m}$ to $7.5\ \mu\text{m}$ range.

Broadband Properties of Helical Metamaterials

The situation gets more complex for the case of two helix pitches. We find a transition from sharp resonances for one helix pitch and LCP in figure 6.2 (b) to a broad band of low transmittance for two pitches in figure 6.2 (c). The intensity conversion of the incident circular polarization is again low (below 5% in the same sense as above). To clarify the nature of this broad band of low transmittance, we look at the current distributions once more. They are depicted in figure 6.2 (d) for each of the three wavelengths marked by the arrows in figure 6.2 (c). In order to get a better visualization, the modulus of the current is depicted by the curve thickness and the color indicates the direction of the current. The three depicted modes closely resemble standing waves as the positions of their current nodes change only slightly with time [89]. The modulus of the currents decreases along the negative z -direction due to the fact that light is incident from the air side.

When comparing the three current modes, we see that the number of nodes decreases from three to one as wavelength increases. The superposition of these three modes leads to the broad spectral response in figure 6.2 (c). This broad band of low transmittance could be used for the design of a broadband circular polarizer.

In the language of solid-state physics, the unusual broadband operation originates from the interaction between the different pitches of a helix [83]. This behavior is analogous to that of discrete atomic levels evolving into broad electronic bands in a crystalline solid. In other words, in addition to the discussed internal resonances that mainly determine the optical response, Bragg resonances become important as well in helical metamaterials.

If we treat the helix wire material as an ideal conductor rather than as a Drude metal with finite plasma frequency and damping, the calculation results are similar. Returning to the Drude metal Au, this observation indicates that the effects can, in principle, be scaled by structure size to any desired wavelength range, provided that the operation wavelength is sufficiently below the plasma frequency [89]. This observation also indicates

that the missing light for the low-transmittance circular polarization is reflected rather than absorbed.

The parallel helices in our design are similar to the proposed design for axial bianisotropy [31] discussed in section 2.3.3. We remind that for axial bianisotropy, no chiral effects are present for propagation along the preferential direction, *i.e.* the helix axis. This is true for the fundamental resonance (without current nodes) of a helix with more than one pitch height. In that case, the fundamental resonance cannot be excited by incidence of light parallel to the helix axis as we can see in part (d) of figure 6.2 (for longer wavelengths than the ones shown, no further resonances occur for axial propagation). Yet we see a strong chiral effect of our helical metamaterials for propagation along the preferential direction. This arises from the discussed higher resonances depicted in figure 6.2 (d). Thus, our metamaterial rather resembles a general uniaxial bianisotropic medium.

We pointed out the properties of helical radio antennas in the end-fire geometry in section 2.3.6. Like our metamaterial building blocks, these helical radio antennas are sub-wavelength structures which is apparent from (2.80). An electrical current in a left-handed helical antenna in the end-fire geometry leads to emission of LCP light propagating along the helix axis. Thus, an electromagnetic wave with LCP propagating in the opposite direction will induce an electrical current in such an antenna.

Transferring this to the case of a two-dimensional square array of helical antennas, we expect reflection and/or absorption of light incident onto the array if the handedness of the light is identical to that of the helices [83]. Light with the opposite circular polarization is expected to be mainly transmitted as interaction with the helices is small. These expectations are fulfilled by our helical metamaterial arrays as presented in figure 6.2. However, in our comparison between helical radio antennas and helical metamaterials, we assumed that lateral interaction among the different helices of an array is negligible. While this is the case for helical radio antennas [82], this point will be clarified for helical metamaterials within the next part of this section.

6.1.2. Dependence of the Optical Properties on Geometrical Parameters

In order to get a better understanding of the optical chiral properties of helical metamaterials, for example the interaction effects of single elements in an array, we will present calculated spectra of helices with different geometrical parameters [83]. This parameter study can also help to choose an appropriate design for the realization of a broadband circular polarizer. To gain more information, “transmittance” will refer to the ratio of LCP (RCP) transmitted and LCP (RCP) incident light intensity, while “conversion” will refer to the ratio of LCP (RCP) transmitted and RCP (LCP) incident light intensity. Starting with the helix parameters shown in figure 6.1, we will vary one parameter at a time while keeping the others at the values given there. In addition, we also investigated the reflection properties of helical metamaterials.

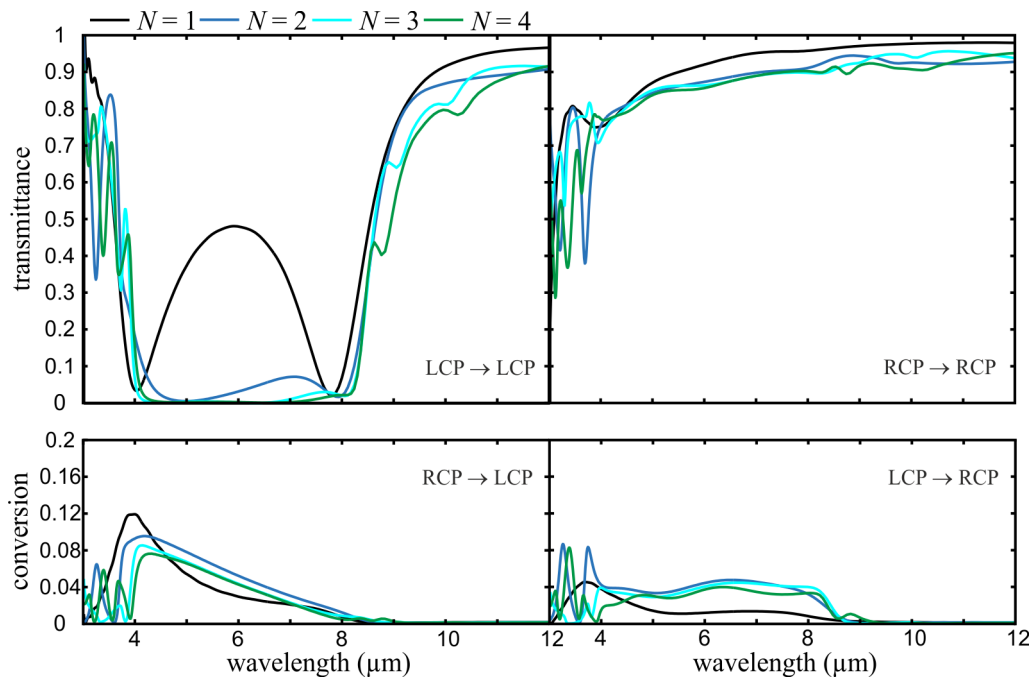


Figure 6.3 Intensity transmittance and conversion spectra (please note the different vertical scales). In each figure part, the circular polarization in front of the arrow refers to incident light while the circular polarization behind the arrow refers to transmitted light. The number of helix pitches N is varied [83].

Variation of the Number of Pitches N

As a logical continuation of the structures presented in section 6.1.1, we want to further increase the number of helix pitches. For $N = 1$, figure 6.3 shows the two distinct resonances already discussed above. For $N = 2$, a broad band of low transmittance evolves for LCP that is even more pronounced for $N = 3$ and $N = 4$. With respect to the design of a broadband circular polarizer, we see that although the suppression of LCP is better with increasing N , a helix with two pitches height already shows strong suppression. Notably, the minimum and maximum wavelengths do not shift much with increasing N . This means that none of the resonances shifts proportional to the total length of the Au wire or proportional to the height of the structure [83].

Variation of the Pitch Height p

Next, we vary the pitch height p as illustrated in figure 6.4. The remaining parameters are fixed to the values given in figure 6.1. Please note that the black spectra in figures 6.3 to 6.7 correspond to equal geometry parameters. When changing p , obviously the two resonances shift their positions to some extent. However, while the pitch height p varies by more than a factor of three, the resonance positions merely shift by some tens of percent [83]. This behavior is quite different from that of dielectric chiral

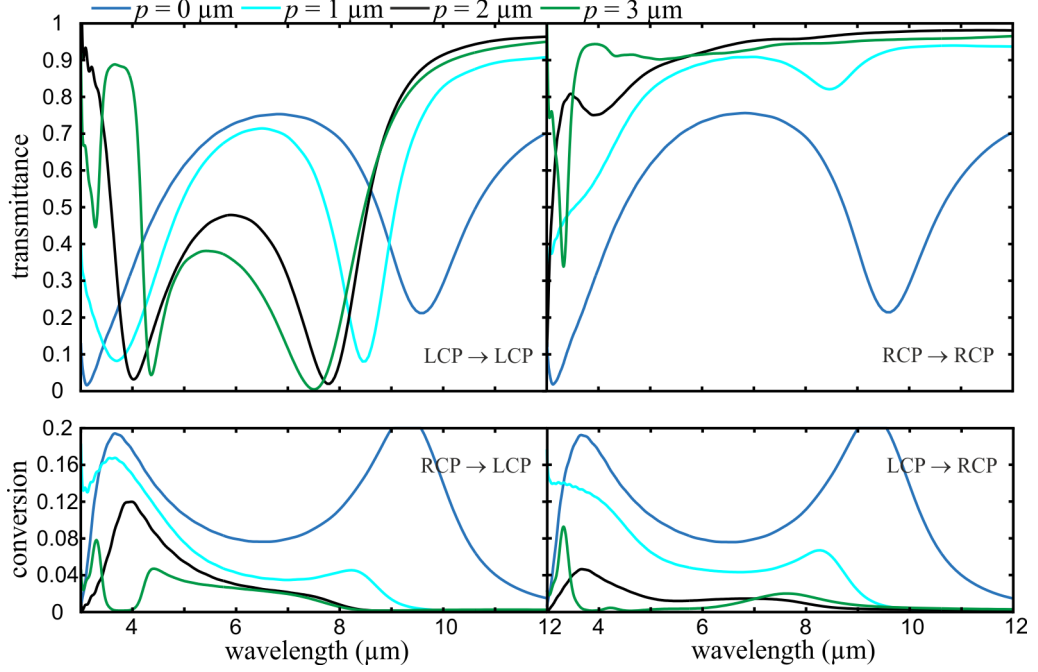


Figure 6.4 As figure 6.3 for $N = 1$, however with a variation of the pitch height p . The case $p = 0 \mu\text{m}$ corresponds to a planar split-ring resonator with $R = 0.6 \mu\text{m}$, $r = 0.1 \mu\text{m}$, $a = 2 \mu\text{m}$, and a gap width of 100 nm [83].

structures [87, 93, 94] like dielectric helix photonic crystals [87], where the operation wavelength is directly proportional to the period along the propagation direction. Thus, in dielectric chiral structures, the optical response is dominated by Bragg resonances. In contrast, in Au helical metamaterials, the optical response is determined by the interplay of pronounced internal resonances and their mutual coupling within one helix. With regard to a circular polarizer design, we see that an increase of p leads to lower conversions which is desirable.

Variation of the Lattice Constant a

As mentioned in the previous section, we want to know if and to what extent interactions of helices in an array influence the optical properties. To this end, we vary the lattice constant a . The respective spectra shown in figure 6.5 have been calculated using Lumerical. In contrast to helical radio antennas, obviously interaction between individual helices is present in our case. Both resonances shift to shorter wavelengths for a decreasing lattice constant, with a more pronounced shift of the long-wavelength resonance. This is the fundamental resonance of a helix with one pitch (see figure 6.2 (b)). It corresponds to a continuous current along the helix without nodes. Thus, a snapshot of the magnetic field of this mode is similar to that of a permanent magnet [83]. Imagine two parallel oriented permanent magnets with the north (south) poles side by side. The energy of this system increases when decreasing the distance between the two magnets. This

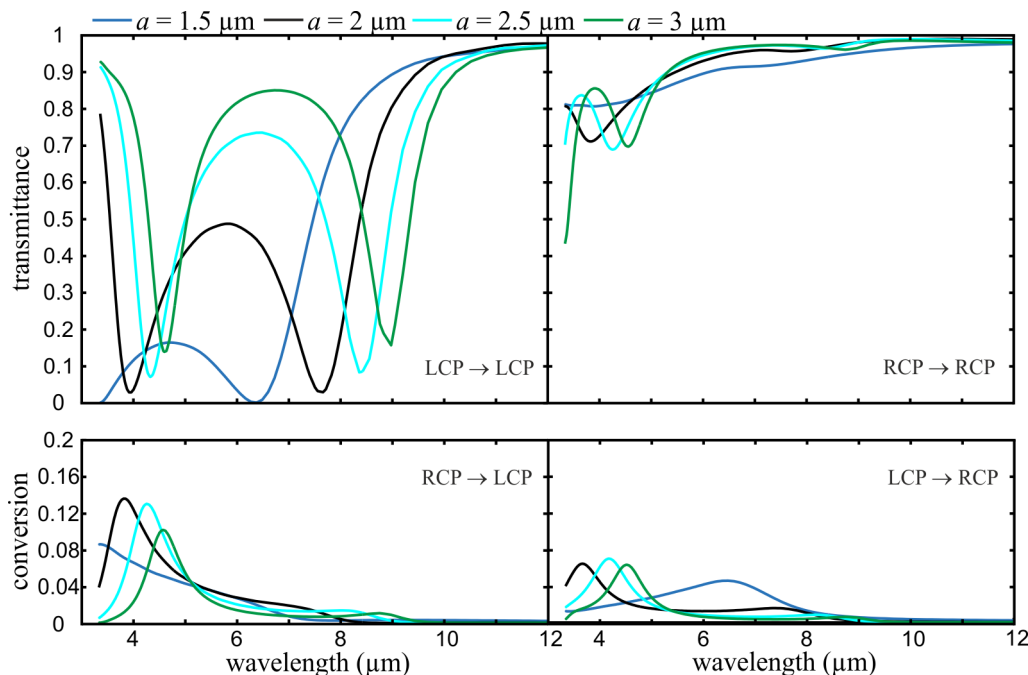


Figure 6.5 As figure 6.3 for $N = 1$, however with a variation of the lateral lattice constant a [83].

analogy qualitatively explains the behavior of the long-wavelength resonance in our helical metamaterials. The short-wavelength resonance corresponds to a current mode with one node as explained in section 6.1.1. Thus, the lower and the upper part of the helix have anti-parallel magnetic dipole moments. The interaction of helices with such anti-parallel magnetic dipole moments can qualitatively be understood in the same sense as described above. We also see that the depth of the resonances increases with decreasing lattice constant. This is due to the fact that then, the number of magnetic dipoles per unit volume, or unit area, increases.

In spite of mutual interactions, the overall qualitative behavior of helical metamaterials stays similar to that of end-fire helical radio antennas. Optimum circular polarizer operation is expected for dense packing of the helices. However, individual structures should not touch each other, as then the picture of separated antennas is obviously no longer applicable [83].

Variation of the Helix Radius R

The parameter with the strongest influence on the resonance positions is the helix radius R . When increasing the helix radius, we see a redshift for both resonances in figure 6.6 that is more or less proportional to R . Also, the distance of the resonances increases with increasing R . This is expected according to antenna theory, where the functionality region is given depending on the helix radius (2.80). Even the absolute positions of the resonance wavelengths roughly coincide with the prediction of antenna theory. The depth of

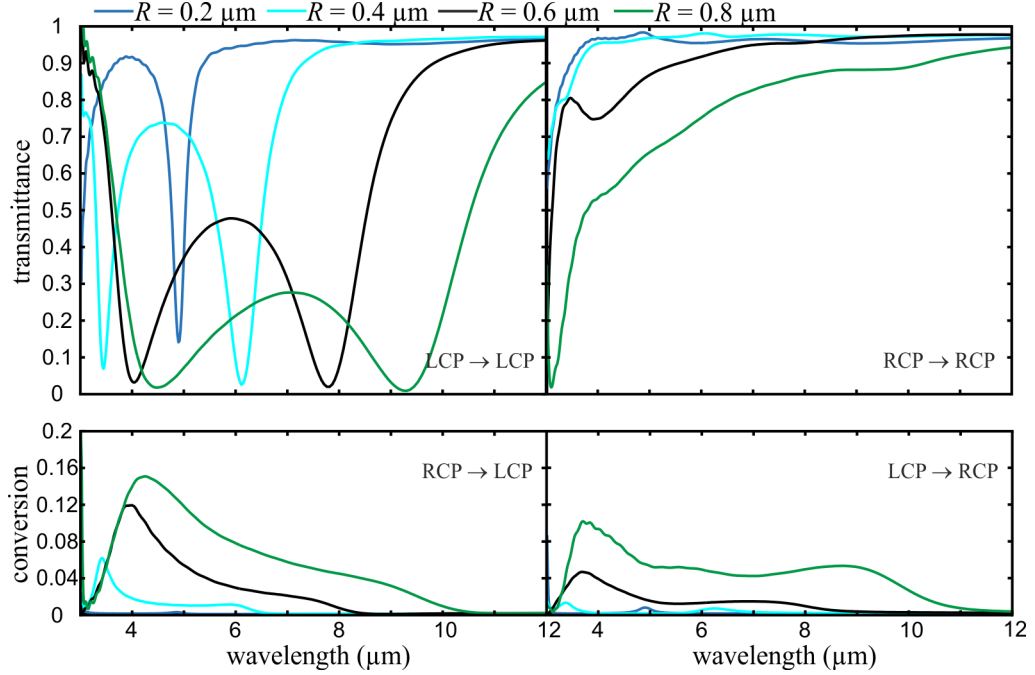


Figure 6.6 As figure 6.3 for $N = 1$, however with a variation of the helix radius R [83].

of the resonances decreases with decreasing helix radius. This is because the lattice constant a stays at a constant value and thus the array is diluted [83]. By increasing R , the bandwidth of a circular polarizer can be increased, as long as the conversions stay sufficiently low.

Variation of the Wire Radius r

Figure 6.7 shows the calculated spectra for a variation of the wire radius r . With increasing r , the resonances shift to shorter wavelengths. This trend can be understood by recalling that an electrical current follows the shortest possible path. In our case, this means that the current is mainly flowing at the inner radius of a helix, corresponding to $R - r$. Thus, by increasing r , we effectively reduce the helix radius [83]. Accordingly, we see a blueshift of the resonances.

Reflection Spectra

Although less interesting with regard to circular polarizer properties, the reflectance spectra are interesting with regard to the optical properties of helical metamaterials. In figure 6.8, we see that incident light with LCP is mainly reflected as LCP. This is contrary to the behavior of an Au mirror (as visible by the red curves in figure 6.8) or the behavior of an usual dielectric half-space according to Fresnel-type reflection [27]. There,

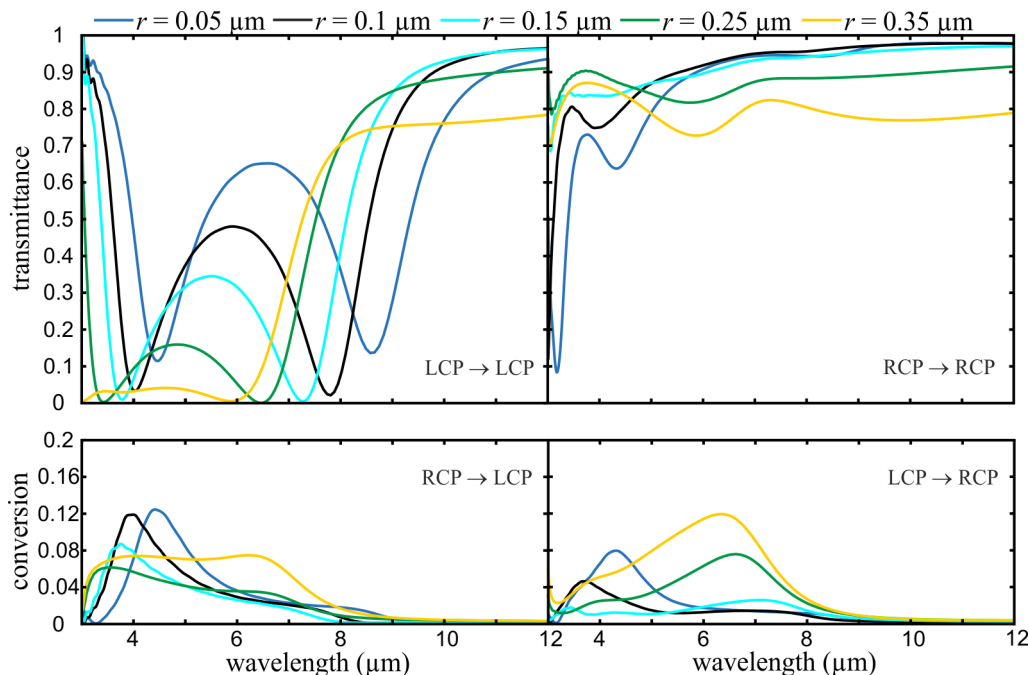


Figure 6.7 As figure 6.3 for $N = 1$, however with a variation of the wire radius r [83].

reflected circularly polarized light flips the handedness from LCP to RCP and *vice versa* upon 180° change of the direction of the wave vector of light. The reflection behavior shown in figure 6.8 is also not expected for ideal chiral media [31, 158].

Intuitively, we interpret this numerical finding as being due to the fact that our helices are not infinitely long but have two ends. These ends introduce a preferred direction normal to the helix axis. Thus, our helical metamaterials are not strictly uniaxial. In addition to pure circular dichroism, they also exhibit some degree of linear birefringence [83]. This linear birefringence contributes to the observed circular polarization conversion in transmission geometry. It also explains the non-Fresnel-type reflectance: We can imagine incident light with LCP to be composed of two orthogonal linearly polarized components. If the relative phase between these two changes by 180° , the reflected light will have LCP. The stronger effects in reflectance than in transmittance are not surprising as phase changes at a structure's surface usually have a much more profound effect on the reflection properties than on the transmission properties [83].

We also want to note that the reflectance spectra (“RCP → LCP” and “LCP → RCP”) in figure 6.8 are nearly identical — in contrast to the conversion spectra for transmission in figures 6.3 to 6.7. For normal incidence onto a non-chiral medium exhibiting linear birefringence, it is straightforward to show that the spectra for RCP → LCP and LCP → RCP are strictly identical. Thus, this finding again highlights the influence of linear birefringence on the reflection spectra of helical metamaterials [83].

The pronounced conversion in figure 6.8 does not allow to derive effective material parameters, as proposed for a biisotropic chiral medium by means of a retrieval in [158]. However, the high reflectance supports our above reasoning, that in the wavelength regions

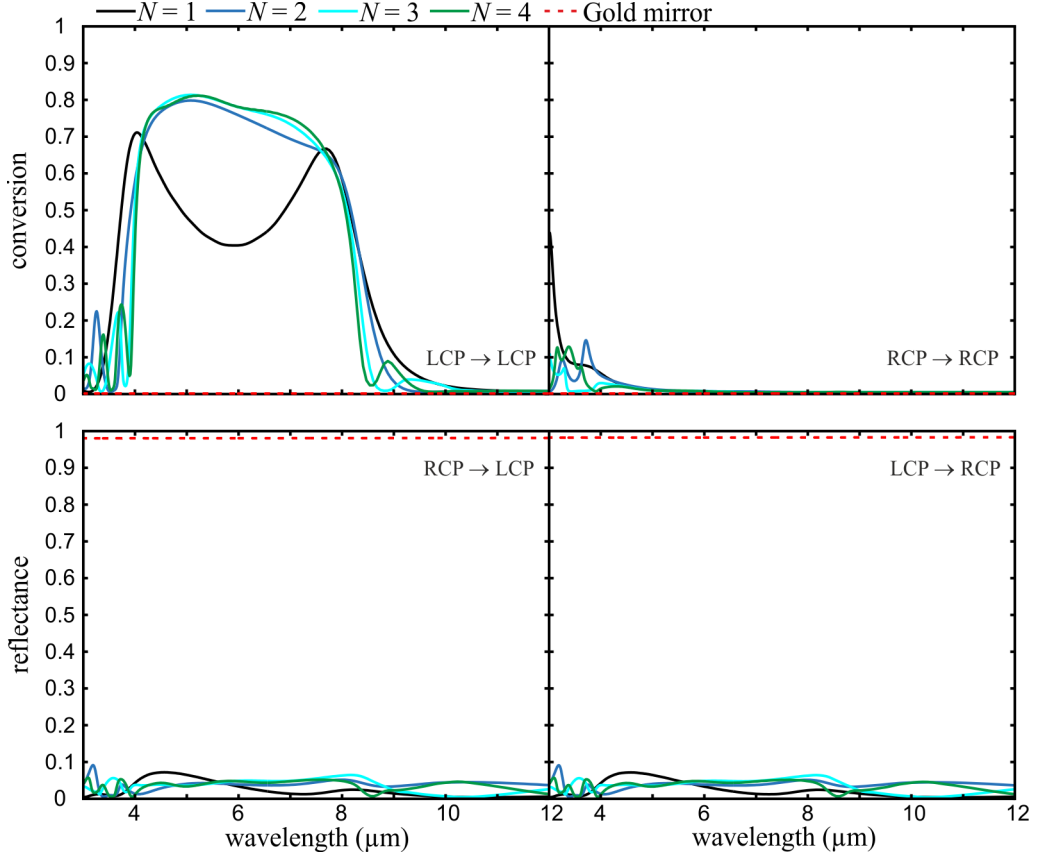


Figure 6.8 As figure 6.3, however here the intensity reflectance and conversion spectra for varying values of N are shown. The red dotted curves show the calculated spectra of a Au mirror. Please note that in relation to Fresnel-type reflection, now “RCP → LCP” and “LCP → RCP” refer to reflectance spectra while “LCP → LCP” and “RCP → RCP” refer to conversion spectra [83].

with low transmittance most light intensity is reflected rather than being absorbed. In the case of helices made of a perfect conductor, the sum of transmittance and reflectance is one, leading to a high reflectance at the spectral resonance positions.

6.1.3. Helical Metamaterials as Broadband Circular Polarizers

We have discussed calculated optical spectra of helical metamaterials under normal incidence of circularly polarized light in the previous parts of this section. Depending on the geometry parameters of the helices, a broad band of low transmittance is present for the circular polarization with the same handedness as the helices, while the circular polarization with the opposite handedness is mainly transmitted. Here, we present fabricated helical metamaterials which reproduce this broadband polarizing property [89]. The fabricated structures also reproduce the transition from distinct resonances to a broadband behavior which we have seen in figure 6.2 (b) and (c).

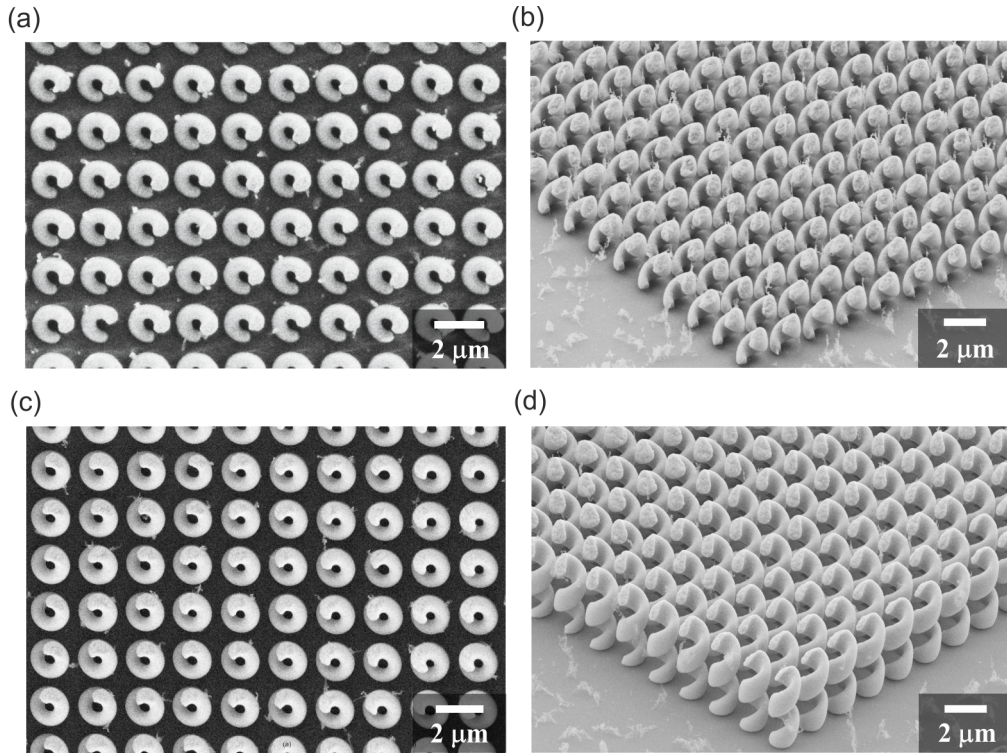


Figure 6.9 (a) Top view, and (b) oblique view of an array of left-handed helices with almost one pitch height. (c) Top view, and (d) oblique view of an array of right-handed helices with two pitches height. The white flakes are polymer residues.

Figure 6.9 shows SEM micrographs of arrays of left-handed helices with almost one pitch height in parts (a) and (b), and with two pitches height in parts (c) and (d). The helices have nominal pitch height $p = 2 \mu\text{m}$ and helix radius $R = 0.6 \mu\text{m}$, and are arranged in a square array with lattice constant $a = 2 \mu\text{m}$. The wire diameter depends on the used energy dose during DLW. It has a value of around $0.5 \mu\text{m}$ parallel to the substrate and a value of around $1.5 \mu\text{m}$ perpendicular to the substrate.

Measured optical transmittance spectra of these structures for incident circular polarization of light are shown in figure 6.10. The gray shaded region of wavelengths above $6.5 \mu\text{m}$ cannot be evaluated as the glass substrate becomes opaque there. For comparison, we also show calculated spectra in figure 6.10. The used geometrical parameters are as close to the fabricated structures as possible, as indicated by the insets.

Spectra of left-handed helices with almost one pitch height are shown in figure 6.10 (a). We see a distinct resonance for incident light with LCP while incident light with RCP is mainly transmitted. In contrast to the calculated spectra shown in figure 6.2 (b), we only see one resonance. This is probably due to the larger wire thickness which leads to a blueshift of resonances as discussed above. Thus, the short-wavelength resonance lies outside the metamaterial limit. Figure 6.10 (b) reveals the theoretically anticipated blocking of light with LCP for left-handed helices with two pitches height. As light with RCP is mainly transmitted, a large extinction ratio results in the wavelength range from $3.5 - 6.5 \mu\text{m}$ [89].

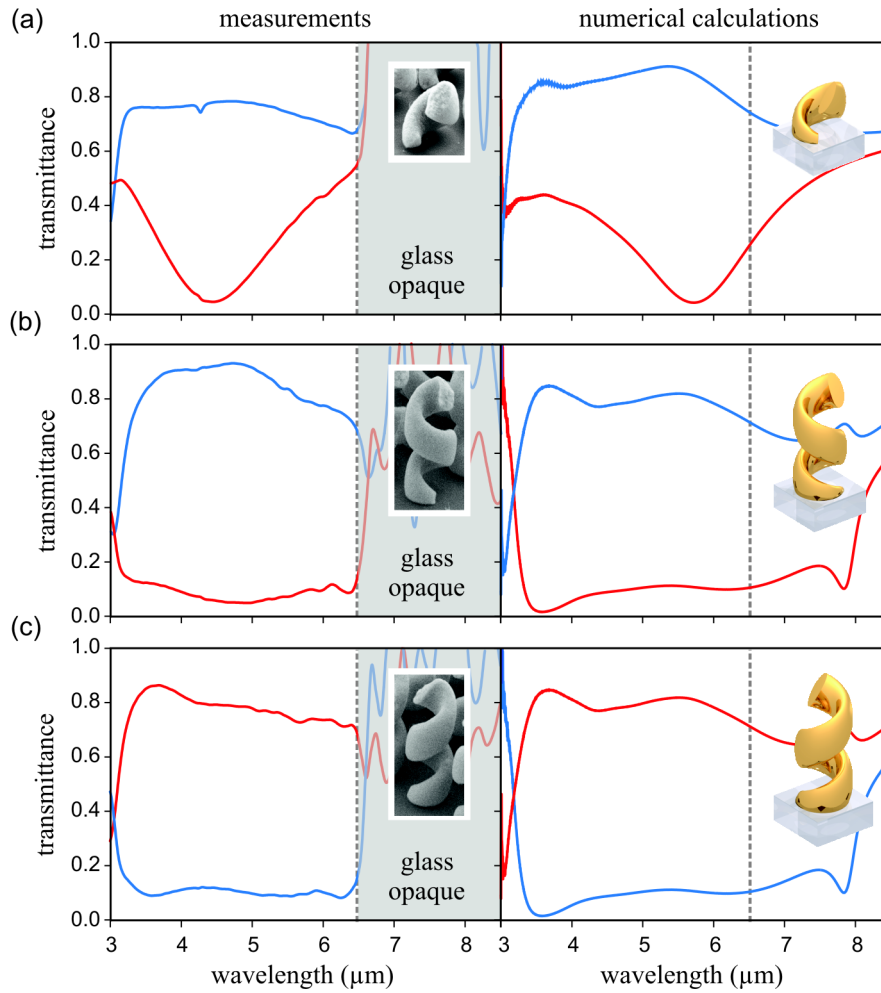


Figure 6.10 Measured (left column) and calculated (right column) transmittance spectra for helical metamaterials under normal incidence of light with LCP (red) and RCP (blue). The spectra are shown for (a) left-handed helices with almost one pitch height, (b) left-handed helices with two pitches height, and (c) right-handed helices with two pitches height. The insets show single helices of the respective measured and calculated arrays. The fabricated arrays of left- and right-handed helices with two pitches height are located on the same substrate and have comparable geometrical parameters [89].

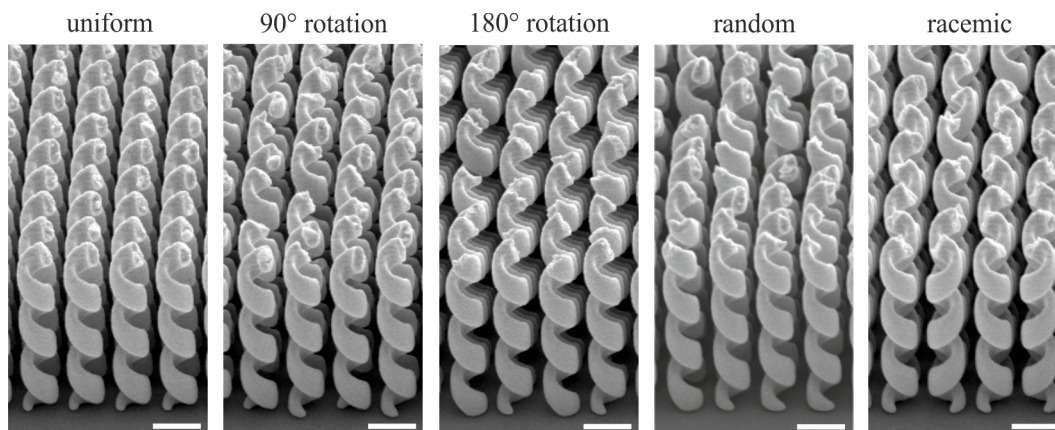


Figure 6.11 SEM pictures of helices with $N = 3.2$ for the five different superlattice configurations. The scale bar is $2 \mu\text{m}$.

This behavior is reproduced for right-handed helices and light with RCP as shown in figure 6.10 (c). The wavelength region with suppression of one circular polarization has a bandwidth of almost one octave for the measurements and even more for the calculations. Thus, our helical metamaterials could be used as compact broadband circular polarizers in the infrared spectral range. This could be an alternative to the use of wave plates for the adjustment of circular polarizations as they usually have rather narrow functionality bands. The wave plate we use for our measurements is a costly one-off production and is already at the edge of covering the whole wavelength range of our circular polarizer design.

6.1.4. Helical Superlattices

Numerical calculations of helical metamaterials with varying lattice constants have indicated that interaction effects between single helices are not negligible [83]. Here, we will present fabricated superlattices of Au helices to experimentally confirm the influence of these interaction effects. Such superlattices of *polymer* helices have been discussed in the context of chiral photonic crystals in [159] by M. Thiel *et al.* There, an additional stop-band appeared for superlattices that was not present for uniform square arrays of polymer helices. The DLW step of the structures shown in this section has been done by M. Thiel. Superlattices of left-handed helices with three different heights and five different configurations have been fabricated and measured. Figure 6.11 shows SEM micrographs of helices with $N = 3.2$ for the five checkerboard-like configurations: uniform arrays like the ones previously shown, arrays where every other helix is rotated by 90° with respect to its helix axis, arrays where every other helix is rotated by 180° , arrays where all helices are rotated by a random phase around their helix axes, and racemic arrays where every other helix is right-handed. The geometrical parameters of the helices are: $p = 2.3 \mu\text{m}$, $R = 0.5 \mu\text{m}$, and $a = 2 \mu\text{m}$ (the wire radius is similar to the previously shown helices).

Measured transmittance spectra for incident light with LCP and RCP are shown in figure 6.12. The three columns correspond to $N = 1$, $N = 2$, and $N = 3.2$, while the rows corre-

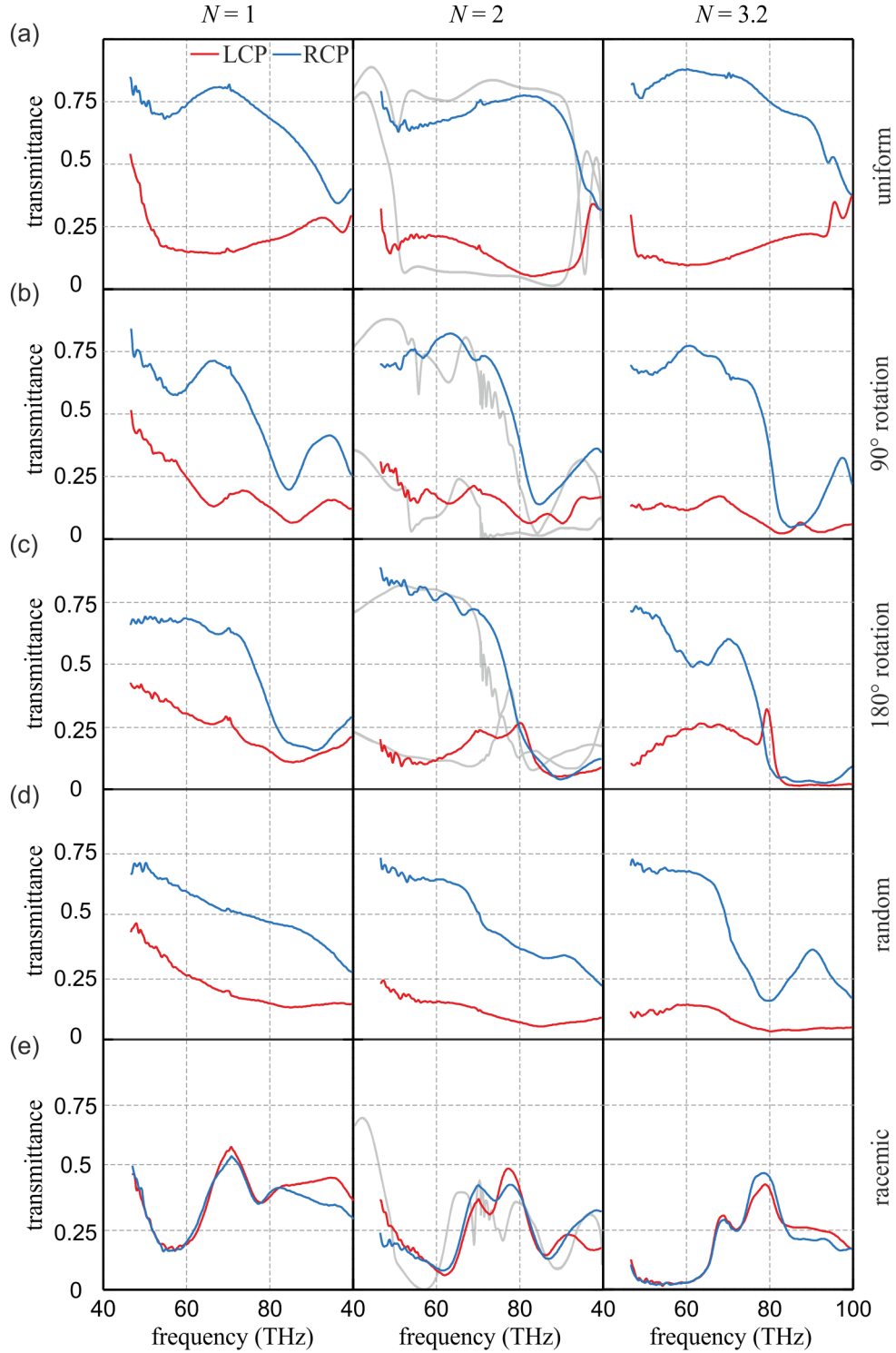


Figure 6.12 Measured spectra for normal incidence of light with LCP (red) and RCP (blue) for different numbers of pitches. For $N = 2$, also calculated spectra are shown (gray), except for the random configuration where a calculation is obviously not possible. To the right, the superlattice configuration of each row is given.

spond to different superlattice configurations. For the case of two pitches, also calculated spectra are shown as a comparison. In the first row, again the evolution of broadband circular dichroism with increasing N is visible. The differences to figure 6.10 are due to the different geometrical parameters of the helices, in particular the pitch height. In figure parts (b) and (c), we see considerable change of the optical properties. In both cases, strong resonances for RCP of light appear for high frequencies. In particular, in the case of 180° rotation, a broad region with low transmittance for both circular polarizations evolves for $N = 2$ and $N = 3.2$. Please note that now one unit cell contains two helices and its size increases to $\sqrt{2}a$. Hence, the structures can be viewed as a metamaterial only for frequencies below 70 THz. Directly above 70 THz, one would expect to see Wood anomalies [160, 161]. While an effect is clearly visible in the calculations, these fine structures are probably averaged out in the measurements due to deviation from normal incidence and variations between helices in an array. For low frequencies, we see that the circular polarizer functionality band is extended in comparison to uniform arrays. For arrays with 180° rotation, it extends down to 30 THz in the calculations.

Due to linear birefringence of the structures, we can assume that the coupling of incident light to the helices will depend on the relative orientation of the electric field vector and the ends of the helices. Thus, the coupling will be different for helices with different rotation. Also, the interaction of helices in an array will be affected by the mutual rotation. Figure 6.12 (d) shows measured spectra for arrays with random rotation. In this case, a numerical calculation of spectra is obviously not possible using our numerical method. In comparison to the other rows, the spectra of random arrays are quite smooth. Both the coupling of the electric field to helices and the mutual coupling of individual helices will vary locally within an array. Thus, many different coupling configurations are present at the same time and lead to this smooth behavior in contrast to pronounced resonances. In fact, if we take the mean of the spectra in figure 6.12 (a) – (c), the random spectra are already approached quite well (not shown).

Arrays of randomly rotated helices with parallel helix axes have been proposed for the realization of axial bianisotropic metamaterials [31] as we mentioned in section 2.3.3. However, we have to keep in mind, that in our case higher resonances play a crucial role while there, the fundamental resonance was considered. Still, the random orientation might reduce linear birefringence and hence conversion.

Finally, racemic mixtures are shown in the last row of figure 6.12. The behavior for incident light with LCP and RCP is very similar in the measurements and identical in the calculations. When considering the racemic configuration in figure 6.11, we see that a mirror plane is present parallel to the helix axes. According to the symmetry conditions discussed in section 2.3.2, no chirality should be present in this case. Thus, neither optical activity nor circular dichroism should be present. The spectra shown in figure 6.12 (e) behave according to these expectations.

Numerical calculations of the reflection spectra of superlattices with left-handed helices and $N = 2$ have shown that, within the metamaterial limit, the behavior is analogous to that shown in figure 6.8, *i.e.* incident light with LCP is mainly reflected as LCP. In contrast, the reflectance spectra of the racemic configuration show that incident light with LCP (RCP) is mainly reflected as RCP (LCP). Thus, the reflection is in accordance to that expected from a mirror.

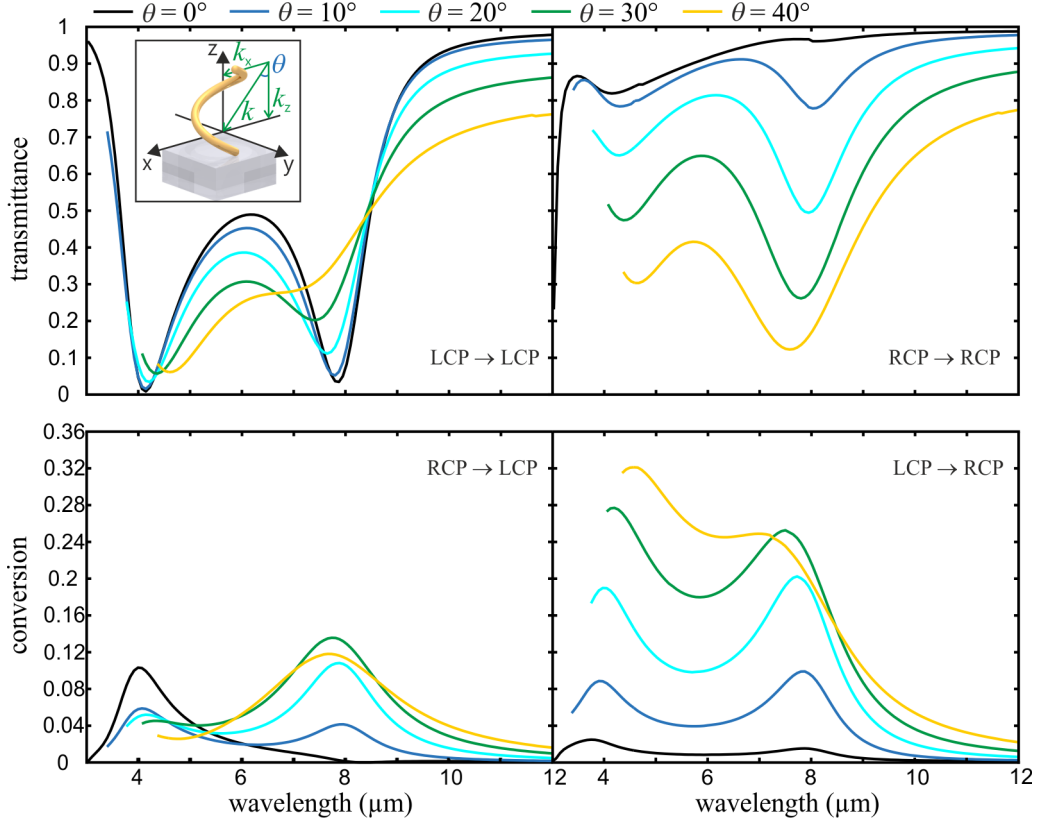


Figure 6.13 Intensity transmittance and conversion spectra (please note the different vertical scales) for circularly polarized incident light propagating along different directions as indicated in the inset. The geometrical parameters of the helix are identical to the ones shown in figure 6.1 [83].

6.2. Helical Metamaterials for Oblique and Transversal Propagation

So far, we have discussed the optical properties of arrays of parallel helices under incidence of light parallel to the helix axis. In this section we are concerned with the optical properties for different excitation configurations. To this end, we performed numerical calculations corresponding to the ones shown in section 6.1.2. However, this time, the direction of incidence was varied as indicated by the inset in figure 6.13. These calculations have been performed by using JCM Suite [83]. The angle of incidence varies between 0° and 40° in steps of 10° . While an angle of 10° mainly influences the conversions, higher angles lead to a profound change in the transmission. In particular, the transmission of light with RCP is affected: The spectrum shows distinct resonances that are similarly pronounced as the resonances for light with LCP. This aspect and the increase of the conversions for higher angles needs to be considered in possible applications [83].

In the context of chiral photonic crystals, a so called bichiral design has been proposed and realized [162] in order to minimize angle dependence. We will evaluate this in the

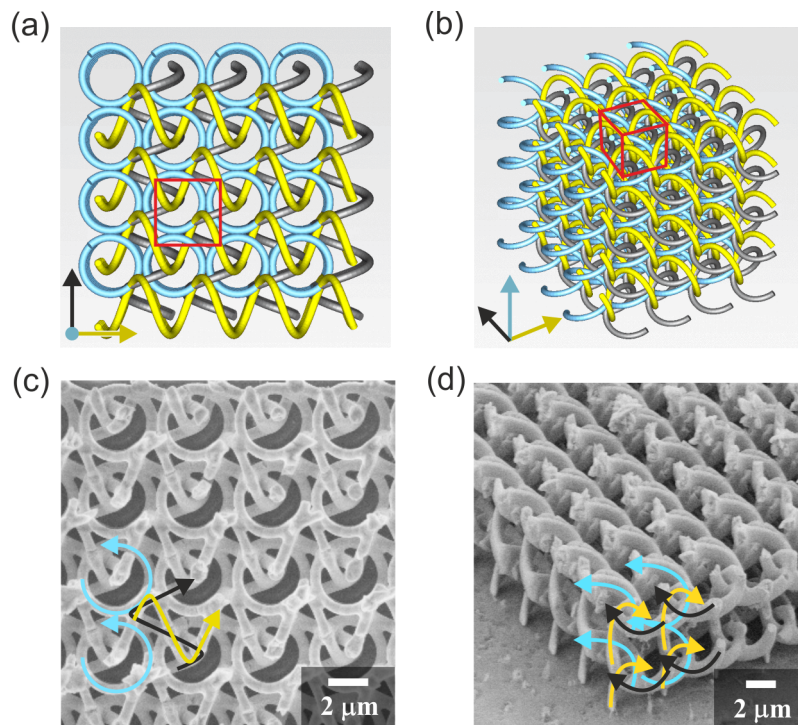


Figure 6.14 (a) Top view, and (b) oblique view of the triaxial helical metamaterial design, where parallel helices have the same color indicated by arrows parallel to the helix axes, and the unit cell is indicated by red lines. (c) Top view, and (d) oblique view of fabricated Au structure. As a guide to the eye, arrows are inserted in the SEM micrographs. The colors correspond to the ones used in figure parts (a) and (b).

context of helical metamaterials in the next part of this section. The strong dependence on the angle of incidence also raises the question of the optical properties of uniaxial helical metamaterials for transversal propagation that we will discuss in the last part of this section.

6.2.1. Triaxial Helical Metamaterials for Oblique Propagation

A possibility to decrease the dependence of the optical properties of helical metamaterials on the angle of incidence could be to use a more isotropic design. Such a design has been realized for polymer helix photonic crystals [162,163]. The idea is to compose a unit cell of three helices with axes along three orthogonal spatial directions, thus a triaxial material. Figure 6.14 (a) and (b) shows the underlying design and also indicates the unit cell used for calculations. A fabricated Au structure is shown in figure 6.14 (c) and (d). Although the height is only approximately two unit cells, measurements of these structures showed a low transmittance (below 0.2) of unpolarized light. Thus, for measurements with a circular polarization with high transmittance, a value below 0.4 is expected. In addition, calculations indicate that the wavelength range of the functionality region is rather small, and, beneath circular dichroism, also high values of conversions are present. Thus, we did

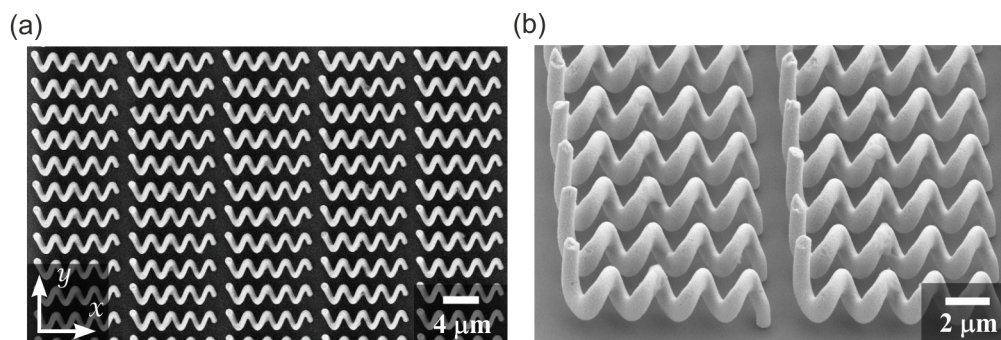


Figure 6.15 Array of helices with helix axes parallel to the glass substrate. (a) Top view, and (b) oblique view.

not further pursue this approach.

Recently, a triaxial Au helix design has been presented [91] that has been fabricated by DLW and electroless plating (as mentioned in section 4.1). There, measurements with a similar setup to ours have shown a functionality region between $3.5 \mu\text{m}$ and $4.5 \mu\text{m}$. The total transmittance was around 0.3 for incident light with RCP and around 0.1 for incident light with LCP. A steady shape of the spectra was reported for incidence angles between 0° (normal incidence) and 15° . Thus, angle dependence can be reduced to some extent by this design, however at the expense of functionality bandwidth and overall transmitted intensity.

6.2.2. Uniaxial Helical Metamaterials for Transversal Propagation

We have seen that helical metamaterials can exhibit strong chiral effects for axial propagation due to higher resonant modes of the helices. We have also seen that the optical properties strongly depend on the angle of incidence. Therefore, we want to discuss the behavior of uniaxial helical metamaterials for transversal propagation in this section. This excitation geometry has also been used in several designs proposed in [164, 165], and designs realized at GHz frequencies [70, 76] that, for example, could be used as broadband optical wave plates.

In order to allow for measurements normal to a glass substrate, the helix axes are parallel to the glass substrate, and one end of each helix is attached to the substrate in our design. Figure 6.15 shows an array of fabricated Au helices with helix axes parallel to the glass substrate and slightly more than four pitches length. The array has a lattice constant of $a_x = 10 \mu\text{m}$ and $a_y = 2.85 \mu\text{m}$ in the respective directions indicated in figure part (a). The helix parameters are $R = 0.8 \mu\text{m}$ and $p = 2.1 \mu\text{m}$.

Optical transmission measurements show that these structures exhibit no circular dichroism. However, differences in the behavior of light with linear polarizations along x - and y -direction are present. Measured and calculated transmittance and reflectance spectra, where the linear polarization of incident light was controlled, are shown in figure 6.16. The calculations have been done by M. Blome and S. Burger (from the Konrad-Zuse-Zentrum für Informationstechnik in Berlin) using JCM Suite. While no pronounced features are visible in the measurable frequency region, calculations indicate a strong linear dichroism

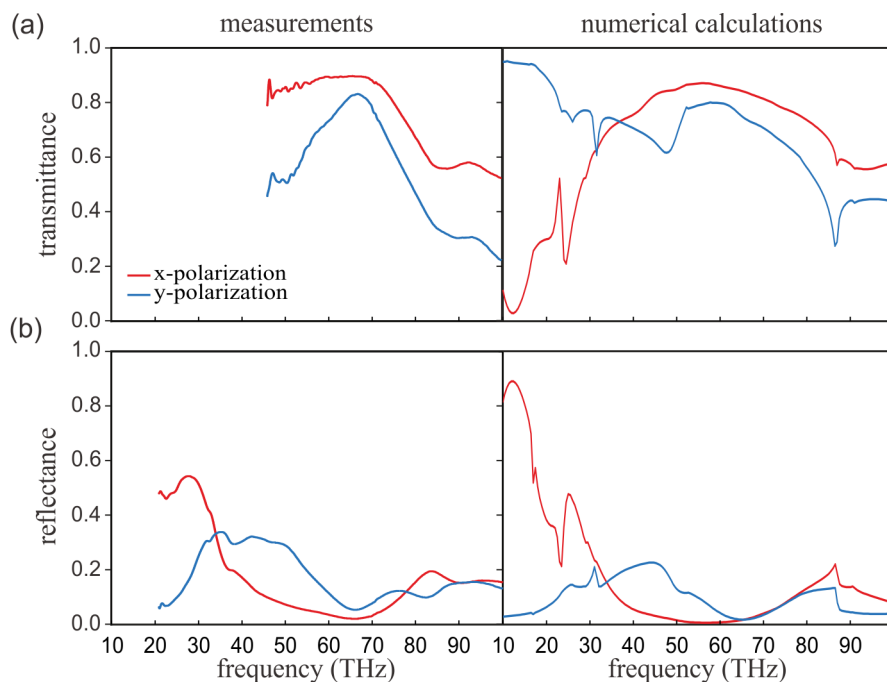


Figure 6.16 Measured and calculated (a) transmittance, and (b) reflectance spectra for incident light with linear polarization along x - (red) or y -direction (blue) with no analyzer behind the sample. For transmission, the conversions are below 0.07 in the calculations and below 0.12 in the measurements (not shown).

around 12 THz. A shift of this resonance to a measurable spectral region is not possible at the moment as the resolution of the used AZ9260 photoresist is not sufficient (even for helices with only one pitch length).

The pronounced resonance at a low frequency is in accordance with radio antenna theory [82]. There, it is stated that emission of light normal to the helix axis is maximal if the wavelength of the incident light is much larger than the size of the helix. It is further said that the polarization state of the emitted light depends on the geometrical parameters of the helix and thus can be linear.

The mentioned lack of circular dichroism is in accordance with radio antenna theory, too: helical radio antennas in the end-fire geometry (where $2\pi R \approx \lambda$) mainly emit and receive circularly polarized light along the helix axis. Thus, no chiral effects are expected for light incident normal to the helix axis for these wavelengths.

6.3. Uniaxial Tapered-Helix Metamaterials

We have shown in section 6.1.3 that square arrays of Au helices can serve as compact broadband circular polarizers. How can the functionality of such devices be improved? In this section, we show by heuristic reasoning supported by numerical calculations that by tapering the helix radius, the bandwidth of the device can realistically be increased to 1.5 octaves [92]. Due to the asymmetry introduced by the tapering, the polarization

conversions are different, depending on the side from which light impinges onto the tapered helices. We will see that this can be used to improve the extinction ratio when the metamaterial is used either as polarizer or as analyzer.

6.3.1. Optical Properties of Uniaxial Tapered-Helix Metamaterials

Intuitively, one might expect increased operation bandwidth when the radius of a helix is gradually increased or decreased along the helix axis (in fact, tapered helices are known as broadband antennas from radio antenna applications [82]). Obviously, the upper bound of the radius is given by the condition that a helix will leave its unit cell and thus could intersect with its neighbors when the sum of the helix diameter and the wire diameter equals the in-plane lattice constant. The ultimate lower bound for the helix radius is given by the wire radius. Together, we have

$$\frac{a}{2} - r > R > r. \quad (6.1)$$

For example, for $r = \frac{a}{8}$ (which is a fairly thin wire), the helix radius can at most be tapered by a factor of three. What increase of bandwidth can we expect from this tapering factor? The bandwidth of a helix with constant radius can be estimated using (2.80). For this case, the relative bandwidth, *i.e.* the ratio between maximum and minimum wavelength, is

$$\frac{\lambda_{\max}}{\lambda_{\min}} = \frac{4}{3} : \frac{3}{4} = \frac{16}{9} \approx 1.8. \quad (6.2)$$

With (2.80) in mind, the relative bandwidth for tapered helices with a tapering factor of three can naively be expected to increase to [92]

$$\frac{\lambda_{\max}}{\lambda_{\min}} = \frac{3 \cdot 4}{3} : \frac{3}{4} = \frac{16}{3} \approx 5. \quad (6.3)$$

To investigate whether this beneficial effect can be transferred to optical frequencies, we have performed numerical calculations. There, it turned out that a quadratical tapering of the radius leads to slightly better results than linear tapering. The helix radius as a function of the height is displayed together with the other geometrical helix parameters in figure 6.17 (a).

By the overall symmetry, four different configurations are possible for left-handed helices as depicted in figure 6.17 (b). Starting from the glass substrate, the helix radius can either increase or decrease, and the light can impinge from either the glass substrate or from the air side. Our numerical calculations showed that the direction of tapering relative to the incident light is important while the direction of tapering relative to the glass substrate only plays a minor role (that may be different though for higher-index substrates like silicon) [92]. Thus, we will discuss helices starting with a small radius at the glass substrate here. For comparison, computational and experimental results for helices with a big radius at the glass substrate are shown in the appendix A.3.

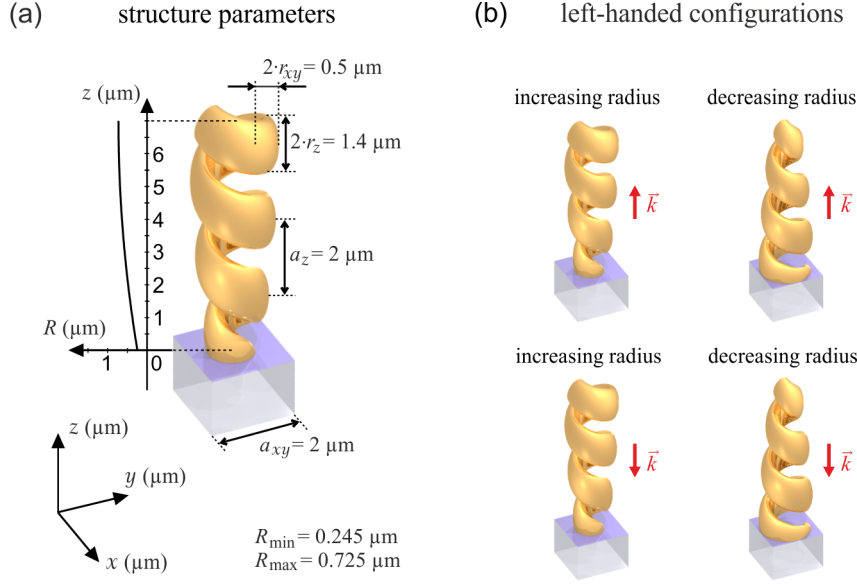


Figure 6.17 (a) Geometrical parameters of tapered helices, and (b) illustration of the possible excitation configurations for a left handed helix on a glass substrate. Light is incident parallel to the helix axis as indicated by the wave vector \vec{k} [92].

The calculated intensity transmittance and conversion spectra for plane waves impinging along the helix axis are shown in figure 6.18. Incident light is impinging either from the glass substrate side or the air side as illustrated by the insets. The transmittance spectra (LCP \rightarrow LCP, and RCP \rightarrow RCP) of the two configurations are symmetric due to reciprocity [52]. However, the conversion spectra (LCP \rightarrow RCP, and RCP \rightarrow LCP) depend on the relative orientation of the direction of the incident light and the taper gradient. This leads to the asymmetric transmission mentioned in section 2.2.3. The conversions behave according to (2.43) and (2.45) (see also [53]).

Depending on the application, both shown configurations can be useful [92]. If one aims at using the device as circular polarizer, *e.g.* for RCP emerging light, LCP should not emerge if possible, regardless whether it stems from transmission of LCP or conversion of RCP. This can be realized with the configuration in figure 6.18 (b). In contrast, when aiming at an analyzer for circular polarization, *e.g.* RCP, with a polarization-insensitive detector behind the metamaterial, one does not care about the emerging polarization. Yet, one does not want LCP \rightarrow LCP or LCP \rightarrow RCP to be significant in magnitude. Such a device can be realized with the configuration in figure 6.18 (a).

The operation bandwidth for the two devices extends from about 30 THz to 90 THz [92]. This translates to a relative bandwidth of 3, *i.e.* about 1.5 octaves. In comparison to untapered but otherwise similar helices like the ones presented in section 6.1.3 [89], this is a significant improvement. We do not achieve the relative bandwidth of 5 from the above naive antenna-theory reasoning, likely because of its simplicity. In addition, the ratio $\frac{\text{RCP} \rightarrow \text{RCP}}{\text{LCP} \rightarrow \text{LCP}}$ is strongly enhanced and exceeds 100 in the range of 37 - 85 THz. The

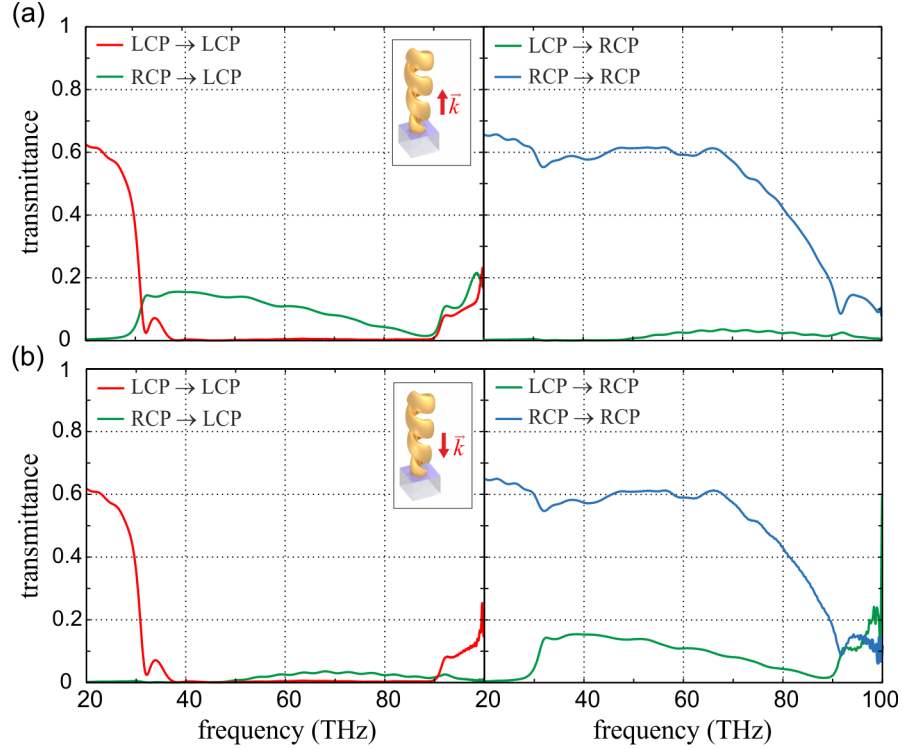


Figure 6.18 Calculated transmittance and conversion spectra for left-handed helices with a small radius at the glass substrate [92].

extinction ratio $\frac{(\text{RCP} \rightarrow \text{RCP}) + (\text{LCP} \rightarrow \text{RCP})}{(\text{LCP} \rightarrow \text{LCP}) + (\text{RCP} \rightarrow \text{LCP})}$, which is relevant for circular polarizer applications, is larger than 10 throughout the entire operation bandwidth and partially exceeds 100 [92]. Due to the asymmetric transmission, the same applies to the extinction ratio $\frac{(\text{RCP} \rightarrow \text{RCP}) + (\text{RCP} \rightarrow \text{LCP})}{(\text{LCP} \rightarrow \text{LCP}) + (\text{LCP} \rightarrow \text{RCP})}$ in the case of an analyzer. For comparison, this ratio barely exceeds 5 for the helices discussed in section 6.1.3. If the number of pitches of these untapered helices is increased to $N = 3.5$, the extinction ratio is merely increased to 6.

6.3.2. Improved Broadband Circular Polarizer

The enormous bandwidth shown in the preceding part of this section by numerical calculations is beyond our present measurement capabilities. Nevertheless, we fabricated Au tapered-helix metamaterials and compared measured spectra to numerical calculations within our measurement specifications. Upon reasonable agreement between experiment and theory, we assume that the actual metamaterial properties correspond to the calculated ones even outside of the experimental limitations.

A fabricated array of left-handed helices with a small radius at the glass substrate is shown in figure 6.19. The geometrical parameters are as depicted in figure 6.17. Measured transmittance spectra of this array are shown together with corresponding calculated spectra for two different excitation configurations as indicated by the insets in figure 6.20. Like for all our measurements, “LCP” corresponds to $(\text{LCP} \rightarrow \text{LCP}) + (\text{LCP} \rightarrow \text{RCP})$ and

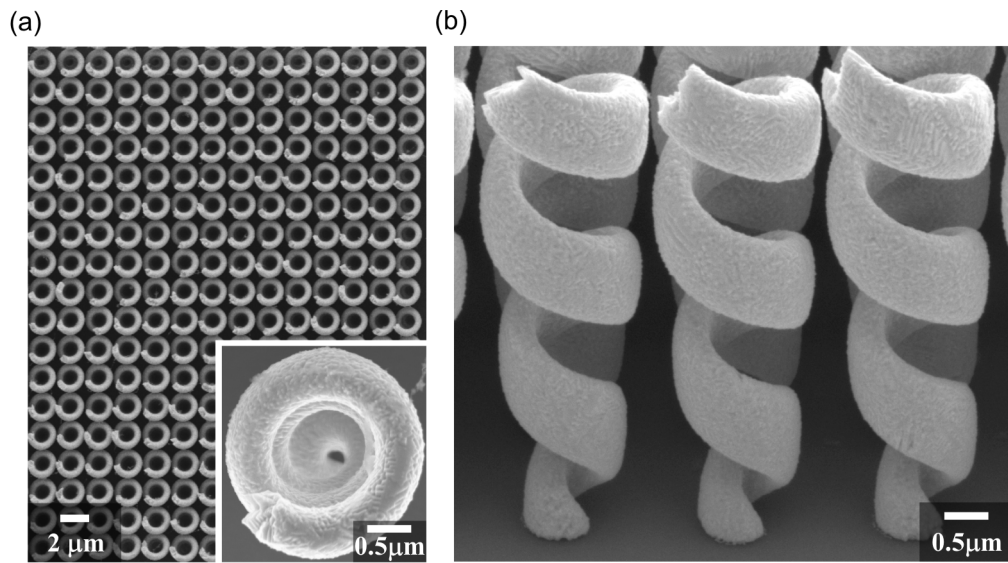


Figure 6.19 Array of fabricated tapered helices. (a) Top view, and (b) oblique view. The inset shows a magnified top view of one helix [92].

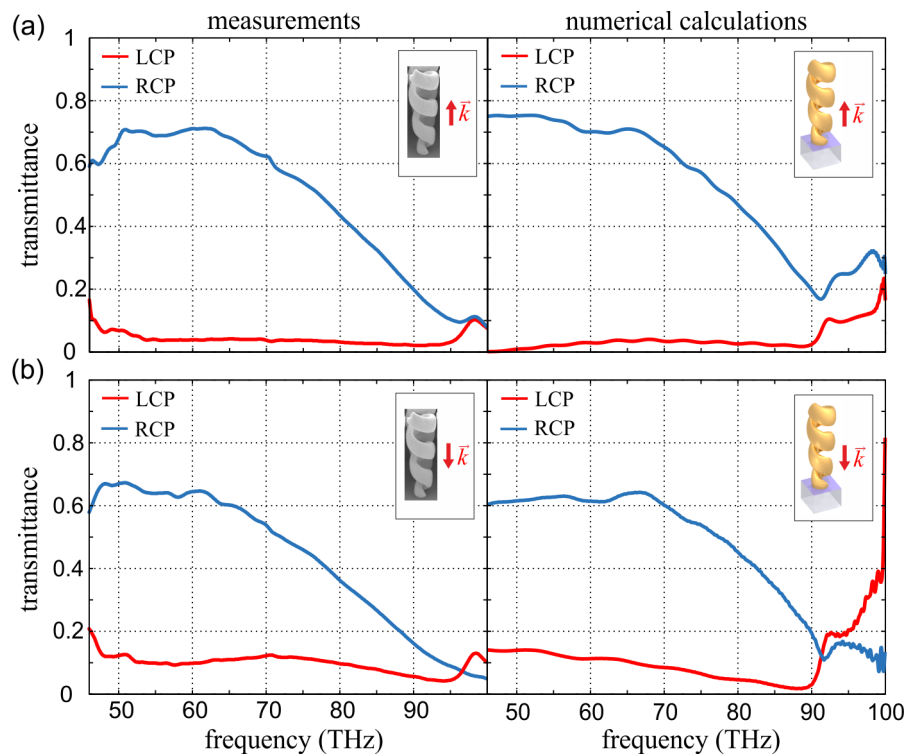


Figure 6.20 Measured and calculated transmittance spectra for light incident normal to the glass substrate with either LCP or RCP and no analyzer behind the sample. The excitation configurations are as indicated in the insets [92].

hence, we can test the functionality of our device as an analyzer. The measured extinction ratio for the configuration in figure 6.20 (a) exceeds 10 throughout almost the entire operation bandwidth. For comparison, fabricated tapered helices with a big radius at the glass substrate and corresponding measured spectra are shown in the appendix A.3.

7. First Steps towards Metal-Dielectric Heterostructures

The combination of DLW and ECD allows to realize many different structure designs as we have shown in sections 4.2 - 4.5 for four materials. However, the range of possible optical properties of the resulting structures could be strongly extended if it would be possible to fabricate electrically disconnected structures normal to a substrate. Cu_2O is a promising candidate for this purpose: it can be deposited using ECD at a constant or low-frequency voltage as it is a semiconductor, and it can be viewed as a dielectric for optical frequencies. In this chapter, we first want to present numerical calculations of Au helices with Cu_2O discontinuities. They unambiguously show the influence of the dielectric on the optical properties of helical metamaterials. In the second part of this chapter, we will discuss our experiments on Cu- Cu_2O heterostructures and possibilities with regard to Au- Cu_2O heterostructures.

7.1. Uniaxial Discontinuous-Helix Metamaterials

What influence can dielectric discontinuities have on the optical properties of helical metamaterials? In order to answer this question, we conducted numerical calculations of arrays of left-handed Au helices. The geometrical parameters are as depicted in figure 6.1, apart from the helices having two pitches height instead of one. Starting with continuous helices, we replaced one or two segments with Cu_2O as indicated in figure 7.1 (a). Due to the 3D representation, the distances for $D = 2$ appear to be different, however they all have the same value. The height of the segments along the z -direction is 200 nm and the Cu_2O is modeled as a dielectric with $n = 2.6$. Light is incident parallel to the helix axis from the air side. The spectra in figure 7.1 (b) reveal a strong influence of the Cu_2O discontinuities on the transmission of light with LCP. Even a pronounced resonance for the transmission of light with RCP appears for $D = 2$, where the helix parts rather resemble tilted split-ring resonators. We also see that the conversions are not changed substantially.

As depicted in figure 6.2 (c) and (d), the broad region of low transmittance of LCP results from the superposition of three current modes with one, two, and three current nodes. These current modes are depicted in figure 7.2 (for reasons of clarity for an Au wire). As Cu_2O is nonconducting for high frequencies, the discontinuities enforce current nodes at their spatial positions as indicated by the dark and light blue lines for $D = 1$ and $D = 2$, respectively. Thus, we would expect that for $D = 1$, the mode with two current nodes is suppressed, while for $D = 2$, the modes with one and three current nodes are suppressed. This behavior is qualitatively reproduced by the spectra in figure 7.1. Thus, by inserting electrical discontinuities in helical metamaterials, one has the possibility to choose which modes can be excited.

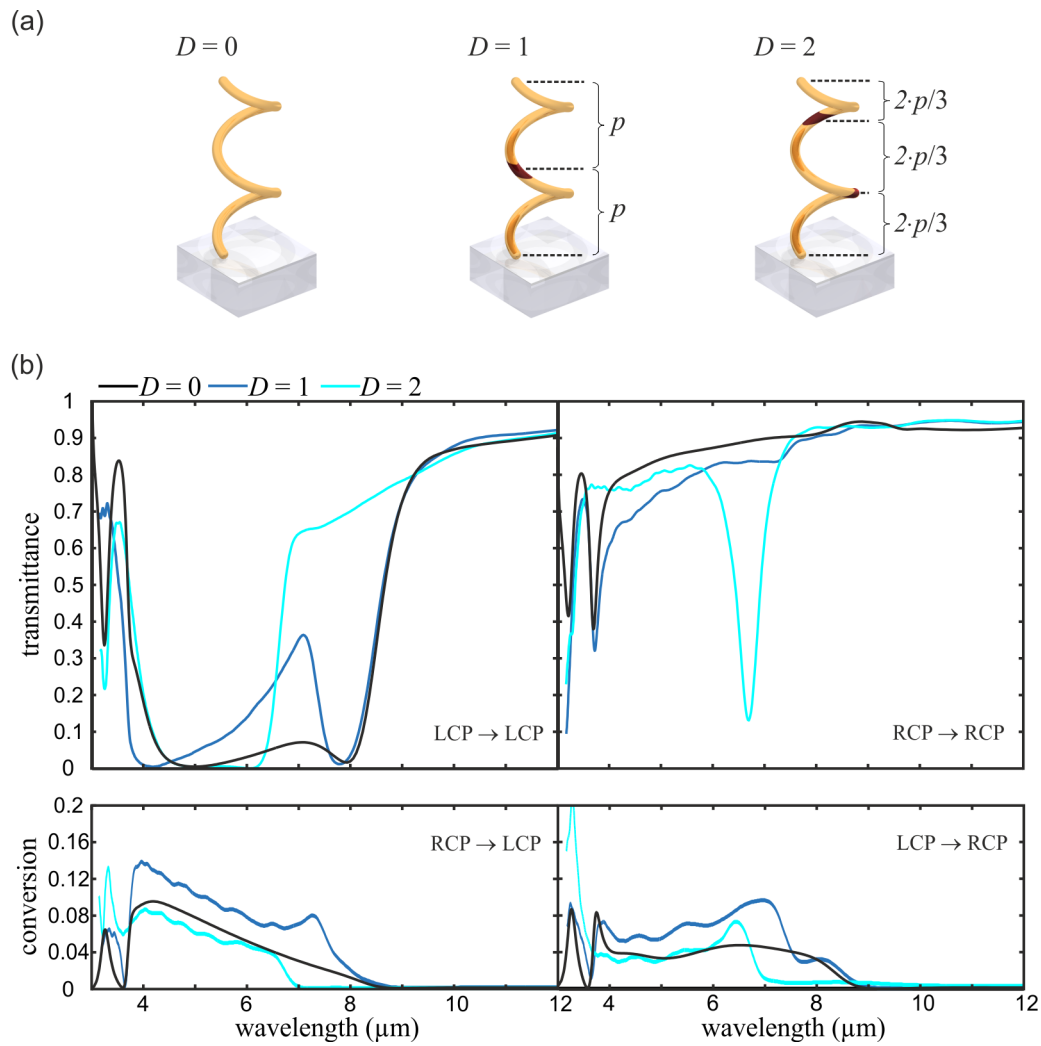


Figure 7.1 (a) Illustration of the unit cells used for numerical calculations with different numbers of discontinuities D , and (b) calculated intensity transmittance and conversion spectra for circularly polarized incident light. The helices are two pitches high, hence the spectra for $D = 0$ are equal to those shown in figure 6.3 for $N = 2$.

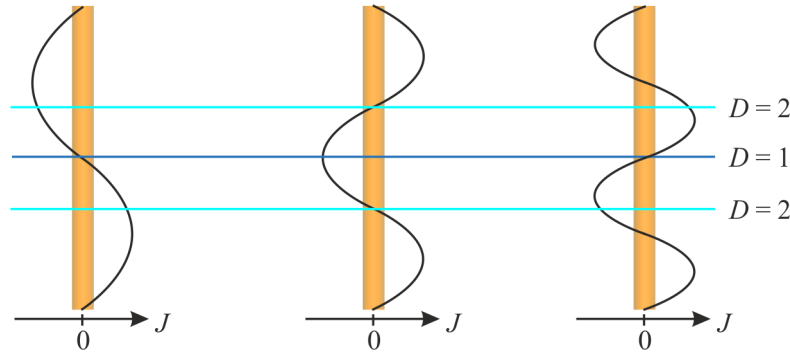


Figure 7.2 Depiction of three current modes for an Au wire corresponding to those in figure 6.2 (d) for a continuous Au helix with two pitches height. The blue lines indicate at which positions a current node would be enforced through the insertion of a dielectric.

7.2. Experimental Approach to Metal-Dielectric Heterostructures

Our approach for the realization of metal-dielectric heterostructures was the alternating deposition of Cu and Cu_2O since this can be done in the same electrolyte solution. This work has been done together with M. Latzel within his diploma thesis.

Both Cu_2O - and Cu-helix arrays can be fabricated as shown in figure 7.3 (a) for the two materials. The geometrical parameters of the helices are $p = 2 \mu\text{m}$, $R = 0.5 \mu\text{m}$, $a = 2 \mu\text{m}$, and a wire thickness similar to previously shown helices. The structure quality is validated by the measured transmittance spectra in figure 7.3 (b). Within the metamaterial limit, we do not see any features in the spectra for Cu_2O as one would expect for a dielectric (the spikes around $4.3 \mu\text{m}$ are due to CO_2 absorption). In contrast, the spectra for Cu show a broadband suppression of light with RCP as the helices are right-handed.

After the fabrication of qualitatively good Cu and Cu_2O structures, the next step was the deposition of heterostructures. Figure 7.4 (a) shows helices with one pitch of Cu_2O on top of one pitch Cu. The interface between the materials is indicated by an arrow as the material contrast is low when viewed in the SEM. A much better contrast is given by a microscope in reflection. There, Cu appears bright as it reflects, while Cu_2O appears dark. Figure 7.4 (b) shows a microscope picture of Cu- Cu_2O rods which are located on the same substrate as the Cu- Cu_2O helices in figure 7.4 (a).

In order to fabricate electrically disconnected metal structures like the helices discussed above, a second layer of Cu needs to be deposited on Cu- Cu_2O structures. However, this could not be realized. Figure 7.4 (c) shows rods which were cut open with a FIB after the deposition of Cu, Cu_2O , and Cu in this order. In case of the left rod, no Cu started to grow in the last ECD step. In case of the other two rods, Cu started to grow. However, for these structures, Cu_2O is visible only near the middle of the rods and is surrounded by a material which has the same contrast as Cu. This can be explained by a reduction

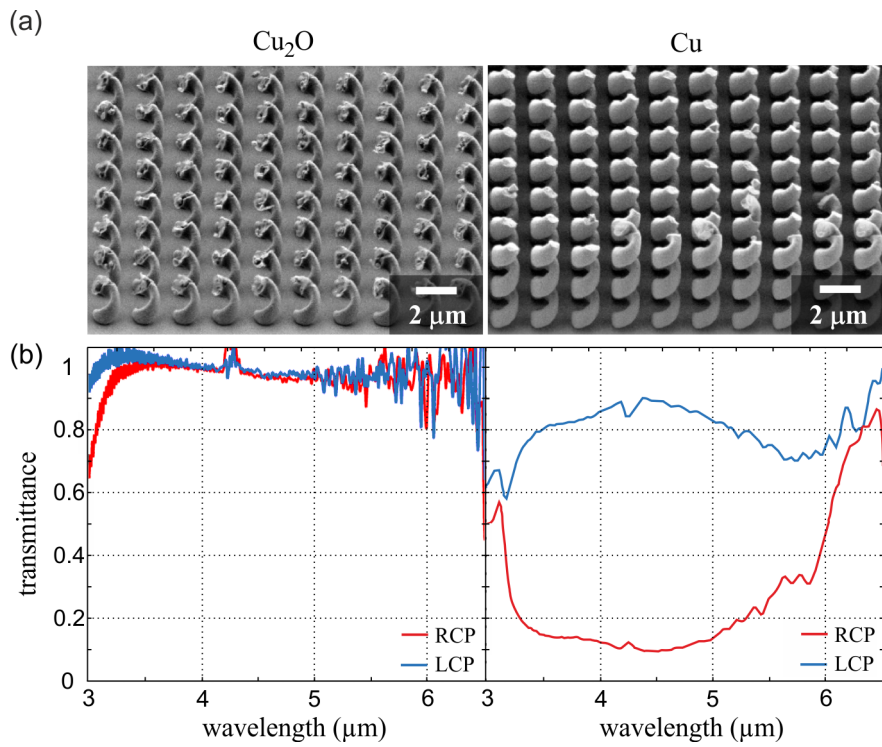


Figure 7.3 (a) SEM micrographs of Cu₂O-helix arrays with one pitch height and of Cu-helix arrays with almost three pitches height. (b) Measured transmittance spectra of the arrays depicted in (a).

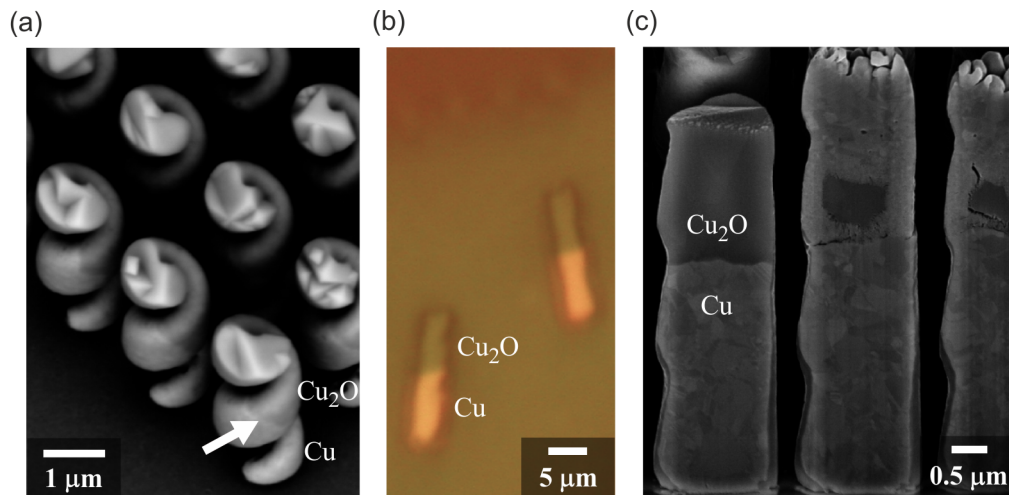
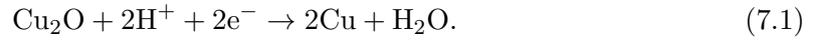


Figure 7.4 (a) SEM micrograph of helices, and (b) microscope picture of rods, both with Cu₂O on top of Cu. (c) SEM micrograph of rods where a second Cu layer was deposited on Cu-Cu₂O structures.

of Cu_2O to Cu according to



This reaction can take place due to the high negative cathode potentials [166] that are necessary for the deposition of Cu. The H^+ ions are presumably delivered by electrolysis of water from the AZ9260 photoresist.

Thus, at least within this experimental setup, the growth of Cu on Cu_2O is not possible. However, one can transfer the fabrication principle to other material systems. For example, the deposition of Au on Cu_2O could be possible as the necessary cathode potential is less negative. Alternatively, other semiconductor materials than Cu_2O might also lead to a successful deposition of heterostructures.

8. Conclusions and Outlook

In conclusion, we have presented our work on helical optical metamaterials in this thesis: design, numerical calculations, development of a suitable fabrication method, optical measurements of realized structures, and discussions of the optical properties. The developed fabrication method combines template fabrication by direct laser writing with an inversion of the templates by using electrochemical deposition. With this method, we have realized three-dimensional structures with versatile designs and feature sizes down to half a micrometer. Our fabricated helical metamaterials show interesting chiral optical properties, in particular a strong and broadband circular dichroism. Hence, they could be used as broadband circular polarizers, yielding an early real-world application for optical metamaterials.

Within this thesis, we devoted chapters 2 and 3 to the fundamentals of both the optical and the electrochemical aspects of this work. In particular, we pointed out the motivation for realization of three-dimensional metamaterials and work that has so far been done in the field of chiral optical metamaterials.

A detailed description of our fabrication method has been given in chapter 4. The starting point are glass substrates, each covered with a layer of indium tin oxide. The layer thickness is optimized for maximal transparency and minimal electrical resistance at the same time. We apply a negative- or a positive-tone photoresist onto these substrates and structure it three-dimensionally by using direct laser writing. In direct laser writing, a laser is focused into a photoresist in such a way that the resist is exposed only in a small region around the focus. This allows for the realization of polymer structures with very versatile three-dimensional designs.

We use such polymer structures as templates for inversion *via* electrochemical deposition of different materials in aqueous solutions. Before the electrochemical deposition, a thorough wetting is necessary to get the electrolyte solution into the submicrometer sized holes in the templates. We achieved optimal wetting by replacing air with carbon dioxide, which can completely dissolve in water, using a self-made setup. Then, the samples are built into one of our electrochemical deposition setups and the templates are inverted. We implemented the deposition of four different materials within our method, namely gold, nickel, copper(I) oxide, and copper. For all materials, we discussed the composition of the electrolyte solution, and the optimal parameters and procedures for the deposition on a macroscopic substrate as well as inside a microscopic polymer template. The main focus was on gold for which we included studies on the design flexibility. After the electrochemical deposition, the photoresists are removed, yielding free-standing three-dimensional structures with feature sizes of half a micrometer.

With this method, we fabricated gold-helix metamaterial arrays and characterized them with the experimental and numerical methods described in chapter 5. The realized structures together with characterization results and discussions of the optical properties have been presented in chapter 6.

In the first part of chapter 6, we numerically investigated uniaxial metamaterial arrays of thin left-handed helices with helix axes normal to the glass substrate and one pitch height. For light with left-circular polarization incident along the helix axis, they have two pronounced resonances within the metamaterial limit, while light with right-circular polarization is mainly transmitted. The two resonances correspond to two current distributions resembling standing waves along the helix wires. The long wavelength current mode is continuous while the short wavelength current mode has one node in the middle of the helix wire.

When the helices have two pitches height, these two resonances reappear, with the current distributions being repeated in the upper pitch. This means that the long wavelength resonance has a current distribution with one node and the short wavelength resonance a current distribution with three nodes. However, a third resonance appears for helices with two pitches height, which has two current nodes. The coupling of these three resonances leads to a broad spectral region of small transmission of light with left-circular polarization and simultaneously high transmission of light with right-circular polarization. The formation of this broad band is similar to discrete atomic levels evolving into broad electronic bands in a crystalline solid. The broadband properties of our helical metamaterials have also been compared to those of helical radio antennas.

We have studied the dependence of the optical properties on geometrical parameters numerically. The most important findings are that the spectral resonance position is mainly determined by the helix radius and that interaction between the single helices cannot be neglected.

In measurements of fabricated uniaxial helical metamaterials, we saw the transition from distinct resonances for helices with one pitch height to a broadband behavior for helices with two pitches height. These structures show strong circular dichroism in a wavelength range spanning almost one octave. Additionally, the extinction ratio between the transmitted and the suppressed circular polarization has a high value of five throughout the functionality bandwidth. Thus, our fabricated helical metamaterials could be used as compact broadband circular polarizers.

We extended this design by superlattices with checkerboard-like configurations of helices with different rotation or handedness to study interactions of the single building blocks in a helical metamaterial. Our measurements showed that a rotation of every other helix by 90° or 180° around the helix axis significantly changes the optical spectra. In particular, spectral regions with a strong suppression of both circular polarizations result. Arrays composed of randomly rotated helices possess smooth spectra without pronounced resonances. We have also found that a racemic mixture leads to equal behavior of light with left- and right-circular polarization.

In the second part of chapter 6, we numerically investigated the dependence of the optical properties of uniaxial helical metamaterials on the angle of incidence. We then

discussed a triaxial design that reduces this dependence, however at the expense of a small bandwidth and a low transmittance. To investigate the optical properties for incidence of light normal to the helix axis, we fabricated arrays of helices with helix axes parallel to the substrate and four pitches length. Interestingly, no circular dichroism was present in this case. Instead, we found pronounced resonances for incident light with a linear polarization which was parallel or perpendicular to the helix axis. This is in accordance with the behavior known from helical radio antennas.

In the last part of chapter 6, we presented an uniaxial tapered-helix metamaterial that was pre-designed for use as an improved circular polarizer. Through a tapering of the helix radius along the helix axis, the functionality bandwidth is enlarged. In addition, the geometrical shape leads to an asymmetric transmission that is used to increase the extinction ratio. In our measurements, the extinction ratio was improved by a factor of two in comparison to our metamaterial design with untapered helices throughout almost the entire functionality bandwidth.

With our present method, three-dimensional structures with versatile designs and feature sizes of half a micrometer have been fabricated. Future developments on the fabrication side could lead to an even larger variety of realizable structure designs.

By depositing materials which act as dielectrics at optical frequencies, electrical discontinuities in metal structures could be realized. We have proposed an experimental route for the realization of such metal-dielectric heterostructures and taken first steps on it (section 7.1).

Another improvement of our fabrication method would be to achieve a better resolution, for example through combination with isotropic layer deposition methods [167, 168] or through direct laser writing with enhanced resolution [133–136]. This would allow to realize helical metamaterial designs in the visible spectral region, and more complicated unit cells within a measurable wavelength range.

We have discussed the optical properties of our helical metamaterials for different geometries. The uniaxial design shows a strong and broadband circular dichroism and could yield an alternative to the usually wavelength-dependent wave plates, particularly for the infrared spectral region where suitable optical components are often hard to find. Another interesting aspect of such metamaterial devices is their small size and the possibility to incorporate them into miniature optical systems.

Yet there are many further helical designs to explore: centimeter wave realizations of wave plates [70] and chiral metamaterials with a negative refractive index [72–76] could be transferred to optical frequencies. There are also many interesting designs known from helical radio antennas that could be transferred to the optical regime, like multifilar structures with several helices in one unit cell [82]. Numerical calculations have shown that this leads to circular dichroism with improved bandwidth and extinction ratio in comparison to a design with one helix per unit cell [169, 170]. One could also utilize the mechanical properties of helices. For example, mechanically tunable plasmon resonances have been reported in a microwave experiment [171]. The incorporation of electrical discontinuities into metal structures would further enlarge the design possibilities as our numerical studies

of discontinuous helices have unambiguously shown (section 7.2). With these possibilities at hand, future helical designs can yield fascinating optical properties and thus contribute to the vivid field of photonics.

A. Appendix

A.1. Wave Propagation in Chiral Media — Additional Equations

Derivation of the relation between the material parameters in the wavefield description: Through equating the right sides of (2.63) and (2.64), we get

$$\frac{\kappa^2}{c_0^2} \frac{1}{\varepsilon_0 \mu_0} = (\mu - \mu_{\pm})(\varepsilon - \varepsilon_{\pm}), \quad (\text{A.1})$$

$$\kappa^2 = (\mu - \mu_{\pm})(\varepsilon - \varepsilon_{\pm}). \quad (\text{A.2})$$

Replacing both \vec{E}_{\pm} and \vec{H}_{\pm} in (2.65) by (2.63), we get

$$i \frac{\kappa}{c_0 \varepsilon_0} \frac{1}{\varepsilon - \varepsilon_{\pm}} \nabla \times \vec{H}_{\pm} = i \omega \mu_0 \mu_{\pm} \frac{c_0 \varepsilon_0 (\varepsilon - \varepsilon_{\pm})}{i \kappa} \vec{E}_{\pm}. \quad (\text{A.3})$$

We replace $\nabla \times \vec{H}_{\pm}$ using (2.67) and solve for κ^2 :

$$-i \omega \varepsilon_0 \varepsilon_{\pm} i \frac{\kappa}{c_0 \varepsilon_0} \frac{1}{\varepsilon - \varepsilon_{\pm}} \vec{E}_{\pm} = \omega \mu_0 c_0 \varepsilon_0 \frac{\mu_{\pm} (\varepsilon - \varepsilon_{\pm})}{\kappa} \vec{E}_{\pm}, \quad (\text{A.4})$$

$$\frac{\kappa^2}{c_0^2} \frac{1}{\varepsilon_0 \mu_0} = \frac{\varepsilon - \varepsilon_{\pm}}{\varepsilon_{\pm}} \mu_{\pm} (\varepsilon - \varepsilon_{\pm}), \quad (\text{A.5})$$

$$\kappa^2 = \frac{\mu_{\pm}}{\varepsilon_{\pm}} (\varepsilon - \varepsilon_{\pm})^2. \quad (\text{A.6})$$

Inserting (A.2) in (A.6), we get

$$\mu - \mu_{\pm} = \frac{\mu_{\pm}}{\varepsilon_{\pm}} (\varepsilon - \varepsilon_{\pm}), \quad (\text{A.7})$$

$$\frac{\mu}{\mu_{\pm}} - 1 = \frac{\varepsilon}{\varepsilon_{\pm}} - 1, \quad (\text{A.8})$$

$$\frac{\varepsilon_{\pm}}{\varepsilon} = \frac{\mu_{\pm}}{\mu}, \quad (\text{A.9})$$

$$\varepsilon_{\pm} = \varepsilon \frac{\mu_{\pm}}{\mu}. \quad (\text{A.10})$$

This can be used to replace ε_{\pm} in (A.2). Then we are able to get solutions for μ_{\pm} :

$$\kappa^2 = (\mu - \mu_{\pm}) \frac{\varepsilon}{\mu} (\mu - \mu_{\pm}), \quad (\text{A.11})$$

$$(\mu_{\pm} - \mu)^2 - \frac{\mu}{\varepsilon} \kappa^2 = 0, \quad (\text{A.12})$$

$$(\mu_{\pm} - \mu - \frac{\mu}{\sqrt{\mu\varepsilon}}\kappa)(\mu_{\pm} - \mu + \frac{\mu}{\sqrt{\mu\varepsilon}}\kappa) = 0. \quad (\text{A.13})$$

This quadratic equation has the two solutions

$$\mu_{\pm} = \mu(1 \pm \frac{1}{\sqrt{\mu\varepsilon}}\kappa). \quad (\text{A.14})$$

The expression for ε_{\pm} follows directly when inserting (A.14) into (A.10):

$$\varepsilon_{\pm} = \varepsilon(1 \pm \frac{1}{\sqrt{\mu\varepsilon}}\kappa). \quad (\text{A.15})$$

A.2. Process Parameters of the used Photoresists

In the following two tables, the process parameters for AZ9260 and SU8 are given. The terms soft bake, post bake, and hard bake denote a baking step on a hot plate before DLW, after DLW, and after development, respectively.

AZ9260

The process parameters for a thickness of the AZ9260 photoresist of 9 μm and 20 μm are given in table A.1.

Table A.1 Process parameters for AZ9260 with a film thickness of 9 μm and 20 μm .
(*use oven instead of hot plate)

	9 μm	20 μm , step 1	20 μm , step 2
spin coating (speed, duration)	300 $\frac{1}{\text{min}}$, 10 s, then 2400 $\frac{1}{\text{min}}$, 60 s	300 $\frac{1}{\text{min}}$, 10 s, then 2400 $\frac{1}{\text{min}}$, 60 s	300 $\frac{1}{\text{min}}$, 10 s, then 2100 $\frac{1}{\text{min}}$, 60 s
soft bake (temperature, duration)	110°C, 195 s	110°C, 96 s	110°C, 8 min*
rehydration (humidity, duration)	60%, 1 h	-	60%, 1 h
development (duration)	30 min	-	30 min

SU8

Table A.2 gives the process parameters for a film thickness of 20 μm using SU8-25 and a thickness of 100 μm using SU8-100.

Table A.2 Process parameters for a film thickness of 20 μm using SU8-25 and 100 μm using SU8-100 (*use oven instead of hot plate).

	SU8-25	SU8-100
spin coating (speed, duration)	600 $\frac{1}{\text{min}}$, 10 s, then 2200 $\frac{1}{\text{min}}$, 33 s	500 $\frac{1}{\text{min}}$, 13 s, then 3500 $\frac{1}{\text{min}}$, 38 s
soft bake (temperature, duration)	95°C, 7 min	65°C, 10 min, then 65°C \rightarrow 95°C, 30 min
post bake (temperature, duration)	65°C \rightarrow 95°C, 7 min	65°C, 1 min, then 65°C \rightarrow 95°C, 10 min*
development (duration)	8 min	20 – 25 min
flush with isopropyl (duration)	90 s	60 s
hard bake (temperature, duration)	180°C, 15 min, then 180°C \rightarrow 40°C, 2 h	180°C, 15 min, then 180°C \rightarrow 40°C, 2 h

A.3. Supplementary Results on Uniaxial Tapered-Helix Metamaterials

For comparison, we want to discuss helices starting with a big radius at the glass substrate here. Calculated intensity transmittance and conversion spectra for plane waves impinging along the helix axis are shown in figure A.1. While the shape of the spectra is slightly different to those in figure 6.18, we can clearly see that the overall behavior depends on the orientation of the tapering relative to the propagation direction of the incident light. The differences in the shapes of the spectra in figure 6.18 and figure A.1 are most likely due to different parts of the helices being cut away because of the glass substrate.

Figure A.2 shows SEM micrographs of fabricated Au helices with a big radius at the glass substrate. Measured transmittance spectra of this array are shown in figure A.3 together with corresponding calculated spectra. The insets indicate the used excitation configurations.

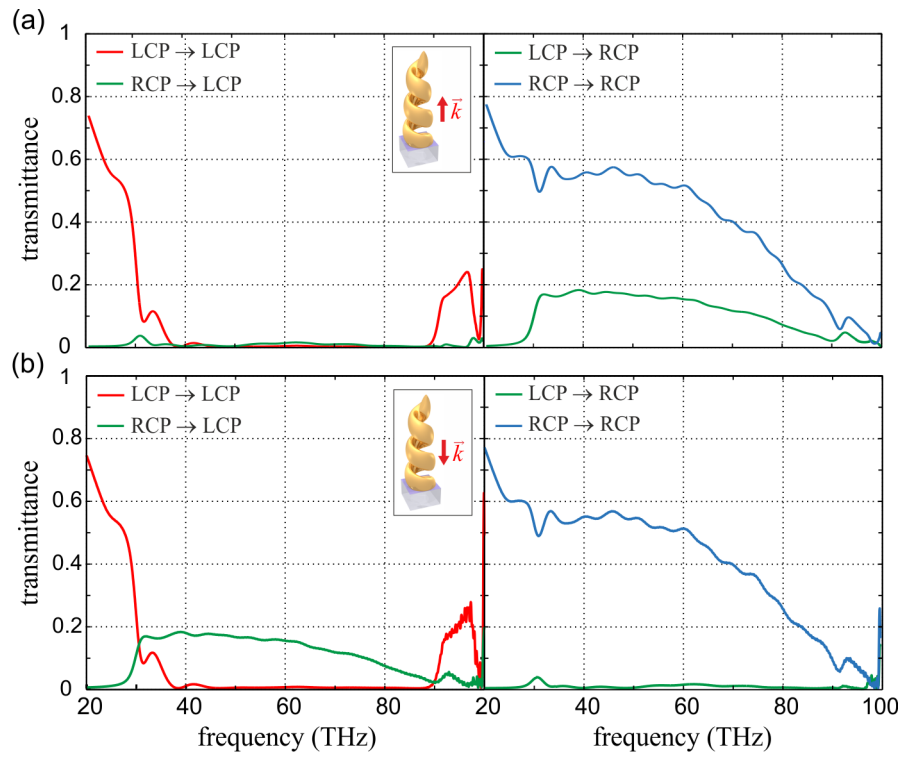


Figure A.1 Calculated transmittance and conversion spectra for left-handed helices with a big radius at the glass substrate

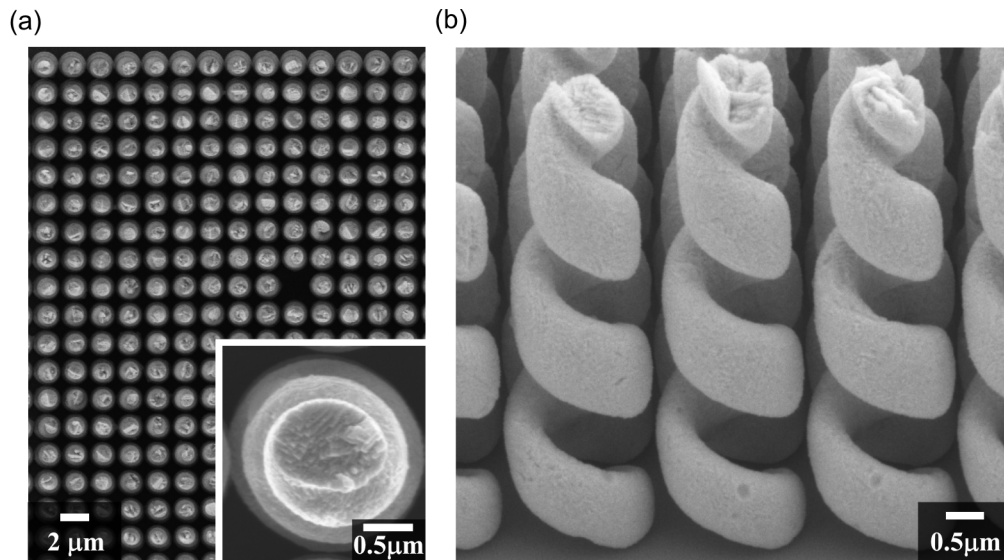


Figure A.2 Array of fabricated tapered helices. (a) Top view, and (b) oblique view. The inset shows a magnified top view of one helix.

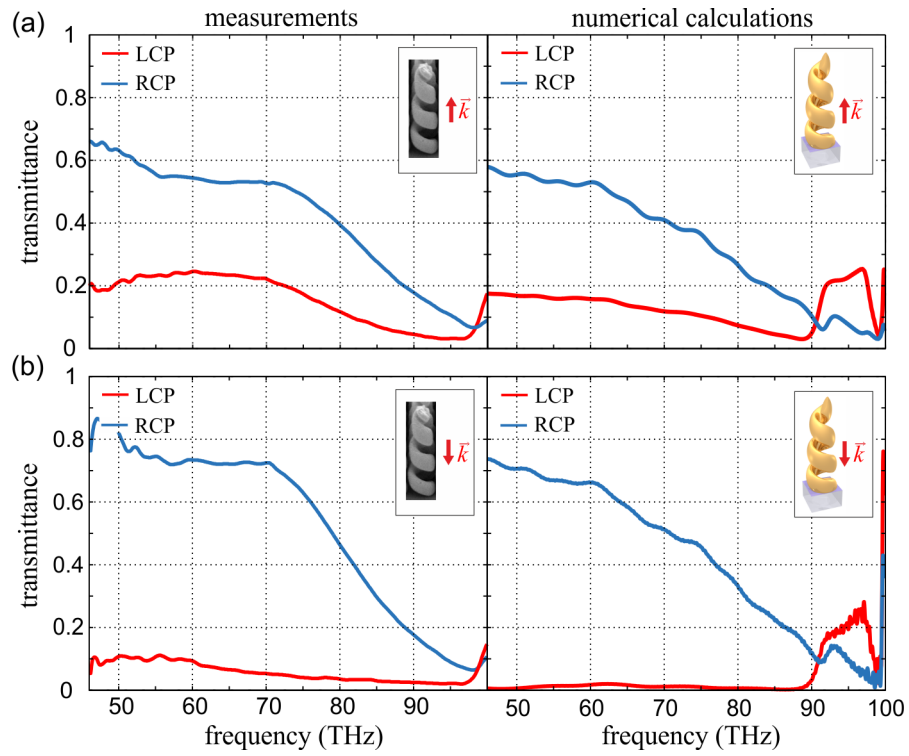


Figure A.3 Measured and calculated transmittance spectra for the excitation configurations indicated in the insets. Light is incident normal to the glass substrate with either LCP or RCP and no analyzer is present behind the sample.

Bibliography

- [1] W. T. Lord Kelvin, *Baltimore lectures on molecular dynamics and the wave theory of light* (C. J. Clay and Sons, 1904).
- [2] L. Pasteur, “Recherches sur les relations qui peuvent exister entre la forme cristalline et la composition chimique, et le sens de la polarisation rotatoire,” *Ann. Chim. Phys.* **24**, 442 (1848).
- [3] P. Drude, *Lehrbuch der Optik* (S. Hirzel, 1906).
- [4] K. F. Lindman, “Über eine durch ein isotropes System von spiralförmigen Resonatoren erzeugte Rotationspolarisation der elektromagnetischen Wellen,” *Ann. Phys.* **368**, 621 (1920).
- [5] J. B. Pendry, A. J. Holden, D. J. Robbins, and W. J. Stewart, “Magnetism from Conductors and Enhanced Nonlinear Phenomena,” *IEEE Trans. Microwave Theory Tech.* **47**, 2075 (1999).
- [6] S. Linden, C. Enkrich, M. Wegener, J. Zhou, T. Koschny, and C. M. Soukoulis, “Magnetic Response of Metamaterials at 100 Terahertz,” *Science* **306**, 1351 (2004).
- [7] C. Enkrich, M. Wegener, S. Linden, S. Burger, L. Zschiedrich, F. Schmidt, J. F. Zhou, T. Koschny, and C. M. Soukoulis, “Magnetic Metamaterials at Telecommunication and Visible Frequencies,” *Phys. Rev. Lett.* **95**, 203901 (2005).
- [8] V. G. Veselago, “The electrodynamics of substances with simultaneously negative values of ϵ and μ ,” *Sov. Phys. Usp.* **10**, 509 (1968).
- [9] R. A. Shelby, D. R. Smith, and S. Schultz, “Experimental Verification of a Negative Index of Refraction,” *Science* **292**, 77 (2001).
- [10] S. Zhang, W. Fan, N. C. Panoiu, K. J. Malloy, R. M. Osgood, and S. R. J. Brueck, “Experimental Demonstration of Near-Infrared Negative-Index Metamaterials,” *Phys. Rev. Lett.* **95**, 137404 (2005).
- [11] G. Dolling, C. Enkrich, M. Wegener, C. M. Soukoulis, and S. Linden, “Simultaneous Negative Phase and Group Velocity of Light in a Metamaterial,” *Science* **312**, 892 (2006).
- [12] J. B. Pendry, “Negative Refraction Makes a Perfect Lens,” *Phys. Rev. Lett.* **85**, 3966 (2000).
- [13] U. Leonhardt, “Optical Conformal Mapping,” *Science* **312**, 1777 (2006).

- [14] J. B. Pendry, D. Schurig, and D. R. Smith, "Controlling Electromagnetic Fields," *Science* **312**, 1780 (2006).
- [15] T. Ergin, N. Stenger, P. Brenner, J. B. Pendry, and M. Wegener, "Three-Dimensional Invisibility Cloak at Optical Wavelengths," *Science* **328**, 337 (2010).
- [16] J. B. Pendry, "A Chiral Route to Negative Refraction," *Science* **306**, 1353 (2004).
- [17] A. Papakostas, A. Potts, D. M. Bagnall, S. L. Prosvirnin, H. J. Coles, and N. I. Zheludev, "Optical Manifestations of Planar Chirality," *Phys. Rev. Lett.* **90**, 107404 (2003).
- [18] M. Kuwata-Gonokami, N. Saito, Y. Ino, M. Kauranen, K. Jefimovs, T. Vallius, J. Turunen, and Y. Svirko, "Giant Optical Activity in Quasi-Two-Dimensional Planar Nanostructures," *Phys. Rev. Lett.* **95**, 227401 (2005).
- [19] M. Decker, M. W. Klein, M. Wegener, and S. Linden, "Circular dichroism of planar chiral magnetic metamaterials," *Opt. Lett.* **32**, 856 (2007).
- [20] M. Decker, M. Ruther, C. E. Kriegler, J. Zhou, C. M. Soukoulis, S. Linden, and M. Wegener, "Strong optical activity from twisted-cross photonic metamaterials," *Opt. Lett.* **34**, 2501 (2009).
- [21] M. Decker, R. Zhao, C. M. Soukoulis, S. Linden, and M. Wegener, "Twisted splitting-resonator photonic metamaterial with huge optical activity," *Opt. Lett.* **35**, 1593 (2010).
- [22] C. Helgert, E. Pshenay-Severin, M. Falkner, C. Menzel, C. Rockstuhl, E.-B. Kley, A. Tünnermann, F. Lederer, and T. Pertsch, "Chiral Metamaterial Composed of Three-Dimensional Plasmonic Nanostructures," *Nano Lett.* **11**, 4400 (2011).
- [23] S. Maruo, O. Nakamura, and S. Kawata, "Three-dimensional microfabrication with two-photon-absorbed photopolymerization," *Opt. Lett.* **22**, 132 (1997).
- [24] G. von Freymann, A. Ledermann, M. Thiel, I. Staude, S. Essig, K. Busch, and M. Wegener, "Three-Dimensional Nanostructures for Photonics," *Adv. Funct. Mater.* **20**, 1038 (2010).
- [25] M. Thiel, J. K. Gansel, M. Wegener, and G. von Freymann, "Wenn das Licht den Dreh raus hat. Künstliche chirale Materialien," *Phys. Unserer Zeit* **42**, 70 (2011).
- [26] N. Dambrowsky and J. Schulz, "Goldgalvanik in der Mikrosystemtechnik, Herausforderungen durch neue Anwendungen," *Forschungszentrum Karlsruhe in der Helmholtz-Gemeinschaft, Wissenschaftliche Berichte* p. 7308 (2007).
- [27] E. Hecht, *Optik* (Oldenbourg Verlag, München Wien, 2001), 3rd ed.
- [28] B. E. A. Saleh and M. C. Teich, *Fundamentals of Photonics* (John Wiley & Sons, New York, 2007), 2nd ed.

-
- [29] J. D. Jackson, *Classical Electrodynamics* (John Wiley & Sons, New York, 1999), 3rd ed.
- [30] M. Born and E. Wolf, *Principles of optics : electromagnetic theory of propagation, interference and diffraction of light* (Cambridge University Press, 2006), 7th ed.
- [31] I. V. Lindell, A. H. Sihvola, S. A. Tretyakov, and A. J. Viitanen, *Electromagnetic Waves in Chiral and Bi-Isotropic Media* (Artech House, Boston London, 1994).
- [32] J. A. Kong, *Electromagnetic Wave Theory* (John Wiley & Sons, New York, 1986).
- [33] M. A. Ordal, L. L. Long, R. J. Bell, S. E. Bell, R. R. Bell, R. W. Alexander, and C. A. Ward, "Optical properties of the metals: Al, Co, Cu, Au, Fe, Pb, Ni, Pd, Pt, Ag, Ti, and W in the infrared and far infrared," *Appl. Opt.* **22**, 1099 (1983).
- [34] P. B. Johnson and R. W. Christy, "Optical Constants of the Noble Metals," *Phys. Rev. B* **6**, 4370 (1972).
- [35] M. A. Ordal, R. J. Bell, R. W. Alexander, L. L. Long, and M. R. Querry, "Optical properties of fourteen metals in the infrared and far infrared: Al, Co, Cu, Au, Fe, Pb, Mo, Ni, Pd, Pt, Ag, Ti, V, and W," *Appl. Opt.* **24**, 4493 (1985).
- [36] P. B. Johnson and R. W. Christy, "Optical constants of transition metals: Ti, V, Cr, Mn, Fe, Co, Ni and Pd," *Phys. Rev. B* **9**, 5056 (1974).
- [37] P. Biagioni, J.-S. Huang, and B. Hecht, "Nanoantennas for visible and infrared radiation," arXiv:1103.1568v2 (2011).
- [38] C. A. Kyriazidou, H. F. Contopanagos, W. M. Merrill, and N. G. Alexopoulos, "Artificial versus Natural Crystals: Effective Wave Impedance of Printed Photonic Bandgap Materials," *IEEE Trans. Antennas Propag.* **48**, 95 (2000).
- [39] C. R. Simovski and S. A. Tretyakov, "Local constitutive parameters of metamaterials from an effective-medium perspective," *Phys. Rev. B* **75**, 195111 (2007).
- [40] M. S. Rill, "Three-Dimensional Photonic Metamaterials by Direct Laser Writing and Advanced Metallization Techniques," Ph.D. thesis (2010).
- [41] A. Alù, "Restoring the physical meaning of metamaterial constitutive parameters," *Phys. Rev. B* **83**, 081102 (2011).
- [42] D. R. Smith, D. C. Vier, T. Koschny, and C. M. Soukoulis, "Electromagnetic parameter retrieval from inhomogeneous metamaterials," *Phys. Rev. E* **71**, 036617 (2005).
- [43] G. Mie, "Beiträge zur Optik trüber Medien, speziell kolloidaler Metallösungen," *Ann. Phys.* **25**, 377 (1908).
- [44] W. N. Hardy and L. A. Whitehead, "Split-ring resonator for use in magnetic resonance from 200-2000 MHz," *Rev. Sci. Instrum.* **52**, 213 (1981).

- [45] K. Busch, G. von Freymann, S. Linden, S. F. Mingaleev, L. Tkeshelashvili, and M. Wegener, “Periodic nanostructures for photonics,” *Phys. Rep.* **444** (2007).
- [46] G. Dolling, M. Wegener, and S. Linden, “Realization of a three-functional-layer negative-index photonic metamaterial,” *Optics Lett.* **32**, 551 (2007).
- [47] J. Valentine, S. Zhang, T. Zentgraf, E. Ulin-Avila, D. A. Genov, G. Bartal, and X. Zhang, “Three-dimensional optical metamaterial with a negative refractive index,” *Nature* **455**, 376 (2008).
- [48] N. Liu, H. Guo, L. Fu, S. Kaiser, H. Schweizer, and H. Giessen, “Three-dimensional photonic metamaterials at optical frequencies,” *Nat. Mater.* **7**, 31 (2008).
- [49] T. Koschny, L. Zhang, and C. M. Soukoulis, “Isotropic three-dimensional left-handed metamaterials,” *Phys. Rev. B* **71**, 121103 (2005).
- [50] A. Andryieuski, C. Menzel, C. Rockstuhl, R. Malureanu, and A. V. Lavrinenko, “The split cube in a cage: bulk negative-index material for infrared applications,” *J. Opt. A: Pure Appl. Opt.* **11**, 114010 (2009).
- [51] D. O. Güney, T. Koschny, M. Kafesaki, and C. M. Soukoulis, “Connected bulk negative index photonic metamaterials,” *Opt. Lett.* **34**, 506 (2009).
- [52] R. J. Potton, “Reciprocity in optics,” *Rep. Prog. Phys.* **67**, 717 (2004).
- [53] C. Menzel, C. Helgert, C. Rockstuhl, E.-B. Kley, A. Tünnermann, T. Pertsch, and F. Lederer, “Asymmetric Transmission of Linearly Polarized Light at Optical Metamaterials,” *Phys. Rev. Lett.* **104**, 253902 (2010).
- [54] A. S. Schwanecke, V. A. Fedotov, V. V. Khardikov, S. L. Prosvirnin, Y. Chen, and N. I. Zheludev, “Nanostructured Metal Film with Asymmetric Optical Transmission,” *Nano Lett.* **8**, 2940 (2008).
- [55] Greek-English Translator, <http://www.kypros.org/cgi-bin/lexicon> (2012).
- [56] S. A. Tretyakov, A. H. Sihvola, A. A. Sochava, and C. R. Simovski, “Magnetolectric Interactions in Bi-Anisotropic Media,” *Journal of Electromagnetic Waves and Applications* **12**, 481 (1998).
- [57] D. N. Astrov, *Soviet Phys. JETP* **11**, 708 (1960).
- [58] M. Wegener and S. Linden, *Bianisotropic and Chiral Metamaterials*, Chapter in *Tutorials in Metamaterials* edited by M. A. Noginov and V. A. Podolskiy, Series in Nano-optics and Nanophotonics (Taylor & Francis Group, 2012).
- [59] X. Chen, B.-I. Wu, J. A. Kong, and T. M. Grzegorzcyk, “Retrieval of the effective constitutive parameters of bianisotropic metamaterials,” *Phys. Rev. E* **71**, 046610 (2005).

-
- [60] M. S. Rill, C. Plet, M. Thiel, I. Staude, G. von Freymann, S. Linden, and M. Wegener, "Photonic metamaterials by direct laser writing and silver chemical vapour deposition," *Nat. Mater.* **7**, 543 (2008).
- [61] C. E. Kriegler, M. S. Rill, M. Thiel, E. Müller, S. Essig, A. Frölich, G. von Freymann, S. Linden, D. Gerthsen, H. Hahn, K. Busch, and M. Wegener, "Transition between corrugated metal films and split-ring-resonator arrays," *Appl. Phys. B* **96**, 749 (2009).
- [62] Z. Li, K. Aydin, and E. Ozbay, "Determination of the effective constitutive parameters of bianisotropic metamaterials from reflection and transmission coefficients," *Phys. Rev. E* **79**, 026610 (2009).
- [63] I. V. Lindell and A. J. Viitanen, "Eigenwaves in the general uniaxial bianisotropic medium with symmetric parameter dyadics," *Progress in Electromagnetics Research* **9**, 1 (1994).
- [64] S. A. Tretyakov and A. A. Sochava, "Reflection and Transmission of Plane Electromagnetic Waves in Uniaxial Bianisotropic Materials," *Int. J. Infrared Millimeter Waves* **15**, 829 (1994).
- [65] I. V. Lindell and A. J. Viitanen, "Plane Wave Propagation in Uniaxial Bianisotropic Medium," *Electron. Lett.* **29**, 150 (1993).
- [66] A. J. Viitanen and I. V. Lindell, "Plane wave propagation in a uniaxial bianisotropic medium with an application to a polarization transformer," *Int. J. Infrared Millimeter Waves* **14**, 1993 (1993).
- [67] S. He, "Wave propagation through a dielectric-uniaxial bianisotropic interface and the computation of Brewster angles," *J. Opt. Soc. Am. A* **10**, 2402 (1993).
- [68] P. A. Belov, C. R. Simovski, and S. A. Tretyakov, "Example of bianisotropic electromagnetic crystals: The spiral medium," *Phys. Rev. E* **67**, 056622 (2003).
- [69] M. G. Silveirinha, "Design of Linear-to-Circular Polarization Transformers Made of Long Densely Packed Metallic Helices," *IEEE Trans. Antennas Propag.* **56**, 390 (2008).
- [70] C. Wu, H. Li, X. Yu, F. Li, H. Chen, and C. T. Chan, "Metallic Helix Array as a Broadband Wave Plate," *Phys. Rev. Lett.* **107**, 177401 (2011).
- [71] I. V. Lindell, A. J. Viitanen, and P. K. Koivisto, "Plane-wave propagation in a transversely bianisotropic uniaxial medium," *Microw. Opt. Technol. Lett.* **6**, 478 (1993).
- [72] S. Zhang, Y.-S. Park, J. Li, X. Lu, W. Zhang, and X. Zhang, "Negative Refractive Index in Chiral Metamaterials," *Phys. Rev. Lett.* **102**, 023901 (2009).

- [73] E. Plum, J. Zhou, J. Dong, V. A. Fedotov, T. Koschny, C. M. Soukoulis, and N. I. Zheludev, "Metamaterial with negative index due to chirality," *Phys. Rev. B* **79**, 035407 (2009).
- [74] J. Zhou, J. Dong, B. Wang, T. Koschny, M. Kafesaki, and C. M. Soukoulis, "Negative refractive index due to chirality," *Phys. Rev. B* **79**, 121104 (2009).
- [75] M. C. K. Wiltshire, J. B. Pendry, and J. V. Hajnal, "Chiral Swiss rolls show a negative refractive index," *J. Phys. Condens. Matter* **21**, 292201 (2009).
- [76] C. Wu, H. Li, Z. Wei, X. Yu, and C. T. Chan, "Theory and Experimental Realization of Negative Refraction in a Metallic Helix Array," *Phys. Rev. Lett.* **105**, 247401 (2010).
- [77] I. V. Lindell, A. H. Sihvola, and J. Kurkijärvi, "Karl F. Lindman: The Last Hertzian, and a Harbinger of Electromagnetic Chirality," *IEEE Antennas Propag. Mag.* **34**, 24 (1992).
- [78] J. D. Kraus, "Helical beam antenna," *Electronics* **20**, 109 (1947).
- [79] I. V. Semchenko, S. A. Khakhomov, and A. L. Samofalov, "Polarization Plane Rotation of Electromagnetic Waves by the Artificial Periodic Structure with One-Turn Helical Elements," *Electromagnetics* **26**, 219 (2006).
- [80] E. Saenz, I. Semchenko, S. Khakhomov, K. Guven, R. Gonzalo, E. Ozbay, and S. Tretyakov, "Modeling of Spirals with Equal Dielectric, Magnetic, and Chiral Susceptibilities," *Electromagnetics* **28**, 476 (2008).
- [81] I. V. Semchenko, S. A. Khakhomov, and S. A. Tretyakov, "Chiral metamaterial with unit negative refraction index," *Eur. Phys. J. Appl. Phys.* **46**, 32607 (2009).
- [82] J. D. Kraus and R. Marhefka, *Antennas: For All Applications* (McGraw-Hill, New York, 2003), 3rd ed.
- [83] J. K. Gansel, M. Wegener, S. Burger, and S. Linden, "Gold helix photonic metamaterials: A numerical parameter study," *Opt. Express* **18**, 1059 (2010).
- [84] A. V. Rogacheva, V. A. Fedotov, A. S. Schwanecke, and N. I. Zheludev, "Giant Gyrotropy due to Electromagnetic-Field Coupling in a Bilayered Chiral Structure," *Phys. Rev. Lett.* **97**, 177401 (2006).
- [85] E. Plum, V. A. Fedotov, and N. I. Zheludev, "Optical activity in extrinsically chiral metamaterial," *Appl. Phys. Lett.* **93**, 191911 (2008).
- [86] K. Robbie, M. J. Brett, and A. Lakhtakia, "Chiral sculptured thin films," *Nature* **384**, 616 (1996).
- [87] M. Thiel, M. Decker, M. Deubel, M. Wegener, S. Linden, and G. von Freymann, "Polarization Stop Bands in Chiral Polymeric Three-Dimensional Photonic Crystals," *Adv. Mater.* **19**, 207 (2007).

-
- [88] RÖMPP Online Chemie-Lexikon, <http://www.roempp.com/prod> (2012).
- [89] J. K. Gansel, M. Thiel, M. S. Rill, M. Decker, K. Bade, V. Saile, G. von Freymann, S. Linden, and M. Wegener, “Gold Helix Photonic Metamaterial as Broadband Circular Polarizer,” *Science* **325**, 1513 (2009).
- [90] B. Gallas, K. Robbie, R. Abdeddaïm, G. Guida, J. Yang, J. Rivory, and A. Priou, “Silver square nanospirals mimic optical properties of U-shaped metamaterials,” *Opt. Express* **18**, 16335 (2010).
- [91] A. Radke, T. Gissibl, T. Klotzbücher, P. V. Braun, and H. Giessen, “Three-Dimensional Bichiral Plasmonic Crystals Fabricated by Direct Laser Writing and Electroless Silver Plating,” *Adv. Mater.* **23**, 3018 (2011).
- [92] J. K. Gansel, M. Latzel, A. Frölich, J. Kaschke, M. Thiel, and M. Wegener, “Tapered gold-helix metamaterials as improved circular polarizers,” *Appl. Phys. Lett.* **100**, 101109 (2012).
- [93] H.-S. Kitzerow, and C. Bahr, eds., *Chirality in Liquid Crystals* (Springer, Heidelberg, 2001).
- [94] M. Thiel, G. von Freymann, and M. Wegener, “Layer-by-layer three-dimensional chiral photonic crystals,” *Opt. Lett.* **32**, 2547 (2007).
- [95] K. A. Bachman, J. J. Peltzer, P. D. Flammer, T. E. Furtak, R. T. Collins, and R. E. Hollingsworth, “Spiral plasmonic nanoantennas as circular polarization transmission filters,” *Opt. Express* **20**, 1308 (2012).
- [96] C. H. Hamann, A. Hamnett, and W. Vielstich, *Electrochemistry* (Wiley-VCH, 2007), 2nd ed.
- [97] M. Paunovic and M. Schlesinger, *Fundamentals of Electrochemical Deposition* (John Wiley & Sons, Inc., 1998).
- [98] D. Wahl, “Eine kleine Geschichte der Elektrochemie Teil 1,” *Galvanotechnik* **96**, 1600 (2005).
- [99] S. Arai, T. Saito, and M. Endo, “Metal-Fixed Multiwalled Carbon Nanotube Patterned Emitters Using Photolithography and Electrodeposition Technique,” *Electrochem. Solid-State Lett.* **11**, D72 (2008).
- [100] T. Watanabe, *Nano-Plating: Microstructure Formation Theory of Plated Films and a Database of Plated Films* (Elsevier, 2004).
- [101] E. W. Foster, G. J. Kearns, S. Goto, and J. E. Hutchison, “Patterned Gold-Nanoparticle Monolayers Assembled on the Oxide of Silicon,” *Adv. Mater.* **17**, 1542 (2005).
- [102] Z. Wu, H.-M. Li, X. Xiong, G.-B. Ma, M. Wang, R.-W. Peng, and N.-B. Ming, “Electrodeposition of single-crystalline silver pearl chains,” *Appl. Phys. Lett.* **94**, 041120 (2009).

- [103] R. Schuster, V. Kirchner, P. Allongue, and G. Ertl, "Electrochemical Micromachining," *Science* **289**, 98 (2000).
- [104] R. A. Farrer, C. N. LaFratta, L. Li, J. Praino, M. J. Naughton, B. E. A. Saleh, M. C. Teich, and J. T. Fourkas, "Selective Functionalization of 3-D Polymer Microstructures," *J. Am. Chem. Soc.* **128**, 1796 (2006).
- [105] W. Menz, J. Mohr, and O. Paul, *Microsystem Technology* (WILEY-VCH, 2001).
- [106] X. Yu, Y.-J. Lee, R. Furstenberg, J. O. White, and P. V. Braun, "Filling Fraction Dependent Properties of Inverse Opal Metallic Photonic Crystals," *Adv. Mater.* **19**, 1689 (2007).
- [107] S. V. Grigoriev, K. S. Napolskii, N. A. Grigoryeva, A. V. Vasilieva, A. A. Mistonov, D. Y. Chernyshov, A. V. Petukhov, D. V. Belov, A. A. Eliseev, A. V. Lukashin, Y. D. Tretyakov, A. S. Sinitskii, and H. Eckerlebe, "Structural and magnetic properties of inverse opal photonic crystals studied by x-ray diffraction, scanning electron microscopy, and small-angle neutron scattering," *Phys. Rev. B* **79**, 045123 (2009).
- [108] M. Datta and D. Landolt, "Fundamental aspects and applications of electrochemical microfabrication," *Electrochim. Acta* **45**, 2535 (2000).
- [109] J. Puipe and F. Leaman, *Theory and Practice of Pulse Plating* (American Electroplaters and Surface Finishers Society, 1986).
- [110] N. Kanani, *Galvanotechnik* (Carl Hanser Verlag, 2000).
- [111] D. Chanda, K. Shigeta, S. Gupta, T. Cain, A. Carlson, A. Mihi, A. J. Baca, G. R. Bogart, P. Braun, and J. A. Rogers, "Large-area flexible 3D optical negative index metamaterial formed by nanotransfer printing," *Nat. Nanotechnol.* **6**, 402 (2011).
- [112] A. Vlad, C. A. Dutu, P. Guillet, P. Jedrasik, C.-A. Fustin, U. Södervall, J.-F. Gohy, and S. Melinte, "Highly Ordered Conjugated Polymer Nanoarchitectures with Three-Dimensional Structural Control," *Nano Lett.* **9**, 2838 (2009).
- [113] S. Zhang, W. Fan, B. K. Minhas, A. Frauenglass, K. J. Malloy, and S. R. J. Brueck, "Fabrication of 1D and 2D vertical nanomagnetic resonators," *J. Vac. Sci. Technol., B* **22**, 3327 (2004).
- [114] K. Höflich, R. B. Yang, A. Berger, G. Leuchs, and S. Christiansen, "The Direct Writing of Plasmonic Gold Nanostructures by Electron-Beam-Induced Deposition," *Adv. Mater.* **23**, 2657 (2011).
- [115] D. B. Burckel, J. R. Wendt, G. A. Ten Eyck, J. C. Ginn, A. R. Ellis, I. Brener, and M. B. Sinclair, "Micrometer-Scale Cubic Unit Cell 3D Metamaterial Layers," *Adv. Mater.* **22**, 5053 (2010).
- [116] D. B. Burckel, J. R. Wendt, S. Samora, M. B. Sinclair, I. Brener, and J. C. Ginn, "Multilayer infrared metamaterial fabrication using membrane projection lithography," *J. Vac. Sci. Technol., B* **29**, 06FF04 (2011).

-
- [117] S. Kawata, H.-B. Sun, T. Tanaka, and K. Takada, "Finer features for functional microdevices," *Nature* **412**, 697 (2001).
- [118] M. Deubel, G. von Freymann, M. Wegener, S. Pereira, K. Busch, and C. M. Soukoulis, "Direct laser writing of three-dimensional photonic-crystal templates for telecommunications," *Nat. Mater.* **3**, 444 (2004).
- [119] A. Ishikawa, T. Tanaka, and S. Kawata, "Improvement in the reduction of silver ions in aqueous solution using two-photon sensitive dye," *Appl. Phys. Lett.* **89**, 113102 (2006).
- [120] T. Tanaka, "Plasmonic Metamaterials Produced by Two-photon-induced Photoreduction Technique," *J. Laser Micro/Nanoeng.* **3**, 152 (2008).
- [121] N. Vasilantonakis, K. Terzaki, I. Sakellari, V. Purlys, D. Gray, C. M. Soukoulis, M. Vamvakaki, M. Kafesaki, and M. Farsari, "Three-Dimensional Metallic Photonic Crystals with Optical Bandgaps," *Adv. Mater.* **24**, 1101 (2012).
- [122] J. Yao, Z. Liu, Y. Liu, Y. Wang, C. Sun, G. Bartal, A. M. Stacy, and X. Zhang, "Optical Negative Refraction in Bulk Metamaterials of Nanowires," *Science* **321**, 930 (2008).
- [123] B. Gallas, N. Guth, J. Rivory, H. Arwin, R. Magnusson, G. Guida, J. Yang, and K. Robbie, "Nanostructured chiral silver thin films: A route to metamaterials at optical frequencies," *Thin Solid Films* **519**, 2650 (2011).
- [124] R. R. Price, W. J. Dressick, and A. Singh, "Fabrication of Nanoscale Metallic Spirals Using Phospholipid Microtubule Organizational Templates," *J. Am. Chem. Soc.* **125**, 11259 (2003).
- [125] J.-H. Cho and D. H. Gracias, "Self-Assembly of Lithographically Patterned Nanoparticles," *Nano Lett.* **9**, 4049 (2009).
- [126] L. Liu, S.-H. Yoo, S. A. Lee, and S. Park, "Wet-Chemical Synthesis of Palladium Nanosprings," *Nano Lett.* **11**, 3979 (2011).
- [127] M. Yang and N. A. Kotov, "Nanoscale helices from inorganic materials," *J. Mater. Chem.* **21**, 6775 (2011).
- [128] C. Enkrich, "Magnetic Metamaterials for Photonics," Ph.D. thesis (2006).
- [129] H.-J. Krokoszinski and R. Oesterlein, "Post-Deposition Annealing Effects in Electron-Beam-Evaporated Indium Tin Oxide Thin Films," *Thin Solid Films* **187**, 179 (1990).
- [130] R. B. H. Tahar, T. Ban, Y. Ohya, and Y. Takahashi, "Tin doped indium oxide thin films: Electrical properties," *J. Appl. Phys.* **83**, 2631 (1998).
- [131] S. W. Hell and J. Wichmann, "Breaking the diffraction resolution limit by stimulated emission: stimulated-emission-depletion fluorescence microscopy," *Opt. Lett.* **19**, 780 (1994).

- [132] K. I. Willig, B. Harke, R. Medda, and S. W. Hell, "STED microscopy with continuous wave beams," *Nat. Methods* **4**, 915 (2007).
- [133] L. Li, R. R. Gattass, E. Gershgoren, H. Hwang, and J. T. Fourkas, "Achieving $\lambda/20$ resolution by one-color initiation and deactivation of polymerization," *Science* **324**, 910 (2009).
- [134] T. F. Scott, B. A. Kowalski, A. C. Sullivan, C. N. Bowman, and R. R. McLeod, "Two-Color Single-Photon Photoinitiation and Photoinhibition for Subdiffraction Photolithography," *Science* **324**, 913 (2009).
- [135] J. Fischer, G. von Freymann, and M. Wegener, "The Materials Challenge in Diffraction-Unlimited Direct-Laser-Writing Optical Lithography," *Adv. Mater.* **22**, 3578 (2010).
- [136] J. Fischer and M. Wegener, "Three-dimensional direct laser writing inspired by stimulated-emission-depletion microscopy," *Opt. Mater. Express* **1**, 614 (2011).
- [137] Nanoscribe GmbH, <http://www.nanoscribe.de> (2012).
- [138] MicroChemicals GmbH, <http://www.microchemicals.eu> (2012).
- [139] MicroChem Corp., <http://www.microchem.com> (2012).
- [140] M. Deubel, "Three-Dimensional Photonic Crystals via Direct Laser Writing: Fabrication and Characterization," Ph.D. thesis (2006).
- [141] J.-H. Lee, Y.-S. Kim, K. Constant, and K.-M. Ho, "Woodpile Metallic Photonic Crystals Fabricated by Using Soft Lithography for Tailored Thermal Emission," *Adv. Mater.* **19**, 791 (2007).
- [142] S. Maruo, T. Hasegawa, and N. Yoshimura, "Single-anchor support and supercritical CO₂ drying enable high-precision microfabrication of three-dimensional structures," *Opt. Express* **17**, 20945 (2009).
- [143] T. A. Green, M.-J. Liew, and S. Roy, "Electrodeposition of Gold from a Thiosulfate-Sulfite Bath for Microelectronic Applications," *J. Electrochem. Soc.* **150**, C104 (2003).
- [144] R. E. van Grieken and A. A. Markowicz, *Handbook of X-ray spectrometry*, Practical spectroscopy (Marcel Dekker, 1993).
- [145] E. Yablonovitch, "Inhibited Spontaneous Emission in Solid-State Physics and Electronics," *Phys. Rev. Lett.* **58**, 2059 (1987).
- [146] S. John, "Strong Localization of Photons in Certain Disordered Dielectric Superlattices," *Phys. Rev. Lett.* **58**, 2486 (1987).
- [147] K. M. Ho, C. T. Chan, C. M. Soukoulis, B. R., and S. M., "Photonic band gaps in three dimensions: new layer-by-layer periodic structures," *Solid State Commun.* **89**, 413 (1994).

-
- [148] C. M. McShane and K.-S. Choi, "Photocurrent Enhancement of n-Type Cu_2O Electrodes Achieved by Controlling Dendritic Branching Growth," *J. Am. Chem. Soc.* **131**, 2561 (2009).
- [149] T. D. Golden, M. G. Shumsky, Y. Zhou, R. A. VanderWerf, R. A. van Leeuwen, and J. A. Switzer, "Electrochemical Deposition of Copper(I) Oxide Films," *Chem. Mater.* **8**, 2499 (1996).
- [150] F. Hu, K. C. Chan, and T. M. Yue, "Morphology and growth of electrodeposited cuprous oxide under different values of direct current density," *Thin Solid Films* **518**, 120 (2009).
- [151] M. Miyake, Y.-C. Chen, P. V. Braun, and P. Wiltzius, "Fabrication of Three-Dimensional Photonic Crystals Using Multibeam Interference Lithography and Electrodeposition," *Adv. Mater.* **21**, 3012 (2009).
- [152] J. A. Switzer, C.-J. Hung, L.-Y. Huang, E. R. Switzer, D. R. Kammler, T. D. Golden, and E. W. Bohannan, "Electrochemical Self-Assembly of Copper/Cuprous Oxide Layered Nanostructures," *J. Am. Chem. Soc.* **120**, 3530 (1998).
- [153] Joint Committee on Powder Diffraction Standards, *Card Files no. 5-667 and no. 4-836*.
- [154] CST Microwave Studio, <http://www.cst.com/content/products/mws/overview.aspx> (2012).
- [155] Lumerical, <http://www.lumerical.com> (2012).
- [156] JCMSuite, <http://www.jcmwave.com> (2012).
- [157] E. Plum, X.-X. Liu, V. A. Fedotov, Y. Chen, D. P. Tsai, and N. I. Zheludev, "Metamaterials: Optical Activity without Chirality," *Phys. Rev. Lett.* **102**, 113902 (2009).
- [158] D.-H. Kwon, D. H. Werner, A. V. Kildishev, and V. M. Shalaev, "Material parameter retrieval procedure for general bi-isotropic metamaterials and its application to optical chiral negative-index metamaterial design," *Opt. Express* **16**, 11822 (2008).
- [159] M. Thiel, H. Fischer, G. von Freymann, and M. Wegener, "Three-dimensional chiral photonic superlattices," *Opt. Lett.* **35**, 166 (2010).
- [160] R. W. Wood, "On a Remarkable Case of Uneven Distribution of Light in a Diffraction Grating Spectrum," *Proc. Phys. Soc. London* **18**, 269 (1902).
- [161] A. Hessel and A. A. Oliner, "A New Theory of Wood's Anomalies on Optical Gratings," *Appl. Opt.* **4**, 1275 (1965).
- [162] M. Thiel, M. S. Rill, G. von Freymann, and M. Wegener, "Three-Dimensional Bi-chiral Photonic Crystals," *Adv. Mater.* **21**, 4680 (2009).
- [163] M. Thiel, "Design, fabrication, and characterization of three-dimensional chiral photonic crystals," Ph.D. thesis (2010).

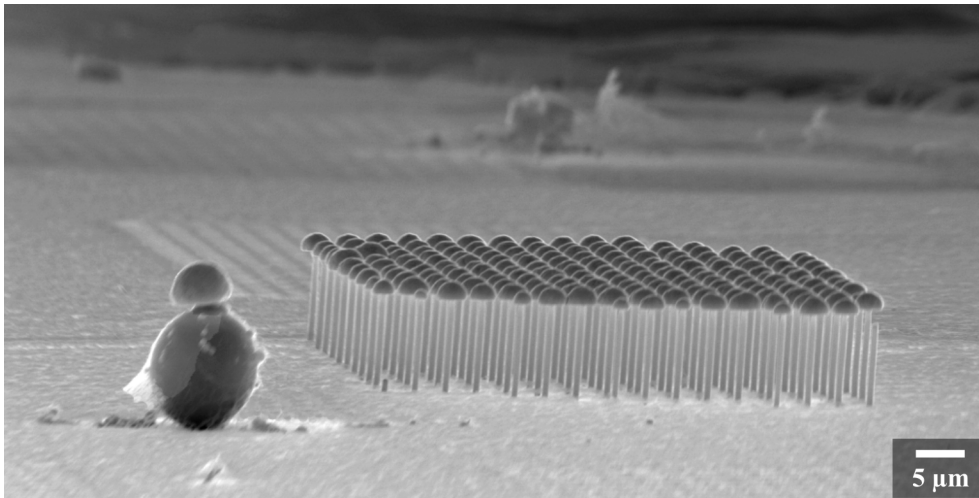
- [164] X. Xiong, X.-C. Chen, M. Wang, R.-W. Peng, D.-J. Shu, and C. Sun, “Optically nonactive assorted helix array with interchangeable magnetic/electric resonance,” *Appl. Phys. Lett.* **98**, 071901 (2011).
- [165] X. Xiong, X.-c. Chen, Z.-W. Wang, S.-C. Jiang, M. Wang, R.-W. Peng, X.-P. Hao, and C. Sun, “Construction of Chiral Metamaterial with a Helix Array,” arXiv:1107.4994v1 (2011).
- [166] M. Pourbaix, *Atlas d’équilibres Electrochimiques à 25°C* (Gautier-Villars & Cie, 1963).
- [167] M. Hermatschweiler, A. Ledermann, G. A. Ozin, M. Wegener, and G. von Freymann, “Fabrication of Silicon Inverse Woodpile Photonic Crystals,” *Adv. Funct. Mater.* **17**, 2273 (2007).
- [168] A. Frölich and M. Wegener, “Spectroscopic characterization of highly doped ZnO films grown by atomic-layer deposition for three-dimensional infrared metamaterials,” *Opt. Mater. Express* **1**, 883 (2011).
- [169] Z. Y. Yang, M. Zhao, P. X. Lu, and Y. F. Lu, “Ultrabroadband optical circular polarizers consisting of double-helical nanowire structures,” *Opt. Lett.* **35**, 2588 (2010).
- [170] Z. Yang, M. Zhao, and P. Lu, “How to improve the signal-to-noise ratio for circular polarizers consisting of helical metamaterials?” *Opt. Express* **19**, 4255–60 (2011).
- [171] C. J. Schuil, A. V. Amirkhizi, F. Bayatpur, and S. Nemat-Nasser, “Composites with mechanically tunable plasmon frequency,” *Smart Mater. Struct.* **20**, 115012 (2011).

Abbreviations

Names of repeatedly appearing variables and abbreviations used within this thesis are given here in alphabetical order (indices are not listed). The number of the page where an abbreviation or a variable name appears for the first time is shown.

2D	two-dimensional (p. 24)
3D	three-dimensional (p. 5)
a	lattice constant (p. 13); activity (p. 42)
AR	aspect ratio of the polarization ellipse (p. 21)
Au	gold (p. 11)
α	orientation of linear or elliptical polarization (p. 20)
\vec{B}	magnetic induction (p. 6)
c	phase velocity of light (p. 8)
C	circular basis (p. 22)
c_0	speed of light in vacuum (p. 8)
CO_2	carbon dioxide (p. 61)
Cu	copper (p. 12)
Cu_2O	copper(I) oxide (p. 53)
\vec{D}	electric displacement (p. 6)
DLW	direct laser writing (p. 54)
DNA	deoxyribonucleic acid (p. 1)
e	elementary charge (p. 10)
e	Euler's number (p. 12)
\vec{E}	electric field (p. 6)
$\vec{\mathcal{E}}$	real part of the electric field (p. 19)
ECD	electrochemical deposition (p. 39)
ε	electric permittivity (p. 7)
$\vec{\varepsilon}$	electric permittivity parameter tensor (p. 25)
ε_0	permittivity of the vacuum (p. 6)
f	frequency in THz (p. 8)
F	Faraday constant (p. 41)
FIB	focused ion beam (p. 54)
ϕ	phase of electromagnetic waves (p. 19)
φ	potential of an electrode or an electrolyte (p. 46)
$\Delta\varphi$	Galvani potential difference (p. 43)
\vec{H}	magnetic field (p. 6)
H_2O	water molecule (p. 40)
ITO	indium tin oxide (p. 56)

\vec{J}	current vector (p. 14); Jones vector (p. 21)
\vec{k}	wave vector (p. 8)
k_0	value of the wave vector in vacuum (p. 8)
κ	chirality parameter (p. 28)
$\vec{\kappa}$	chirality tensor (p. 26)
L	linear basis (p. 21)
LCP	left-circular polarization (p. 19)
LIGA	fabrication method involving lithography, electroplating, and molding (p. 50)
λ	wavelength (p. 8)
M	Jones matrix (p. 21)
\vec{M}	magnetization (p. 6)
me, me ^{z+}	metal atom and metal cation (p. 40)
μ	magnetic permeability (p. 7); chemical potential (p. 42)
$\vec{\mu}$	magnetic permeability parameter tensor (p. 25)
μ_0	permeability of the vacuum (p. 6)
n	refractive index (p. 8)
N	number of pitches of a helix (p. 35)
Ni	nickel (p. 12)
ν	overpotential (p. 47)
p	pitch height of a helix (p. 35)
\vec{p}	electric dipole moment (p. 15)
\vec{P}	polarization (p. 6)
θ	angle between wave vector and interface normal (p. 9)
r	reflection coefficient (p. 9); half of the helix wire thickness (p. 35)
\vec{r}	vector in 3D space (p. 6)
R	gas constant (p. 42)
R	helix radius (p. 35)
RCP	right-circular polarization (p. 19)
s	species (p. 41)
SEM	scanning electron microscope (p. 16)
t	time (p. 6); transmission coefficient (p. 9)
T	transmittance (p. 10); time period (p. 15); temperature (p. 42)
W	electrical energy (p. 42)
ω	frequency in rad (p. 7)
x, \hat{x}	distance and unit vector in x -direction (p. 10)
y, \hat{y}	distance and unit vector in y -direction (p. 19)
z, \hat{z}	distance and unit vector in z -direction (p. 19)
Z	impedance (p. 9)



Journey through the “fields of photonics”. (Thanks to S. Kühn for help with taking this SEM picture.)

Acknowledgements

Finally, I would like to thank all the people who accompanied and supported me on my journey through the “fields of photonics”.

Foremost, I thank my Ph.D. supervisor Prof. Dr. Martin Wegener for the opportunity of doing my thesis within his group. In this group, an excellent research environment with access to all necessary equipment is combined with work on fascinating topics. Thanks to numerous discussions, his profound knowledge in physics, and his general approach to work, I learned a lot in the past years.

I would also like to express my gratitude to Prof. Dr. Kurt Busch who had already been the co-referee during my diploma thesis and who has kindly agreed to also co-referee my Ph.D. thesis. His change to the Humboldt-Universität zu Berlin is a great loss as his and his group’s excellent theoretical background in photonics was an ideal match to our experimental group.

Many thanks also go to all the present and past group members who made this group a fruitful and enjoyable place to work. There was always someone at hand for discussions, a small chat, or simply a comrade during long days in the lab. In particular, I want to thank:

- Dr. Michael Thiel who contributed a lot to my work by doing the direct laser writing of some of the shown structures and by giving a lot of input, in particular with regard to new structure designs.
- Our former group members Prof. Dr. Stefan Linden and Prof. Dr. Georg von Freymann have always been a great help, thank you!
- Many thanks also go to Dr. Michael Rill, Andreas Frölich, and Martin Husnik for their input and helpful discussions.
- Also, I thank my former diploma student Michael Latzel who did very good work. He is now working on his own Ph.D. thesis, for which I wish him all the best.

This thesis also profited from the help of excellent cooperation partners. I thank Dr. Klaus Bade for his valuable help regarding the electrochemical deposition of gold. Also, I am grateful for the numerical calculations performed by Dr. Sven Burger and Dr. Mark Blome.

I thank the proofreaders of this thesis for their help in improving it and giving it its final touch: Prof. Dr. Stefan Linden, Martin Husnik, Jonathan Müller, Johannes Kaschke,

Acknowledgements

Andreas Frölich, Fabian Niesler, Florian Hübler, and Tiemo Bückmann. In particular, I thank Dr. Michael Thiel and Alexander Schick, who have read the entire work.

Moreover, I thank all the people who work at different facilities and keep our system running: Helmuth Lay, Werner Gilde, Heinz Hoffmann, and Michael Hippe, who never seem to grow tired of our messed up computers or broken electronics. Also, Renate Helfen, Claudia Alaya, and Monika Brenkmann have been an immense help. I thank our technician Johann Westhauser and our former technician Thorsten Kuhn for their help with various setups. Also, I am grateful to Denica Angelova, Katja Dopf, Dr. Nicolas Stenger, and Dr. Judith Elsner for the engagement and organization of all the interesting events within the Karlsruhe School of Optics and Photonics.

I thank my parents who gave me the ability to study physics and who have always supported me. I also thank my fiance Alexander Schick who did endure me in hard times, made joyful times even better, and who has supported me so much in these years.